

**PREPARATION OF MXene-DERIVED  
NiFe<sub>2</sub>O<sub>4</sub>/V<sub>2</sub>O<sub>5</sub> COMPOSITES FOR VISIBLE  
LIGHT PHOTODEGRADATION OF DYESTUFF  
AND ANTIMICROBIAL ACTIVITY**

**CHOONG MAN KIT**

**UNIVERSITI TUNKU ABDUL RAHMAN**

**PREPARATION OF MXene-DERIVED NiFe<sub>2</sub>O<sub>4</sub>/V<sub>2</sub>O<sub>5</sub> COMPOSITES FOR  
VISIBLE LIGHT PHOTODEGRADATION OF DYESTUFF AND  
ANTIMICROBIAL ACTIVITY**

**CHOONG MAN KIT**

**A project report submitted in partial fulfilment of the requirements for the  
award of Master of Environmental Technology**

**Faculty of Engineering and Green Technology  
Univeristi Tunku Abdul Rahman**

**December 2021**

## DECLARATION

I hereby declare that this project report is based on my original work except for citations and quotations which have been duly acknowledged. I also declare that it has not been previously and concurrently submitted for any other degree or award at UTAR or other institutions.

Signature

:



Name

: CHOONG MAN KIT

ID No.

: 20AGM00145

Date

: 10<sup>th</sup> Dec 2021

**APPROVAL FOR SUBMISSION**

I certify that this project entitled “**PREPARATION OF MXene-DERIVED NiFe<sub>2</sub>O<sub>4</sub>/V<sub>2</sub>O<sub>5</sub> COMPOSITES FOR VISIBLE LIGHT PHOTODEGRADATION OF DYESTUFF AND ANTIMICROBIAL ACTIVITY**” was prepared by **CHOONG MAN KIT** has met the required standard for submission in partial fulfilment of the requirements for the award of Master of Environmental Technology at Universiti Tunku Abdul Rahman.

Approved by,

Signature



Supervisor : ChM. Ts. Dr. Lam Sze Mun

Date : 13/12/21

The copyright of this report belongs to the author under the terms of the copyright Act 1987 as qualified by Intellectual Property Policy of Universiti Tunku Abdul Rahman. Due acknowledgement shall always be made of the use of any material contained in, or derived from, this report.

© 2021, Choong Man Kit. All right reserved.

Specially dedicated to  
my beloved mother and sisters.

## ACKNOWLEDGEMENTS

I would like to thank everyone who had contributed to the successful completion of this project. First and foremost, I would like to express my sincere gratitude to my research supervisor, ChM. Ts. Dr. Lam Sze Mun her invaluable advice, guidance, enormous patience and immense knowledge throughout the development for this research.

In addition, I would like to express my deepest gratitude towards Universiti Tunku Abdul Rahman (UTAR), Kampar, Faculty of Engineering and Green Technology for providing opportunity allowing me to conduct this project. I would like to express my appreciation to the lab officers from FEGT, Ms. Ng Suk Ting, Mr. Yong Tzzy Jeng and lab officers from FSc, Mr. Goh Wee Sheng, Mr. Leong Thung Lim and Mr. Seou Chi Kien for assisting me during the lab session.

Furthermore, I would like to show my great appreciation to senior, Yong Zi Jun who had helped and given me encouragement and advice during the hardship of the research project. Additionally, I would like to thank my friends, Branda, Rou Hui, Zhao Liang, Sin Ying, Tanveer, Junior and Hang who had always lending their helping hands during the research works.

Finally, I am grateful to my family members especially my mother for unceasing support and encouragement through the whole project.

**PREPARATION OF MXENE DERIVED NiFe<sub>2</sub>O<sub>4</sub>/V<sub>2</sub>O<sub>5</sub> COMPOSITES FOR  
VISIBLE LIGHT PHOTODEGRADATION OF DYESTUFF AND  
ANTIMICROBIAL ACTIVITY**

**ABSTRACT**

Industrial dyestuff wastewater contained various toxic organic and pathogenic microorganisms which can cause severe environmental pollution if the wastewater is directly discharged into natural water bodies. Heterogeneous semiconductor photocatalysis is a green and effective which can use sunlight energy to treat the numerous refractory substrates including the dyestuff wastewater and harmful microbes. In the present study, the delaminated-MXene/Nickel Ferrite/Vanadium Pentoxide (D-M/NFO/V) ternary composite was synthesized through a simple thermal decomposition method and employed in the photodegradation of Rhodamine B (RhB) under LED light irradiation. The as-synthesized photocatalysts were characterized through FESEM, EDX, XRD, UV-vis DRS and Potentiostat. Ternary D-M/NFO/V compound demonstrated reduction in band gap energy with effective charge carrier separation. Using RhB as a targeted pollutant, the ternary D-M/NFO/V composite exhibited the best photocatalytic performance (88.7%) than those of binary Nickel Ferrite/Vanadium Pentoxide (NFO/V) and unary photocatalysts over 4 h of irradiation. The enhanced photocatalytic performance was attributed to its unique morphology, smaller band gap and excellent photoelectrochemical properties. The effect of process parameters including the NFO loadings in binary NFO/V composite, D-M co-catalyst loadings in D-M/NFO/V ternary compound and solution pH were investigated. The results demonstrated that the optimized NFO loadings were 50 wt%, D-M loadings were 0.5 wt% and operated at pH 12. Besides, the antimicrobial activity of the as

synthesized photocatalysts was evaluated on the microbial inactivation towards *Staphylococcus aureus* (*S. aureus*) and *Bacillus cereus* (*B. cereus*). Among the photocatalysts, the ternary D-M/NFO/V composite showed the highest microbial inactivation performance over the period of 4 h. Moreover, the dominant species in treating dyestuff was determined through the radical scavenging experiment and both superoxide anions ( $\bullet\text{O}_2^-$ ) and hydroxyl ( $\bullet\text{OH}$ ) radicals were the major reactive oxygen species (ROS) which were responsible for the photocatalysis in this study. Furthermore, the D-M/NFO/V ternary compound also displayed outstanding recyclability which attained high removal efficiency of 84.2% after four successive runs. Lastly, the optimized ternary composite was successfully tested using real printed ink wastewater to reveal its potential application in the wastewater purification.

## TABLE OF CONTENT

<b>DECLARATION</b>	<b>ii</b>
<b>APPROVAAL FOR SUBMISSIONS</b>	<b>iii</b>
<b>ACKNOWLEDGEMENTS</b>	<b>vi</b>
<b>ABSTRACT</b>	<b>vii</b>
<b>TABLE OF CONTENTS</b>	<b>ix</b>
<b>LIST OF TABLES</b>	<b>xiii</b>
<b>LIST OF FIGURES</b>	<b>xiv</b>
<b>LIST OF SYMBOLS</b>	<b>xviii</b>
<b>LIST OF ABBREVIATIONS</b>	<b>xxi</b>

### CHAPTER

<b>1</b>	<b>INTRODUCTION</b>	
	1.1 Dyestuff Treatment using Advanced Oxidation Process (AOP)	1
	1.2 Problem Statement	3
	1.3 Objectives	5
	1.4 Scope of Study	5
<b>2</b>	<b>LITERATURE REVIEW</b>	
	2.1 Dye-containing Industrial Wastewater	7
	2.2 Dyestuff Treatment Methods	8
	2.2.1 Biological Treatment	10
	2.2.2 Physical Treatment	11
	2.2.3 Chemical Treatment	12
	2.3 Advanced Oxidation Process (AOP)	12

2.3.1	Principle of Heterogeneous Photocatalysis	14
2.3.2	V <sub>2</sub> O <sub>5</sub> Single Photocatalyst	16
2.3.3	NiFe <sub>2</sub> O <sub>4</sub> /V <sub>2</sub> O <sub>5</sub> Binary Photocatalyst	17
2.3.4	MXene-based Catalyst	17
2.3.5	Ti <sub>3</sub> C <sub>2</sub> -NiFe <sub>2</sub> O <sub>4</sub> /V <sub>2</sub> O <sub>5</sub> Ternary Photocatalytic Mechanisms	21
2.4	Process Parameter Studies	21
2.4.1	Co-catalyst Loading	22
2.4.2	Catalyst Loading	23
2.4.3	Solution pH	25
2.5	Photocatalytic Antimicrobial Studies	26
2.6	Summary	28

### 3 RESEARCH METHODOLOGY

3.1	Chemicals and Materials	29
3.2	Apparatus and Equipment	32
3.2.1	Photocatalysis Experimental Apparatus	32
3.2.2	UV-Vis Spectrophotometer	32
3.3	Analytical Procedures	33
3.3.1	Chemical Oxygen Demand (COD) Analysis	33
3.3.2	Biological Oxygen Demand (BOD) Analysis	34
3.3.3	Turbidity Analysis	34
3.3.4	pH Analysis	35
3.3.5	Colour Analysis	35
3.4	Preparation of Photocatalyst	36
3.4.1	Synthesis of V <sub>2</sub> O <sub>5</sub> Photocatalyst	36
3.4.2	Preparation of NiFe <sub>2</sub> O <sub>4</sub> /V <sub>2</sub> O <sub>5</sub> Binary Composite	36

3.4.3	Synthesis of Delaminated $Ti_3C_2$ MXene Co-catalyst	37
3.4.4	Preparation of D- $Ti_3C_2/NiFe_2O_4/V_2O_5$ Composite	38
3.5	Characterization of D- $Ti_3C_2/NiFe_2O_4/V_2O_5$ Composite	39
3.5.1	Morphology and Composition Analysis	39
3.5.2	Crystallization Analysis	40
3.5.3	UV-Vis Diffuse Reflectance Spectroscopy	40
3.5.4	Photoelectrochemical Analysis	40
3.6	Photocatalytic Degradation of Dyestuff	41
3.7	Mineralization Study	41
3.8	Parameter Studies	41
3.8.1	Co-catalyst Loading	41
3.8.2	Catalyst Loading	42
3.8.3	Solution pH	42
3.9	Antimicrobial Activity	42
3.10	The Role of Reactive Oxygen Species (ROS) for Degradation of Dyestuff	43
3.11	The Hydroxyl ( $\bullet OH$ ) Radicals Analysis	44
3.12	Recycling Test	44
3.13	Real Printed Ink Wastewater Effluent Study	44

## 4

### RESULTS AND DISCUSSION

4.1	Characterization of the Synthesized Photocatalysts	45
4.1.1	Morphological Analysis	46
4.1.2	Elemental Composition Analysis	48
4.1.3	Crystallization Phase Analysis	50
4.1.4	Band Gap Energy Analysis	53
4.1.5	Photoelectrochemical Test	55

4.2	Preliminary Study of Photocatalytic Degradation of RhB Dye	58
4.3	Effect of Process Parameter Studies on Photocatalytic Degradation of Dyestuff	62
4.3.1	Effect of NFO Catalyst Loading in NFO/V Binary Composite	61
4.3.2	Effect of D-M Co-catalyst Loading in D-M/NFO/V Ternary Composite	63
4.3.3	Effect of Solution pH	65
4.4	Antimicrobial Activities	67
4.5	Reactive Oxygen Species Responsible for RhB Removal	71
4.6	Reusability Study	74
4.7	Real Printed Ink Wastewater Study	76
<b>5</b>	<b>CONCLUSION AND RECOMMENDATIONS</b>	
5.1	Conclusion	77
5.2	Recommendations	79
	<b>REFERENCES</b>	80
	<b>APPENDICES</b>	
	<b>BOOK CHAPTER</b>	100
	<b>AWARDS</b>	101

**LIST OF TABLES**

<b>TABLE</b>	<b>TITLE</b>	<b>PAGE</b>
Table 2.1	Typical Dyestuff Wastewater Parameter with Standard Discharge Condition under Standard A and B (Department of Environment, 2010; Kishor, et al 2021).	8
Table 2.2	The Synthesis of Various MXene-based Catalyst with Respective Degradation Efficiency.	20
Table 3.1	List of Materials and Chemicals Used.	28
Table 4.1	The Potential Band of the Synthesized Photocatalysts.	44
Table 4.2	Parameters of the RhB dye before and after Photocatalytic Degradation using D-M/NFO/V Ternary Composite.	44
Table 4.3	Parameters of the Real Printed Ink Wastewater before and after Photocatalytic Degradation using D-M/NFO/V Ternary Composite under LED light irradiation for 4 h.	

**LIST OF FIGURES**

<b>FIGURE</b>	<b>TITLE</b>	<b>PAGE</b>
Figure 2.1	Classification of Dyes (Samsami, et al., 2020).	15
Figure 2.2	Basic Mechanism of Photocatalyst Excitation under light irradiation (Jayaraj and Paramasivam, 2018).	17
Figure 2.3	SEM imaged of (a) $Ti_3AlC_2$ MAX and (b) $Ti_3C_2$ MXene (Ihsanullah, 2020).	21
Figure 2.4	The Photocatalytic Mechanism of Ternary $Ti_3C_2$ - $NiFe_2O_4/V_2O_5$ Composites.	27
Figure 2.5	Inactivation of <i>S. aureus</i> Bacteria in (a) Control, (b) Pristine MXene, (c) Bare $Cu_2O$ , and (d) $Cu_2O$ /MXene composites (Wang, et al., 2020).	29
Figure 3.1	Flowchart of Experimental Work Involved in This Study.	30
Figure 3.2	Schematic Diagram of Photocatalytic Degradation System.	34
Figure 3.3	Flowchart of Thermal Decomposition of $NH_4VO_3$ to Yield $V_2O_5$ .	40

Figure 3.4	Flowchart of the Preparation of NiFe <sub>2</sub> O <sub>4</sub> Nanoparticles.	41
Figure 3.5	Flowchart of Synthesis 2D Ti <sub>3</sub> C <sub>2</sub> MXene.	42
Figure 3.6	Flowchart of D-Ti <sub>3</sub> C <sub>2</sub> /NiFe <sub>2</sub> O <sub>4</sub> /V <sub>2</sub> O <sub>5</sub> Composite Fabrication.	43
Figure 4.1	FESEM Images of (a) V, (b) NFO, (c) M, (d) D-M, (e) NFO/V and (f) D-M/NFO/V.	46
Figure 4.2	EDX Spectra of (a) V, (b) NFO, (c) M, (d) D-M, (e) NFO/V and (f) D-M/NFO/V.	47
Figure 4.3	EDX Mapping of D-M/NFO/V Ternary Composite.	49
Figure 4.4	XRD patterns of the Synthesized Photocatalysts.	50
Figure 4.5	XRD patterns of MAX, MXene and D-M.	52
Figure 4.6	Magnified image indicating the presence of D-M in ternary composite.	54
Figure 4.7	UV-vis DRS Spectra of the Synthesized Photocatalysts.	55
Figure 4.8	Kubelka-Munk Function Plot of $(F(R)hv)^2$ versus $hv$ of V, NFO, NFO/V and D-M/NFO/V photocatalysts.	57
Figure 4.9	(a) TPR and (b) EIS Nyquist Plot of the Synthesized Photocatalyst.	59
Figure 4.10	Mott-Schottky Plot for (a) Pure V and (b) Pure NFO.	60

- Figure 4.11 RhB Dye Removal Efficiency under Photolysis and Photocatalysis ([RhB Dye] = 5 mg/L; [Catalyst] = 0.5 g/L; Solution pH = 12.0).
- Figure 4.12 UV-vis Absorption Spectrum of RhB at  $\lambda = 553$  nm Against Time.
- Figure 4.13 Photocatalytic Activity of Pure V, Pure NFO and NFO/V with various NFO loadings toward the Degradation of RhB Dye ([RhB] = 5 mg/L; [Catalyst] = 0.5 g/L; Solution pH = 12).
- Figure 4.14 Photocatalytic Activity D-M/NFO/V Ternary Compound at Different D-M loadings toward Degradation of RhB Dye ([RhB] = 5 mg/L; [Catalyst] = 0.5 g/L; Solution pH = 12).
- Figure 4.15 Photocatalytic Activity of D-M/NFO/V ternary composite at different solution pH toward Degradation of RhB ([RhB] = 5 mg/L; [Catalyst] = 0.5 g/L).
- Figure 4.16 The Photocatalytic Antibacterial Activities toward *S. aureus* under as-prepared Photocatalysts.
- Figure 4.17 The Photocatalytic Antibacterial Activities toward *B. cereus* under as-prepared Photocatalysts.
- Figure 4.18 Effects of Various Scavengers on LED light Photocatalytic Degradation of RhB over D-M/NFO/V Ternary Composite ([RhB] = 5 mg/L; [Catalyst] = 0.5 g/L; Solution pH = 12).

- Figure 4.19 Schematic diagram for Mechanism of Photodegradation over D-M/NFO/V Ternary Composite.
- Figure 4.20 The Recycling Experiment for the Photocatalytic Degradation of RhB over D-M/NFO/V ([RhB] = 5 mg/L; [Catalyst] = 0.5 g/L; Solution pH = 12).
- Figure 4.21 D-M/NFO/V Ternary Composite (a) Suspended in aqueous and (b) Separated by External Magnetic Force.

## LIST OF SYMBOLS

$2\theta$	Two Theta
$A$	Absorbance at specific $\lambda$
$\text{\AA}$	Ångström
$c$	Concentration, mg/L
$^{\circ}\text{C}$	Degree Celsius
$g$	Gram
$h$	hour
$l$	Length of Light Transport Path, cm
$M$	Molarity
$mm$	Millimeter
$nm$	Nanometer
$t$	Time
$W$	Watt
$\epsilon$	Coefficient of Molar Absorption, L/mol/cm
$\lambda$	Wavelength, $\text{cm}^{-1}$
$\mu\text{m}$	Micrometer
$\bullet\text{O}_2^-$	Superoxide Anion Radical
$\bullet\text{OH}$	Hydroxyl Radical
$\text{Ag}$	Silver
$\text{Ag}_2\text{O}$	Silver Oxide
$\text{Ag}_2\text{WO}_4$	Silver Tungstate
$\text{Ag}_3\text{PO}_4$	Silver Phosphate
$\text{AgCl}$	Silver Chloride
$\text{Al}$	Aluminium
$\text{As}$	Arsenic
$\text{Au}$	Gold

$\text{Bi}_2\text{MoO}_6$	Bismuth Molybdate
$\text{Bi}_2\text{WO}_6$	Bismuth Tungstate
$\text{BiFeO}_3$	Bismuth Ferrite
$\text{BiOClBr}$	Bismuth Oxyhalides
$\text{BiVO}_4$	Bismuth Vanadate
BQ	Benzoquinone
C	Carbon
$\text{C}_2\text{H}_5\text{OH}$	Ethanol
$\text{CeO}_2$	Cerium Oxide
CNT	Carbon Nanotube
$\text{CO}_2$	Carbon Dioxide
$\text{Cu}^+$	Copper (I) Ion
$\text{Cu}^{2+}$	Copper (II) Ion
$\text{Cu}_2\text{O}$	Cuprous Oxide
F	Fluorine
Fe	Iron
$\text{Fe}(\text{NO}_3)_3 \cdot 9\text{H}_2\text{O}$	Iron (III) Nitrate Nonahydrate
$\text{Fe}_2\text{O}_3$	Iron (III) Oxide
g- $\text{C}_3\text{N}_4$	Graphitic Carbon Nitride
$\text{H}^+$	Hydrogen Ion
$\text{H}_2$	Hydrogen
$\text{H}_2\text{O}$	Water
$\text{H}_2\text{O}_2$	Hydrogen Peroxide
$\text{H}_2\text{SO}_4$	Sulphuric Acid
HCl	Hydrochloric Acid
$\text{HNO}_3$	Nitric Acid
$\text{HO}_2^-$	Hydroperoxyl Ion
$\text{HO}_2^\bullet$	Hydroperoxyl Radical
KBr	Potassium Bromide
KI	Potassium Iodide
$\text{MgSO}_4$	Magnesium Sulphate
$\text{MnO}_2$	Manganese Oxide
N	Nitrogen
$\text{Na}_2\text{SO}_4$	Sodium Sulphate

NaCl	Sodium Chloride
NaOH	Sodium Hydroxide
Nb <sub>2</sub> CT <sub>x</sub>	Niobium Carbide
NH <sub>4</sub> VO <sub>3</sub>	Ammonium Metavanadate
Ni(NO <sub>3</sub> ) <sub>2</sub> •6H <sub>2</sub> O	Nickel Nitrate Hexahydrate
Ni	Nickel
Ni <sup>2+</sup>	Nickel (II) Ion
NiFe <sub>2</sub> O <sub>4</sub>	Nickel Ferrite
O <sub>2</sub>	Oxygen
O <sub>2</sub> <sup>-•</sup>	Superoxide Anion Radical
O <sub>3</sub>	Ozone
O <sub>3</sub> /H <sub>2</sub> O <sub>2</sub>	Peroxone-process
OH <sup>-</sup>	Hydroxide Ion
Pb	Lead
PCN	Porous g-C <sub>3</sub> N <sub>4</sub>
Pt	Platinum
SnO <sub>2</sub>	Tin Dioxide
SO <sub>4</sub> <sup>•-</sup>	Sulphate Radical
Ti	Titanium
Ti <sub>3</sub> AlC <sub>2</sub>	Titanium Aluminium Carbide
Ti <sub>3</sub> C <sub>2</sub>	Titanium Carbide
TiO <sub>2</sub>	Titanium Dioxide
TMAOH	Tetramethylammonium Hydroxide
V	Vanadium
V <sub>2</sub> O <sub>5</sub>	Vanadium Pentoxide
WO <sub>3</sub>	Tungsten Trioxide
ZnO	Zinc Oxide

## LIST OF ABBREVIATIONS

2-D	Two Dimensional
<i>A. Niger</i>	<i>Aspergillus Niger</i>
AC	Activated Carbon
AMDI	American Dye Manufactures Institute
AOP	Advanced Oxidation Process
BOD	Biological Oxygen Demand
BQ	Benzoquinone
CB	Conductive Band
CC	Chemical Coagulation
CNT	Carbon Nanotube
COD	Chemical Oxygen Demand
$COD_0$	Initial COD Value
$COD_f$	Final COD Value
Co-floc	Coagulation-flocculation
CV	Crystal Violet
DI	Deionized Water
D-M	Delaminated $Ti_3C_2$ MXene
DO	Dissolve Oxygen
$DO_0$	Initial Value of DO
$DO_5$	DO Value after Incubation of 5 Days
DOE	Department of Environment
<i>E. coli</i>	<i>Escherichia coli</i>
EC	Electrocoagulation
EC	Electrocoagulation
$e_{cb}^- - h_{vb}^+$	Electron-Hole Pair
$e_{cb}^-$	Electron
EDX	Energy Disperse X-Ray

EIS	Electrochemical Impedance
EO	Electrooxidation
Eq.	Equation
eV	Electron Volt
FEGT	Faculty of Engineering and Green Technology
FESEM	Field Emission Scanning Electron Microscopy
FESEM	Field-Emission Scanning Electron Microscopy
FTO	Fluorine doped Tin Oxide
$h_{vb}^+$	Hole
HF	Hydrofluoric Acid
HR	High Range
HTA	Hydroxyl Terephthalic Acid
IPA	Isopropanol
<i>K. pneumoniae</i>	<i>Klebsiella pneumoniae</i>
LED	Light Emission Diode
LR	Low Range
LSV	Linear Sweep Voltammetry
MB	Methylene Blue
MBR	Membrane Bioreactor
MFC	Microbial Fuel Cell
MG	Malachite Green
MO	Methyl Orange
MS	Mott Schottky
NP	Nanoparticle
NTU	Nephelometric Turbidity Units
OFL	Ofloxacin
<i>P. aeruginosa</i>	<i>Pseudomonas aeruginosa</i>
<i>P. Vulgaris</i>	<i>Proteus Vulgaris</i>
PL	Photoluminescence
POME	Palm Oil Mill Effluent
POP	Persistent Organic Pollutants
RhB	Rhodamine B
RO	Reverse Osmosis
ROS	Reactive Oxygen Species

<i>S. aureus</i>	<i>Staphylococcus aureus</i>
SFE	Sulfadimidine
SRT	Sludge Retention Time
SS	Suspended Solids
TC	Tetracycline
TOC	Total Organic Carbon
TPR	Transient Photocurrent Response
UTAR	Universiti Tunku Abdul Rahman
UV	Ultraviolet
UV-vis DRS	UV-visible Diffuse Reflectance Spectroscopy
UV-Vis	Ultraviolet-Visible
VB	Valence Band
VOC	Volatile Organic Compound
wt%	Weight Percentage
Xe	Xenon
XRD	X-Ray Diffraction
ZOI	Zone of Inhibition

## CHAPTER 1

### INTRPDUCTION

#### 1.1 Dyestuff Treatment using Advanced Oxidation Process (AOP)

In this urbanization era, the rapid development in Malaysia leading to the increase in the use of natural resources. At the end, the waste generated was returned to the natural environment which causes severe environmental pollution especially water pollution. The water pollution mainly contributed by the industries including the pharmaceutical, paper and pulp, agricultural, printing ink, textile, food processing, and etcetera (Anantha, et al., 2021). Generally, the industrial dyestuff wastewater contained various inorganic and organic pollutants such as dye molecules, synthetic organic compound, and microorganism (Hiremath, et al., 2020). Among these pollutants, the dyestuff has more complicated structure that is highly toxicity and weak biodegradability (Chen, et al., 2017). Due to the stability of dye molecules against photolytic process, a more promising treatment process is needed to degrade these recalcitrant.

The dyestuff wastewater is generated from various type of industries. It contained components that are non-biodegradable, numerous kinds of pigment and trace amount of metal ions (Papadopoulos, et al., 2019). Typical physiochemical characteristics of dyestuff wastewater, including high colour intensity, biochemical oxygen demand (BOD), suspended solids (SS), and high chemical oxygen demand (COD) values (Ma, et al., 2021a). The presence of high COD, BOD and SS in the effluent cause the deterioration of dissolved oxygen (DO), which subsequently affect the aquatic ecosystem. The depletion of DO may reduce the survival rate of aquatic creatures and destroy the balance of ecosystem. Besides, the highly intense dye components diminished the penetration of sunlight that inhibited the photosynthesis of

aquatic plants (Anantha, et al., 2021). Therefore, the dyestuff wastewater must be treated appropriately prior to be discharged to the natural environment to prevent deterioration of water quality.

Conventional physical and chemical treatment techniques for dye-containing wastewater such as membrane filtration, reverse osmosis, adsorption by activated carbon, biosorption, coagulation-flocculation, electrocoagulation, and chemical precipitation (Prasad, et al., 2018; Atacan, Güy and Özacar, 2021). Among these processes, the coagulation-flocculation and adsorption are the most applicable techniques used to remove dye pollutants. Both processes involved the transfer of dye molecules from liquid phase transfer into solid phase or immobilized the contaminants. The adsorbent and coagulant used for the treatment of dyestuff wastewater are selectively remove certain pollutants as they are highly dependent to their nature surfaces. However, these treatment technologies have limitations and drawbacks which including long reaction time, high operating cost, ineffective due to the complexity of dye molecules, generation of secondary pollutants, and extra cost needed for the disposal and treatment of sludge (Alakhras, et al., 2020; Feizpoor, et al., 2021). Therefore, a green technology is required to develop non-toxic, effective, affordable, and easy operation system for treating and degrading dye wastewater.

In recent year, the advanced oxidation processes (AOPs) had become the research focus in the water and wastewater treatment especially dye-containing wastewater due to its advantages over the conventional treatment process, such as shorter treatment time, higher degradation efficacy, and less sludge production (Mishra, et al., 2020; Rafique, et al., 2020)). The AOPs including Electron-Fenton and Fenton process, Photo-Fenton process, ozone oxidation, photocatalytic oxidation reaction and UV-based process (Corona-Bautista, et al., 2021). Among the AOPs, the photocatalytic oxidation using nano-photocatalyst is a promising green technology being employed in treating persistent organic and inorganic pollutants non-selectively with synchronized antimicrobial activity.

## 1.2 Problem Statement

Dye-containing wastewater is one of the major contributors to the water pollution in Malaysia as numerous industries involved in the use of colouring agent, including textile industries, paper and pulp factory, food processing plant, plastic and polymer manufacturing industries, paint, and pigment factory. These wastewaters contained various pollutants such as persistent organic dye molecules, surfactants, acids, alkalis, dispersing agents, and may also contained pathogenic microorganisms. Wools and cottons as the raw materials in textile industries may leads to microbial growth. In typical textile processing, antimicrobial agents will be added to inhibit the microbial growth to prevent infectious pathogenic disease (Younis, Serp and Nassar, 2021). Rhodamine B (RhB) dye is a basic red dye which is well-known used in plastic, printing, food colouring and textile industry for dyeing wool, cotton, leather and silk (Rani S, et al., 2020). Experimental proven that RhB may pose to teratogenic and carcinogenic effect on humans and animals health (Rajalakshmi et al., 2017; Prasad et al., 2018; Govindaraj et al., 2021).

The advanced oxidation processes (AOPs) have shown high efficiency to eliminate the wastewater pollutants due to the generation of highly reactive radical primarily the hydroxyl radicals ( $\bullet\text{OH}$ ) (Corona-Bautista, et al., 2021). Among the AOPs, heterogeneous photocatalytic technology under the UV radiation had become more prominent due to its ability to completely mineralize persistent pollutants into carbon dioxide ( $\text{CO}_2$ ) and water ( $\text{H}_2\text{O}$ ) (Ariyanti, Maillot and Gao, 2018; Ma, et al., 2021a). The photocatalysis utilizing nano size photo-activated semiconductors, particularly metal oxide for generating  $e_{cb}^- - h_{vb}^+$  pairs to achieve mineralization of contaminants. ZnO (band gap  $\approx 3.2$  eV) and  $\text{TiO}_2$  (band gap = 3.0 – 3.2 eV) have been widely applied in photocatalytic wastewater treatment, water splitting, carbon dioxide ( $\text{CO}_2$ ) reduction and many other applications. However, both photocatalysts are active under the ultraviolet light (UV) region, which accounted less than 4% of the sunlight due to its large band gap energy. Therefore, the visible light driven photocatalyst had becoming researchers' focus for photocatalytic applications.

Narrow band gap photocatalyst, such as  $\text{V}_2\text{O}_5$  has the advantages as a n-type semiconductor with low band gap ranging from 2.4 to 2.8 eV, good photo and chemical

stability, non-toxic, large surface area, easily synthesized, and high visible light absorption (Jayaraj et al., 2018; Jayaraj and Paramasivam, 2019). However, the single visible-light driven photocatalyst has its drawback as narrow band gap promoting fast recombination rate of the photogenerated  $e_{cb}^- - h_{vb}^+$  pairs and produce heat in the reaction (Dadigala et al., 2019). To overcome the abovementioned issue, the single  $V_2O_5$  can be coupled via metal deposition, elemental doping, fabrication of heterostructure composite with metal oxide or multi-layered 2-Dimensional (2-D) nanomaterial. These methods can transfer the photogenerated  $e^-$  to the composite material and prolong the recombination rate of  $e_{cb}^- - h_{vb}^+$  pairs.

Moreover, the use of semiconductor catalyst in wastewater treatment is difficult to be separated and recycled which may induce the secondary pollution. As the consequence, it is not practically being adopted in real industrial wastewater treatment process. To overcome this limitation, the introduction of magnetic materials to be coupled with the pristine semiconductor photocatalyst. Nickel ferrite ( $NiFe_2O_4$ ) nanoparticles had gained attraction as a promising material in photocatalysis due to its magnetic properties, great photo-corrosion resistance, low toxicity, and extensive light absorption as it has narrow bandgap energy (1.56 – 2.19 eV). Apart from the enhancement of the separation of the photogenerated  $e_{cb}^- - h_{vb}^+$  pairs, the coupling of  $NiFe_2O_4$  to  $V_2O_5$  as a composite material can be easily recovered through external magnetic force, which greatly improve the reusability of semiconductor photocatalyst. To further improve the photocatalytic performance of  $NiFe_2O_4/V_2O_5$  composite, the 2-D nanosheet MXene as new considerable attention from researchers after 2-D graphene due to their enormous properties. The MXene has tremendous properties including good electronic and conductive properties, existence of active sites, and large surface area (Sun, et al., 2019; Ihsanullah, 2020).

Apart from the photocatalytic degradation of organic pollutants, the generation of reactive oxygen species (ROS) was found effective in antimicrobial activities. *E. coli*, a gram-negative microorganism that commonly found in water bodies such as pond, lake, river and stream. This bacterium may cause water-borne disease such as cholera, urinary tract infection and diarrhoea. The highly reactive ROSs could destruct the bacterial cell membrane, damage proteins, DNA, and lipids through oxidation (Jaffari, et al., 2019b; Mukhtar, et al., 2021).

To the best of own knowledge, there is no literature study adopting the  $\text{Ti}_3\text{C}_2\text{-NiFe}_2\text{O}_4/\text{V}_2\text{O}_5$  ternary composite material in treating real dyestuff wastewater and antimicrobial activities. The newly emerging of the 2D  $\text{Ti}_3\text{C}_2$  MXene as co-catalyst in photocatalytic wastewater treatment is an advanced material due to the abovementioned properties. The  $\text{NiFe}_2\text{O}_4/\text{V}_2\text{O}_5$  binary composite has narrow bandgap energy, which absorbed broad range of light could be initiated under visible light irradiation. In this study, the performance of  $\text{Ti}_3\text{C}_2\text{-NiFe}_2\text{O}_4/\text{V}_2\text{O}_5$  ternary nanocomposite in degrading dyestuff wastewater and antimicrobial activities will be evaluated.

### 1.3 Objectives

The objectives in current study are:

1. To synthesis a MXene- $\text{NiFe}_2\text{O}_4/\text{V}_2\text{O}_5$  composite through a simple thermal decomposition method.
2. To characterize the physiochemical, optical, and electronic properties of the synthesized  $\text{Ti}_3\text{C}_2\text{-NiFe}_2\text{O}_4/\text{V}_2\text{O}_5$  composite using various characterization methods.
3. To investigate the photocatalytic performance of  $\text{Ti}_3\text{C}_2\text{-NiFe}_2\text{O}_4/\text{V}_2\text{O}_5$  composite towards the degradation of RhB dye and antimicrobial activity under visible light.
4. To study the photocatalytic mechanism of the synthesized  $\text{Ti}_3\text{C}_2\text{-NiFe}_2\text{O}_4/\text{V}_2\text{O}_5$  composite via a radical scavenger and TAPL tests.

### 1.4 Scope of Study

In this study, the photocatalytic degradation of RhB dye and antimicrobial activity utilizing 2D  $\text{Ti}_3\text{C}_2$  MXene- $\text{NiFe}_2\text{O}_4/\text{V}_2\text{O}_5$  composite will be conducted. Besides, the as-synthesized  $\text{Ti}_3\text{C}_2\text{-NiFe}_2\text{O}_4/\text{V}_2\text{O}_5$  composite will be characterized using FESEM-EDX, XRD, UV-Vis DRS, PL, and Photoelectrochemical technique. The water quality parameters such as chemical oxygen demand (COD), biochemical oxygen demand

(BOD), turbidity, and colour will be analyzed. Furthermore, the effect of process parameters including the MXene  $\text{Ti}_3\text{C}_2$  co-catalyst loading, composite loading, and pH of wastewater on the photocatalytic degradation and antimicrobial activity will be investigated. The photocatalytic mechanism of the synthesized  $\text{Ti}_3\text{C}_2\text{-NiFe}_2\text{O}_4/\text{V}_2\text{O}_5$  composite via radical scavenger test and TAPL test will be studied. Finally, the real industrial printing wastewater will be treated using the optimized composite materials under visible light irradiation.

## CHAPTER 2

### LITERATURE REVIEW

#### 2.1 Dye-containing Industrial Wastewater

Industrialization in the development of a country leading to the inclining generation of wastewater. Major dye-containing industrial wastewater in worldwide, including textile wastewater, tannery, paper and pulp factories, food processing industries, paint, and dye manufacturing plants (Samsami, et al., 2020). According to the statistical data, there are approximately 70 Mega Tons of dyestuffs is generated per year throughout the world (Kishor, et al., 2021). The generation of dyestuff wastewater particularly the printing ink wastewater had increased drastically due to the increase in the demand for paper printing, packaging, carton, and cardboard (Emamjomeh, et al., 2020). Generally, the wastewater contained multicomplexes and recalcitrant such as complicated dye compounds and pigments, surfactants, alkalis, acids, dispersing agents, solvents, resins, additives, binders, detergents, persistent organic pollutants (POP), volatile organic compounds (VOC), and heavy metals (Ramos, et al., 2019; Hiremath, et al., 2020; Kishor, et al., 2021). Besides, numerous microbial pathogens are also present due to the high organic contents in wastewater. These pathogenic microorganisms, including *S. aureus*, *E. coli*, *P. aeruginosa*, *K. pneumoniae*, and *P. Vulgaris* (Manikandan, et al., 2021; Mukhtar, et al., 2021; Uma, et al., 2021).

These contaminants posed of great impacts if being discharged without proper treatment. Some impacts to the environment including the deterioration of dissolved oxygen (DO) amount in water bodies leading to insufficient oxygen supplied for aquatic creatures as well as the scattering and reduction in light penetration in which the aquatic plants will be restricted from undergoing photosynthesis. Besides, other

harmful impacts such as the mutagenicity, genotoxicity, carcinogenicity, neurotoxicity, and disruption of endocrine system by the dyestuffs are threatening human life (Samsami, et al., 2020; Kishor, et al., 2021).

According to the literature study, it was estimated that more than one hundred thousand types of dyes were used for variety industries. These dyes can be classified based on its solubility in water and further divided into different groups based on their physical-chemical properties. Figure 2.1 illustrates the classification of dyestuffs. For example, a basic red dye of xanthan which is highly soluble in water, namely Rhodamine B (RhB) dye is a dyeing agent used in textile, paper printing, and food processing factory. It may cause irritation to human body parts such as eye, skin, and respiratory tract. Experimental proven that RhB may pose to teratogenic and carcinogenic effect on humans and animals health (Rajalakshimi, et al., 2017; Prasad, et al., 2018; Govindaraj, et al., 2021). The appropriate treatment technology is needed for this hazardous wastewater before being released to the natural water bodies. The typical physical-chemical characteristics of dyestuff wastewater together with their respective acceptable conditions for discharge in Standard A and B are tabulated in Table 2.1.

## **2.2 Dyestuff Treatment Methods**

The hazardous of dye-containing wastewater, such as high chemical oxygen demand (COD), biochemical oxygen demand (BOD), surfactants and various organic as well as inorganic compounds. As a consequence, more advanced wastewater treatment technologies are needed to be implemented. The conventional physical, biological, and chemical treatment techniques for dye-containing wastewater, such as membrane filtration, reverse osmosis, adsorption by activated carbon, biosorption, membrane bioreactor, anaerobic digestion, coagulation-flocculation, electrocoagulation and chemical precipitation (Prasad, et al., 2018; Atacan, Güy and Özacar, 2021).

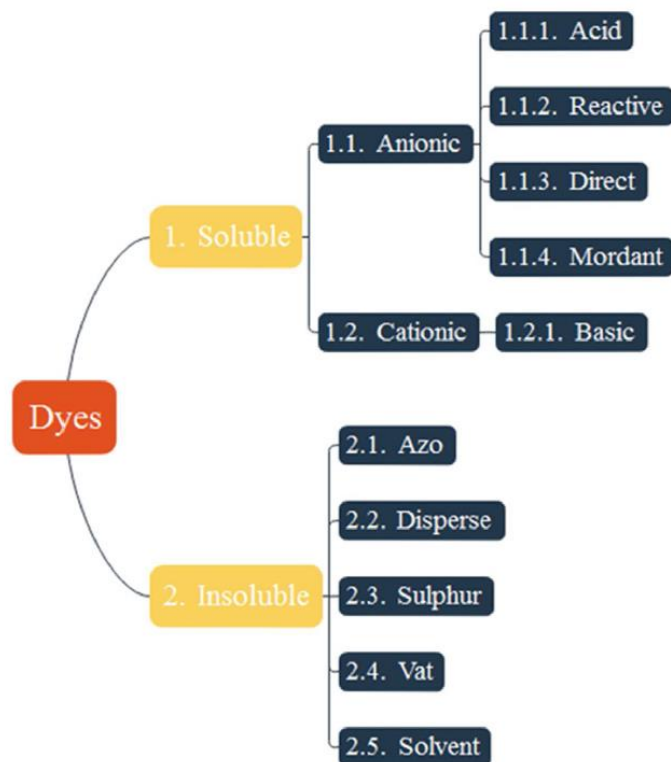


Figure 2.1: Classification of Dyes (Samsami, et al., 2020).

Table 2.1: Typical Dyestuff Wastewater Parameter with Standard Discharge Condition under Standard A and B (Department of Environment, 2010; Kishor, et al 2021)

Parameters	Unit	Typical Value	Standard	
			A	B
pH	-	8.8	6.0 – 9.0	5.5 – 9.0
COD	mg/L	1200	80	250
BOD	mg/L	230	20	40
SS	mg/L	250	50	100
Copper	mg/L	0.5	0.2	1.0
Zinc	mg/L	0.4	2.0	2.0
Cadmium	mg/L	0.6	0.01	0.02
Phenol	mg/L	0.5	0.001	1.0
Colour	AMDI*	-	100	200

\* AMDI- American Dye Manufactures Institute.

### 2.2.1 Biological Treatment

The biological treatment is the conventional wastewater treatment process for high organic strength pollutants. It is well-known as a green approach to degrade numerous kinds of wastewater. Basically, it utilized the microorganism's properties to degrade high COD and BOD contaminants through anaerobic, aerobic, and anoxic (or facultative) digestions (Holkar, et al., 2016; Samsami, et al., 2020). The anaerobic process for the degradation of pollutants is the most conventional treatment process for the high strength textile wastewater, followed by aerobic degradation to further polishing the wastewater to better effluent quality. There are various biological treatment technologies that can be implemented in the dyestuff wastewater, including constructed wetland, phytoremediation, anaerobic and aerobic membrane bioreactor (Emanjomeh, et al., 2020; Choerudin, et al., 2021; Mustafar and Hyder, 2021; Yurtsever, et al., 2021).

The membrane bioreactor (MBR) is an integral technology in wastewater treatment as it combined both membrane technology and biological process in a system. The typical MBR system is treating the high COD wastewater anaerobically followed by the filtration of micro pollutants that could not be degraded by microbes through the nanofiltration membrane. A study conducted by Erkan and co-workers (2020) applying the modified MBR system for synthetic textile wastewater treatment. They operated the bioreactor with a sludge retention time (SRT) of 30 days to stabilize the system. In their research, the high COD removal efficiency was obtained for conventional MBR and modified MBR at 93% and 98%, respectively. However, the major drawback of the MBR system is that the membrane fouling issue due to the formation of biofilm on the membrane leading to the deterioration of filtration capacity. Additionally, the fouling of membrane may also cause the reduction of permeate water flux which increase the trans-membrane pressure when it operated for longer treatment time (Jegatheesan, et al., 2016). Consequently, the clogging of membrane leading to high operating costs for cleaning of membrane which ultimately shorten the membrane's life span.

### 2.2.2 Physical Treatment

The physical treatment is one of the conventional treatment technologies used to treat dye molecules in dyestuff wastewater. Generally, it can be divided into three major process for the physical processes, such as filtration, coagulation-flocculation (co-floc) and adsorption (Holkar, et al, 2016). Among the three processes, co-floc is the most applicable techniques employed in treatment as it is the cheapest process. Due to its weakness in low removal efficiency for highly soluble dye molecules, the adsorption served to be employed for higher dye removal efficiency. In typical wastewater treatment and water purification process, activated carbon (AC) is the most applicable adsorbent used to adsorbed voluminous pollutants. AC had gained interest of numerous researchers due to its high adsorption capacity towards dye adsorption. Yang and co-workers (2021) investigated the AC modified with xanthate to remove various synthetic cationic dyes had achieved remarkable results. The removal efficiencies for cationic dyes malachite green (MG), methylene blue (MB) and crystal violet (CV) were 99%, 90% and 91%, respectively. Nonetheless, the drawbacks of AC in large scale wastewater treatment including low regeneration capability and high production cost of AC, leading to searching for alternative effective adsorbent rather than AC.

The low-cost alkali-activated sand synthesized by Sharma, et al. (2019) for the adsorption of dyestuff wastewater collected after the co-floc process was conducted. In their study, the alkali-activated sand had achieved notable adsorption efficiency of real textile wastewater at 70%. The utilizing of sand as effective adsorption over the AC due to several reasons, including low production cost, remarkably mechanical resistance, high adsorption capacity, and good regeneration to be reused. Nevertheless, the use of adsorbent for the removal of dyestuffs only transfers the liquid pollutants into solid pollutants as these molecules remained undegraded and stayed on the adsorbent. As a result, secondary pollutants were generated, and higher treatment cost is needed for the disposal of these sludge.

### 2.2.3 Chemical Treatment

The chemical process for wastewater treatment generally refers to the oxidation and reduction of pollutants to less harmful forms. The chemical treatments, including the ion exchange, chemical coagulation (CC), electrocoagulation (EC), catalysis, and redox reaction. The addition of chemical coagulant to wastewater was claimed to achieve high removal efficiency. A study carried out by GilPavas and co-workers (2018) treating the dyestuff wastewater via the sequential chemical coagulation using the conventional coagulants, aluminium sulphate followed by the electrooxidation (EO) to further polishing the effluent. The results showed that high colour removal efficiency was obtained after the chemical coagulation at 97% with moderately COD and TOC removal efficiency at 53% and 24%, respectively. Subsequently, the effluent treated with CC was underwent the electrolysis to further polishing the effluent to better quality. From their studies, improved effluent quality was achieved for colour, COD and TOC at 100%, 90% and 70%, respectively.

On the other hand, the employment of EC accompanied with ozonation of dyestuff wastewater was studied by Bilinska, et al. (2020). In their works, the iron electrode was used to generate in situ electro-coagulant at a current density of  $5\text{ A m}^{-2}$ . A notable result was obtained with colour removal efficiency at 84%. However, moderate COD and TOC removal efficiency was observed. Afterwards, the EC treated wastewater was underwent the ozonation and more than 90% colour removal was attained. There are some disadvantages of applying chemical treatment process for dyestuff wastewater. The chemical treatment generally required high cost to synthesis and fabricate, selectivity of chemical coagulants in removal of dye molecules, and possible secondary pollutants generated as sludge or flocs.

## 2.3 Advanced Oxidation Process

Advanced oxidation processes (AOPs) have been widely applied in wastewater treatment for the degradation of various inorganic and persistent organic compounds due to the highly oxidative potential species. The AOPs involved the generation of

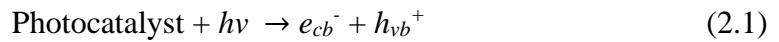
reactive species (ROS) to completely mineralized contaminants to yield carbon dioxide (CO<sub>2</sub>) and water molecule (H<sub>2</sub>O). The major ROS generated via the AOPs including hydroxyl radicals ( $\bullet\text{OH}$ ), sulphate radicals ( $\text{SO}_4\bullet^-$ ) and superoxide anion radicals ( $\bullet\text{O}_2^-$ ) (Bhat and Gogate, 2021; Ma, et al., 2021). Among these radicals,  $\bullet\text{OH}$  with strong oxidative potential at 2.8 eV played the significant role in the degradation of organic and inorganic constituents. The AOPs which generate reactive radicals such as Electron-Fenton and Fenton process, Photo-Fenton process, electrochemical process, ozonation, peroxone-process (O<sub>3</sub>/H<sub>2</sub>O<sub>2</sub>), gamma irradiation, photocatalytic oxidation reaction and UV-based process (Bethi, et al., 2016; Dewil, et a., 2016; Miklos, et al., 2018; Corona-Bautista, et al., 2021).

In recent years, the AOPs had popularity in wastewater treatment over the conventional wastewater treatment technologies due to the advantages of the AOPs. The advantages such as effectively degrade recalcitrant organic components with less production of toxic intermediates. Among the AOPs technology, heterogeneous semiconductor photocatalytic process under light irradiation was more promising technology used due to numerous of advantages. The advantages of heterogeneous photocatalysis are shown as follow (Byrne, Subramanian and Pillai, 2018; Kanakaraju, Glass and Oelgemoller, 2018; Kausley, et al., 2018; Corona-Bautista, et al., 2021; Ma, et al., 2021):

- i. The reaction can be conducted under ambient condition,
- ii. The generation of highly reactive oxygen species such as hydroxyl ( $\bullet\text{OH}$ ) radicals and superoxide anion ( $\text{O}_2\bullet^-$ ) radicals to completely mineralized organic and inorganic ions,
- iii. Absent of sludge generation which leads to secondary pollutions,
- iv. Low cost of semiconductor used as the photocatalyst in heterogeneous photocatalysis, and
- v. A broad range of industrial wastewater treatment applications including textile, pharmaceutical and petroleum-containing wastewaters.

### 2.3.1 Principle of Heterogeneous Photocatalysis

In generally, the photo-activated semiconductor or commonly known as photocatalyst, under light irradiation, the photogenerated electrons ( $e^-$ ) will be excited from the valence band (VB) of the photocatalyst. The photogenerated  $e^-$  will then jump to the conductive band (CB) of the photocatalyst, leaving vacancy ( $h^+$ ) in the VB (Khalik, et al., 2017). This induces the generation of electron-hole pairs ( $e_{cb}^- - h_{vb}^+$ ) as represented in Eq. (2.1). In the aqueous solution, the  $h^+$  oxidize hydroxide ion ( $OH^-$ ) in water molecule ( $H_2O$ ) and generating  $\bullet OH$  radicals which represented in Eqs. (2.2) to (2.3) (Kosera, et al., 2017; Ariyanti, Maillot and Gao, 2018; Zhang, et al., 2018a). In contrast, the recombination of  $e_{cb}^- - h_{vb}^+$  pairs could be also occurred, and release heat as showed in Eq. (2.4) (Al-Mamum, et al., 2019).



In addition, the  $e_{cb}^-$  would react with oxygen ( $O_2$ ) to generate superoxide radicals ( $O_2^{\bullet -}$ ) and subsequently other oxidant species including hydroperoxyl radicals ( $HO_2^{\bullet}$ ) and hydrogen peroxide ( $H_2O_2$ ) that will contribute to the generation of  $\bullet OH$  radicals as shown in Eqs. (2.5) to (2.8) (Kosera, et al., 2017; Ariyanti, Maillot and Gao, 2018; Hasanpour and Hatami, 2020; Ma, et al., 2021a).



The generated  $\bullet OH$  radicals and  $h_{vb}^+$  able to degrade various organic compounds in the surface of the photocatalyst as represented by the Eqs. (2.9) and (2.10) (Ma, et al., 2021a). Figure 2.1 illustrates of the basic mechanism of photocatalysis excitation which initiated by irradiation of UV.

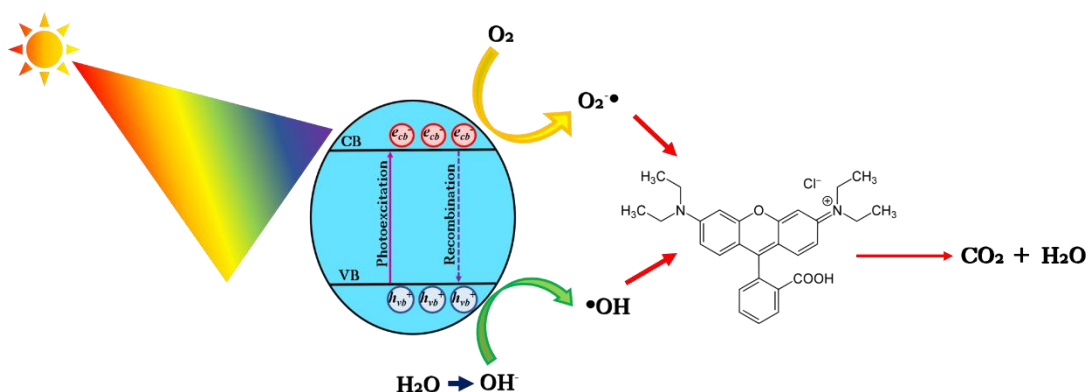
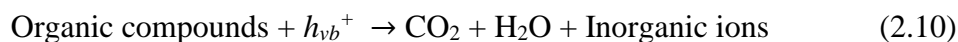
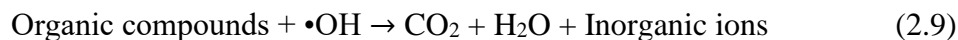


**Figure 2.3: Basic Mechanism of Photocatalyst Excitation under light irradiation (Jayaraj and Paramasivam, 2018)**

The semiconductor photocatalysis has been used in numerous organic decompositions, including the dyestuff wastewater, pharmaceutical waste, tannery wastewater, palm oil mill effluent (POME), and greywater (Ismael, 2020; Lam, et al., 2020; Ng, et al., 2020; Korpe and Rao, 2021; Paumo, et al., 2021). In a literature study, Chankhanittha and Nanan (2021) had developed ZnO/ bismuth molybdate ( $\text{ZnO}/\text{Bi}_2\text{MoO}_6$ ) heterostructure for degrading ofloxacin (OFL), a common antibiotic found in pharmaceutical wastewater under visible light irradiation. In their works, the composites had achieved remarkable degradation efficiency of 94% after 120 mins. Moreover, Yashni and co-workers (2020) had studied the photocatalytic degradation of greywater using the developed ZnO nanoparticles (NPs). In their studies, 100 mg of ZnO NPs had attained a high greywater degradation efficiency at 74.48 % under UV light radiation. Additionally, Li, et al. (2021b) had constructed RhB-sensitized bismuth oxyhalides ( $\text{BiOClBr}$ ) for degrading 2,4,6-trichlorophenol. Under Xe lamp irradiation, the composites catalyst obtained a notable degradation efficiency of 92.3 % in 80 mins. As a consequence, the photocatalysis technology could be applied in various organic degradation as described.

### 2.3.2 V<sub>2</sub>O<sub>5</sub> Single Photocatalyst

The photocatalysis utilizing nano size photo-activated semiconductors, particularly metal oxide to generate the  $e_{cb}^- + h_{vb}^+$  pairs for achieving mineralization of contaminants. The reported metal oxides, such as tungsten oxide (WO<sub>3</sub>), titanium dioxide (TiO<sub>2</sub>), cuprous oxide (Cu<sub>2</sub>O), zinc oxide (ZnO), tin dioxide (SnO<sub>2</sub>), cerium oxide (CeO<sub>2</sub>) and vanadium pentoxide (V<sub>2</sub>O<sub>5</sub>) (Hasanpour and Hatami, 2020; Truong, et al., 2020). Among these metal oxides, ZnO (band gap  $\approx$  3.2 eV) and TiO<sub>2</sub> (band gap = 3.0 – 3.2 eV) have been widely applied in photocatalytic wastewater treatment, water splitting, carbon dioxide (CO<sub>2</sub>) reduction and many other applications (Truong, et al., 2020; Korpe and Rao, 2021). However, both photocatalysts are active under the ultraviolet light (UV) region, due to its large band gap energy. The sunlight spectrum contains less than 5% of the UV light and they are not responsive in the visible light region which accounted more than 45% of the total solar spectrum (Jayaraj, et al., 2018; Jayaraj and Paramasivam, 2019). Consequently, the visible light driven photocatalyst had becoming researchers' focus for photocatalytic applications.

The narrow band gap photocatalyst, such as copper oxide (CuO), cuprous oxide (Cu<sub>2</sub>O), manganese oxide (MnO<sub>2</sub>), vanadium dioxide (VO<sub>2</sub>), and vanadium pentoxide (V<sub>2</sub>O<sub>5</sub>) had been used as visible light driven photocatalyst to effectively photodegrading organic compounds in wastewater (Kwon, et al., 2020). Among the visible-light activating photocatalyst, V<sub>2</sub>O<sub>5</sub> has the advantages as a n-type semiconductor with low band gap ranging from 2.4 to 2.8 eV, good photo and chemical stability, non-toxic, large surface area, easily synthesized, and high visible light absorption (Jayaraj, et al., 2018; Jayaraj and Paramasivam, 2019). Owing to its excellent properties, V<sub>2</sub>O<sub>5</sub> have been widely adopted for the application, such as photocatalysis, high performance cathode material for lithium-ion batteries, pseudocapacitive charge storage devices, and gas sensors (Zeng, et al., 2019; Qian, et al., 2020; Rafique, et al., 2020; Sajid, et al., 2020; Singh, Kumar and Vaish, 2021). However, the single visible-light driven photocatalyst has its drawback as narrow band gap promoting fast recombination rate of the photogenerated  $e_{cb}^- - h_{vb}^+$  pairs and produce heat in the reaction (Dadigala, et al., 2019).

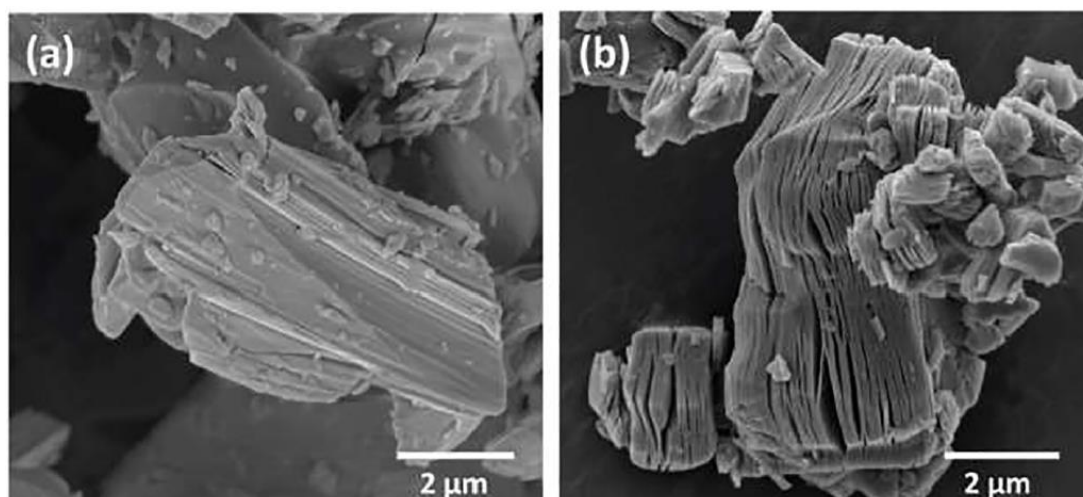
### 2.3.3 NiFe<sub>2</sub>O<sub>4</sub>/V<sub>2</sub>O<sub>5</sub> Binary Photocatalyst

As aforementioned, the drawbacks of utilizing narrow V<sub>2</sub>O<sub>5</sub> as single semiconductor photocatalyst in degrading pollutants including the fast recombination rate due to the small bandgap, and the difficulty of this material to be recovered and reused which may induce the generation of secondary pollutants. Thus, the adoption of single photocatalyst has limited its application in real industrial wastewater treatment system. To overcome the abovementioned shortcomings of single photocatalyst, the construction of heterojunction photocatalyst with another metal oxide is introduced (Zhao, et al., 2021). However, the binary photocatalyst can only resolve the recombination problem, the recovery of the used photocatalyst is still low. Therefore, the narrow bandgap ferromagnetic based photocatalyst has gained researchers' interest. Nickel ferrite (NiFe<sub>2</sub>O<sub>4</sub>) nanoparticle has great magnetic and electronic properties with narrow bandgap between 1.56 to 2.19 eV which possesses broad range of light absorption, low toxicity, and good resistance in photo-corrosion (Faraji, et al., 2021; Veisi, et al., 2021). In addition to the improvement of the separation of the photogenerated  $e_{cb}^- - h_{vb}^+$  pairs, the incorporation of NiFe<sub>2</sub>O<sub>4</sub> with V<sub>2</sub>O<sub>5</sub> to construct a binary composite can be recovered and collected easily through the external magnetic field due to the magnetic property of NiFe<sub>2</sub>O<sub>4</sub>. Therefore, the preparation of this composite material is capable to improve the photocatalytic activities by reducing the recombination rate of  $e_{cb}^- - h_{vb}^+$  pairs together with the high recovery and reusability of binary photocatalyst via external magnetism (Xie, et al., 2021; Zeng, et al., 2021).

### 2.3.4 MXene-based Catalyst

In literatures, incorporation of co-catalysts on the binary composites, including can further enhance the  $e_{cb}^- - h_{vb}^+$  separation efficiently (Prasad, et al., 2020). The co-catalysts not only can be served as the electron sink to facilitate the charge separation, but also provide numerous active sites and functional groups for redox reactions (Cai, et al., 2018; Li, et al., 2021a). The typical noble metals are gold (Au), silver (Ag), and platinum (Pt) have been adopted as promising co-catalysts in photocatalytic degradation of various pollutants (Sun, et al., 2019; Li, et al., 2020). Nonetheless, these

noble metals are expensive and exist in trace amount. MXenes are new 2D transition metal nitrides/carbides which founded in 2011 with general formula of  $M_{n+1}X_nT_x$  (Bu, et al., 2020; Prasad, et al., 2020; Li, et al., 2021a; Shen, et al., 2021). M denotes as the early transition metal elements, X is element C or N and  $T_x$  represents the surface functional groups (OH, O and F). They are new promising 2D nanomaterials which derived from simple chemical etching of A element (IIIA or IVA elements) from MAX phase that could be adopted in numerous applications (Hu, Ding and Zhong, 2021; Xu, et al., 2021). They have been attracted interest as a non-noble-metal co-catalyst for photocatalytic applications including photocatalytic  $CO_2$  reduction, water splitting for generation of  $H_2$ , photocatalytic degradation of various organic pollutants, and many more applications (Zhuang, Liu and Meng, 2019; Cao, et al., 2020; Li, et al., 2020; Hu, Ding and Zhong, 2021; Hu, et al., 2021). The advantageous properties of MXene in composite materials, such as highly hydrophilicity, large surface area, improved charge separation abilities, good conductivity, and various surface functional groups for redox reactions (Sun, et al., 2019; Ihsanullah, 2020). The morphologies of typical  $Ti_3AlC_2$  MAX phase and  $Ti_3C_2$  MXene are depicted in Figures 2.4a and b. The MAX phase exists as stacked ternary compound with metallic bond between M (early transition metal) and A (Group 13 or Group 14 elements) and strong covalent/ionic/metallic forces between M-X (Venkateshalu and Grace, 2020). After the HF etching of A element, the MXene exists small intercalation between M-X.



**Figures 2.4: SEM imaged of (a)  $Ti_3AlC_2$  MAX and (b)  $Ti_3C_2$  MXene (Ihsanullah, 2020).**

Zhang and co-workers (2018b) fabricated 2D  $\alpha$ -ferric oxide ( $\text{Fe}_2\text{O}_3$ ) doped titanium carbide ( $\text{Ti}_3\text{C}_2$ ) MXene composite material via a simple dispersion in ultrasonic wave. Under the visible light irradiation, a notable high degradation efficiency of RhB was obtained at 98% within 2 hours. In another study, Shen et al. (2019) synthesized  $\text{Ti}_3\text{C}_2$  MXene based catalyst with cerium oxide ( $\text{CeO}_2$ ) through a hydrothermal treatment at  $180^\circ\text{C}$ . The as-prepared  $\text{CeO}_2/\text{Ti}_3\text{C}_2$  composite was achieved tetracycline (TC) degradation at 80% in 60 minutes under the visible light radiation. On the other hand, 2D/2D  $\text{Ti}_3\text{C}_2$ /porous g- $\text{C}_3\text{N}_4$  (PCN) composite was prepared by Liu and co-workers (2020a) through a simple continuous stirring. In their study, 98% of 10 mg/L phenol was degraded after 3 hours photocatalysis under visible light irradiation. Cui, et al. (2020) fabricated hybrid bismuth tungstate/niobium carbide ( $\text{Bi}_2\text{WO}_6/\text{Nb}_2\text{CT}_x$ ) via hydrothermal reaction for the degradation of RhB. Under visible light irradiation, the RhB degradation efficiency for the  $\text{Bi}_2\text{WO}_6/\text{Nb}_2\text{CT}_x$  composites was improved to 99.8% as compared to pristine  $\text{Bi}_2\text{WO}_6$  (90.1%) within 90 minutes. The enhancement of the composites was due to the greater interface contacts, subsequently improves the  $e_{cb}^- - h_{vb}^+$  separation for better photocatalytic activities.

Moreover, Cai and co-workers (2018) synthesized a Schottky catalyst, silver phosphate/ $\text{Ti}_3\text{C}_2$  MXene ( $\text{Ag}_3\text{PO}_4/\text{Ti}_3\text{C}_2$ ) using an electrostatic adsorption assisted by self-assembly method. In their studies, methyl orange (MO) with concentration of 20 ppm achieved 90% degradation efficiency in 30 minutes. Fang and co-workers (2019) prepared silver tungstate/  $\text{Ti}_3\text{C}_2$  Schottky composite ( $\text{Ag}_2\text{WO}_4/\text{Ti}_3\text{C}_2$ ) through electrostatic traction. In their studies, the degradation efficiency for 20 mg/L sulfadimidine (SFE) was achieved at 88.6% using the  $\text{Ag}_2\text{WO}_4/\text{Ti}_3\text{C}_2$  composites while only 12% removal efficiency was obtained from the bare  $\text{Ag}_2\text{WO}_4$  in 40 minutes under the visible light radiation. The significant improvement by the coupling of MXene was due to the formation of Schottky junction between the  $\text{Ag}_2\text{WO}_4$  and  $\text{Ti}_3\text{C}_2$  interface. The creation of a built-in electrical field promoted the electrons transfer from  $\text{Ag}_2\text{WO}_4$  to  $\text{Ti}_3\text{C}_2$ , resulted in higher photocatalytic performance. Table 2.2 depicts the various MXene based catalysts with their synthesis methods associated with the degradation efficiency of organic pollutants.

**Table 2.2: The Synthesis of Various MXene-based Catalyst with Respective Degradation Efficiency.**

MXene composite		Synthesis method	Pollutant (mg/L)	Light source	MXene loading (wt%)	Performance	Reference
MAX phase	MXene type						
Ti <sub>3</sub> AlC <sub>2</sub>	a-Fe <sub>2</sub> O <sub>3</sub> /Ti <sub>3</sub> C <sub>2</sub>	Simple dispersion in ultrasonic wave	RhB; 10	500 W Xe lamp with UV-cutoff ( $\lambda >$ 420 nm)	a-Fe <sub>2</sub> O <sub>3</sub> : MXene= 1:2	98% within 2 hours	Zhang, et al., 2018b
Ti <sub>3</sub> AlC <sub>2</sub>	CeO <sub>2</sub> / Ti <sub>3</sub> C <sub>2</sub>	Hydrothermal	TC; 10	350 W Xe lamp	1 g/L	80% in 60 minutes	Shen, et al., 2019
Ti <sub>3</sub> AlC <sub>2</sub>	Ti <sub>3</sub> C <sub>2</sub> /porous g- C <sub>3</sub> N <sub>4</sub>	Simple continuous stirring	Phenol; 10	500 W Xe lamp	0.4 g/L	98% within 3 hours	Liu, et al., 2020a
Nb <sub>2</sub> AlC	Bi <sub>2</sub> WO <sub>6</sub> /Nb <sub>2</sub> CT <sub>x</sub>	Hydrothermal	RhB; 15	500 W Xe lamp	0.5 g/L	99.8% in 90 minutes	Cui, et al., 2020
Ti <sub>3</sub> AlC <sub>2</sub>	Ag <sub>3</sub> PO <sub>4</sub> /Ti <sub>3</sub> C <sub>2</sub>	Electrostatic adsorption assisted by self-assembly	MO; 20	300 W Xe lamp with cutoff filter ( $\lambda >$ 420 nm)	0.4 g/L	> 90% within 30 minutes	Cai, et al., 2018
Ti <sub>3</sub> AlC <sub>2</sub>	Ag <sub>2</sub> WO <sub>4</sub> /Ti <sub>3</sub> C <sub>2</sub>	Electrostatic traction	SFE; 20	300 W Xe lamp	20 mg	88.6% in 40 minutes	Fang, Cao and Chen, 2019

### 2.3.5 $\text{Ti}_3\text{C}_2\text{-NiFe}_2\text{O}_4/\text{V}_2\text{O}_5$ Ternary Photocatalytic Mechanisms

The ternary photocatalytic mechanism was proposed as depicted in Figure 2.5. According to the literatures, the approximate valence band ( $E_{\text{VB}}$ ) of  $\text{NiFe}_2\text{O}_4$  and  $\text{V}_2\text{O}_5$  are -0.57 eV and 0.47 eV, respectively (Jayaraj, et al., 2018; Cui, et al., 2019; Zhao, et al., 2021). Meanwhile, the conductive band ( $E_{\text{CB}}$ ) for both catalysts was 1.07 eV and 2.73 eV, correspondingly. The  $E_{\text{CB}}$  of  $\text{NiFe}_2\text{O}_4$  is more negative than the potential of  $\text{O}_2/\bullet\text{O}_2^-$  (-0.33 eV) (Veisi, et al., 2021). Under the light irradiation, the  $e_{\text{CB}}^-$  will be generated at CB leaving  $h_{\text{VB}}^+$  at VB and react with molecular oxygen ( $\text{O}_2$ ) in aqueous to form superoxide anion radicals ( $\bullet\text{O}_2^-$ ) (Xie, et al., 2021). However, the  $E_{\text{CB}}$  of  $\text{V}_2\text{O}_5$  is more positive, no  $\bullet\text{O}_2^-$  will be generated. Furthermore, the photogenerated  $e_{\text{CB}}^-$  in  $\text{NiFe}_2\text{O}_4$  will be transported to the more positive  $E_{\text{CB}}$  of  $\text{V}_2\text{O}_5$ . On the other hand, the  $E_{\text{VB}}$  of the of  $\text{V}_2\text{O}_5$  is more positive than the potential  $\bullet\text{OH}/\text{OH}^-$  (1.99 eV) and  $\bullet\text{OH}/\text{H}_2\text{O}$  (2.27 eV) (Kwon, et al., 2020; Zhang, et al., 2021a). More hydroxyl radicals ( $\bullet\text{OH}$ ) will be produced at the CB. Subsequently, the  $h_{\text{VB}}^+$  will be travelled to the less positive VB of  $\text{NiFe}_2\text{O}_4$ . The transferring of  $h_{\text{VB}}^+$  and  $e_{\text{CB}}^-$  will improve the  $e_{\text{cb}}^- - h_{\text{vb}}^+$  separation for better photocatalytic activities (Xie, et al., 2021; Zhao, et al., 2021). The radicals generated with high redox potential responsible for degrading RhB dye molecule and perform antimicrobial activities toward *E. coli* and *A. Niger*. Lastly, the  $\text{Ti}_3\text{C}_2$  serves as a co-catalyst which further improve the charge carrier separation (Yang, et al., 2020). The photogenerated  $e_{\text{CB}}^-$  from the CB of  $\text{V}_2\text{O}_5$  will move to this co-catalyst. This may promote the charge separation and reduce the recombination rate of the catalyst (Sun, et al., 2019; Liu, et al., 2020a; Li, et al., 2021a). Hence, the ternary  $\text{Ti}_3\text{C}_2\text{-NiFe}_2\text{O}_4/\text{V}_2\text{O}_5$  composites may exhibit excellent photocatalytic performance.

## 2.4 Process Parameter Studies

In the photocatalytic wastewater treatment process, there were various process parameters that have been configured to study the performance, such as the initial pollutant concentration, solution pH, catalyst loading, dopant content, types of scavenger, light source, light intensity, and additional of electrolyte (Hasanpour and Hatami, 2020; Chankhanittha and Nanan, 2021; Elbadawy, et al., 2021; Rafiq, et al.,

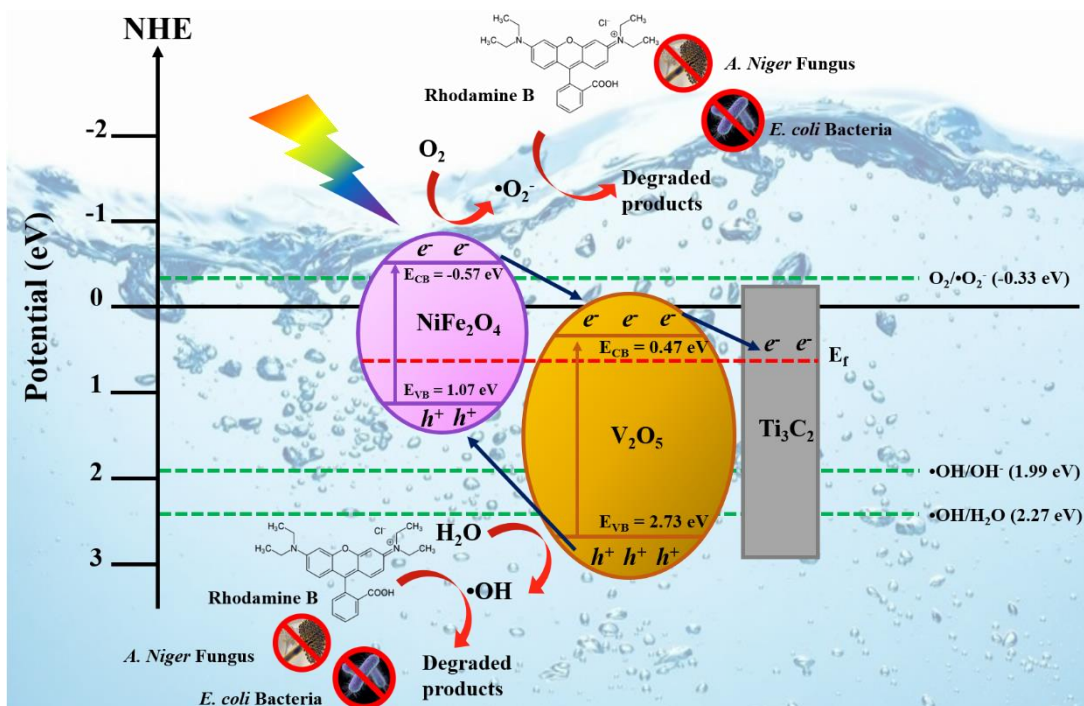


**Figure 2.5: The Photocatalytic Mechanism of Ternary Ti<sub>3</sub>C<sub>2</sub>-NiFe<sub>2</sub>O<sub>4</sub>/V<sub>2</sub>O<sub>5</sub> Composites.**

2021). In the present study, the process parameters including the co-catalyst contents, the catalyst loading, and the pH of solution.

#### 2.4.1 Co-catalyst loading

The contents of co-catalyst to be incorporated to semiconductor photocatalyst has great effect to the photocatalytic performance. Doping of small amount of co-catalyst could promote the  $e_{cb}^- - h_{vb}^+$  pairs separation as it is a conductor that may form Schottky junction with semiconductors (Li, et al., 2021a). The increase in the amount of co-catalyst may improve the photocatalytic activities. However, overdosage of co-catalyst will significantly declines the photocatalytic performance. This is due to the excessive amount of co-catalyst may cover the photoactivated semiconductor from light irradiation for photocatalytic activities (Zhuang, Liu and Meng, 2019; Yang, et al., 2020).

Zhuang and co-workers (2019) had synthesized TiO<sub>2</sub>/Ti<sub>3</sub>C<sub>2</sub> composites via electrostatic assembly technique to be applied in photocatalytic H<sub>2</sub> generation. In their

studies, the varying amount of  $\text{Ti}_3\text{C}_2$  MXene from 1 wt% to 3 wt% had achieved  $\text{H}_2$  production of  $4.257 \text{ mmol h}^{-1}\text{g}^{-1}$  to  $6.979 \text{ mmol h}^{-1}\text{g}^{-1}$  in 3 hours. Further increase in the  $\text{Ti}_3\text{C}_2$  content to 5 wt%, the photocatalytic  $\text{H}_2$  production had reduced to  $5.265 \text{ mmol h}^{-1}\text{g}^{-1}$ . The decrease in the photocatalytic performance was due to the excess  $\text{Ti}_3\text{C}_2$  quantities which restricted the light penetration that reach on the  $\text{TiO}_2$  surface. Similar findings were reported by Liu, et al. (2020a) that the excess co-catalyst can inhibit the photocatalytic activities. Liu and colleagues had prepared the  $\text{Ti}_3\text{C}_2$ /porous g- $\text{C}_3\text{N}_4$  (PCN) composite through continuous stirring followed by vacuum filtration. Under visible light irradiation, the increase of the  $\text{Ti}_3\text{C}_2$  amount from 10 wt% to 20 wt% had enhanced the photodegradation of phenol from 70.4% to 98%. This can be ascribed that the photogenerated  $e_{cb}^- - h_{vb}^+$  pairs are well separated by the heterojunction between  $\text{Ti}_3\text{C}_2$  and PCN photocatalyst. When the weight percentage of  $\text{Ti}_3\text{C}_2$  increased to 50%, the photocatalytic activity had significantly diminished. This revealed that excess  $\text{Ti}_3\text{C}_2$  prevent the light radiation to the PCN photocatalyst and restricted the formation of  $e_{cb}^- - h_{vb}^+$  pairs for photocatalytic process.

#### 2.4.2 Catalyst Loading

The photocatalyst loading is one of the dominant process parameters that directly affect the photocatalytic activities. The increase in the catalyst loading will increase the photocatalytic degradation efficiency of pollutants (Frindy and Sillanpää, 2020; Hasanpour and Hatami, 2020; Rafique, et al., 2020). Numerous studies were conducted to examine the effect of catalyst loading in photocatalytic performance. Based on the literature reports, the loading of catalyst will affect the generation of ROS and the absorptivity of light in aqueous (Vattikuti, et al., 2018; Zeleke and Kuo, 2019; Vigneshwaran, et al., 2021; Xie, et al., 2021; Zhao, et al., 2021). The photocatalytic degradation of contaminants increased with the photocatalyst dosage as more active sites on photocatalyst surface responsible, leading to increase of the generation of reactive radicals (Shah, Jan and Khitab, 2018; Rafique, et al., 2020; Ghorai, et al., 2021). However, the excess catalyst loading may deteriorate the photocatalytic degradation performance. The excessive amount of photocatalyst will intensify the aggregation of catalyst which leading to the depletion of photocatalyst active site for generation of

reactive radicals. Moreover, the overdosage of catalyst will lower the light intensity that penetrate to the aqueous solution in addition to the scattering of light by the high turbidity solution. Consequently, the photocatalyst may receive minimum light due to the shielding effect which obstruct the photoexcitation process for the generation of  $e_{cb}^-$  -  $h_{vb}^+$  pairs (Mishra, et al., 2020). Subsequently, the recombination will occur and resulted in poor photocatalytic activities.

In another study, Chankhanitta and Nanan (2021) had constructed the zinc oxide/bismuth molybdate ( $ZnO/Bi_2MoO_6$ ) composites through a solvothermal technique. In their studies, the increase in the composite amount from 25 mg to 50 mg in degrading 10 ppm of RhB dye under the visible light irradiation, the degradation efficiency had enhanced from 45% to 92% within 180 mins. When the catalyst loading was further increased to 75 mg, a slight reduction in photocatalytic degradation efficiency to 88%. This can be ascribed that the increasing of catalyst dosage had increased the turbidity of solution which lowered the penetration of visible light and the scattering of light. As a result, the generation of ROS for degrading RhB dye was reduced. The significant deterioration in the photocatalytic performance was due to the observable turbidity of solution which preventing the light penetration together with the light scattering by suspended catalyst. The shielding effect caused small number of active sites for photocatalytic activities.

Furthermore, the increase in the catalyst loading has significant effect on the photocatalytic antimicrobial performance (Mydeen, et al., 2020; Mukhtar, et al., 2021). Mukhtar and co-workers (2021) had synthesized dual S-scheme  $ZnO-V_2O_5-WO_3$  nanocomposites via facile co-precipitation method to test its antimicrobial activities against *S. aureus*, *K. pneumoniae*, *P. aeruginosa*, and *P. Vulgaris*. In their studies, the increase in the nanocomposites concentration ranging from 1  $\mu\text{g/mL}$  to 3  $\mu\text{g/mL}$ , the bacteria zone of inhibition (ZOI) measurement also increases significantly. The synthesized nanocomposites had the most considerable antimicrobial effect against *K. pneumoniae* with an improved ZOI measurement of 11 mm to 20 mm when the catalyst concentration increases from 1  $\mu\text{g/mL}$  to 3  $\mu\text{g/mL}$ . This could be ascribed that higher catalyst concentration provided more direct interaction with bacteria cell and ruptures the bacteria cell wall (Balasurya, et al., 2021). The enhanced antimicrobial activities with the increased of catalyst concentration could be the mechanisms including, the

production of more ROS, the generation of dense metal ions which causes the penetration of cations in bacteria cell membrane, and the shape of nanoparticles for easy destruct the cell membrane (Mydeen, et al., 2020; Mukhtar, et al., 2021; Nivetha, Kavitha and Kalanithi, 2021).

### 2.4.3 Solution pH

The pH of the solution has great influence on the photocatalytic degradation of different pollutants. Different semiconductors were used for the photocatalysis process may have different surface properties. These properties including the band edge position, degree of dissociation, and the surface charges are significantly affected by the pH of solution. There are many literature studies have been conducted and proving that the different solution pH causing different photodegradation rate (Hasanpour and Hatami, 2020; Kumar, et al., 2020; Zhao, et al., 2021). In the photodegradation of dye molecules, the pH of solution has direct influence on the surface interaction. A literature study reported by Li, et al (2018) in treating the anionic dye molecule, such as the mordant orange (MO), the increase in the pH of solution from 2.8 to 10.7, the decolourization efficiency was reduced from 90% to 77%. This can be ascribed that in the acidic condition, the surface of the catalyst existed as positively charge. Strong electrostatic interaction between anionic molecules with positively charged catalyst had improved the adsorption of dyes and facilitate the photocatalytic degradation.

Furthermore, Chen and co-workers (2020) had carried out the photocatalytic degradation of 10 mg/L RhB dye using the carbon nanotube-TiO<sub>2</sub> (CNT-TiO<sub>2</sub>) synthesized via sol reflux method. By varying the solution pH from 2 to 10, the photodegradation efficiency had declined 100% to 88%. They explained that the better photocatalytic performance in acidic environment was due to the generation of hydroperoxyl ions (HO<sub>2</sub><sup>-</sup>) which leading to the generation of more •OH radicals. On the other hand, a research conducted by Singh and Basu (2020), treating the cationic RhB dye through the magnetic Fe<sub>2</sub>O<sub>3</sub>/g-C<sub>3</sub>N<sub>4</sub> under the visible light irradiation. According to the results, the increase in the pH value from 1 to 9, an increasing trend in the photocatalytic degradation of RhB was obtained. The remarkable degradation

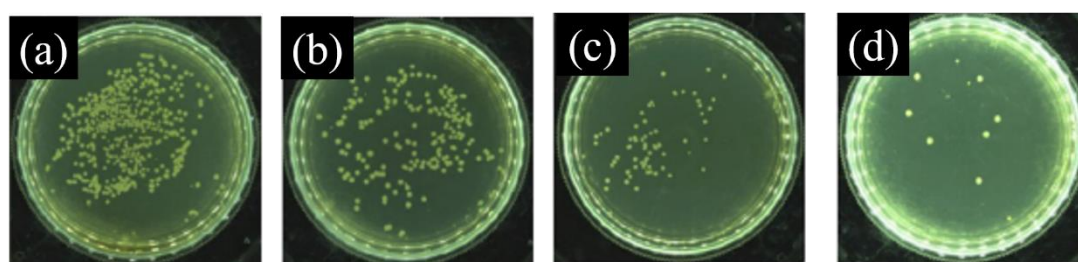
of RhB was observed at pH 9 with efficiency of 98.2%. This revealed that the cationic RhB<sup>+</sup> molecules performed strong electrostatic repulsion from the photocatalyst with positively charged surface at acidic condition. At pH 9, the deprotonation of RhB leading to high photocatalytic performance. Additionally, the basic environment promoting the formation of •OH radicals which facilitate the degradation of RhB. However, the further increase of solution pH showed declination in the degradation efficiency. This could be attributed to the formation of metal hydroxide that covered the photocatalyst surface and limited the active sites for the reaction.

## 2.5 Photocatalytic Antimicrobial Studies

There are various microorganism's species exist in water and wastewater effluent. Generally, the pathogenic microorganisms could be classified into viruses, fungi, gram-positive and gram-negative bacteria. The most common gram-negative bacteria cause numerous types of diseases, such as *E. coli* (diarrhoea, severe illness), *P. aeruginosa* (respiratory infections, urinary tract and gastrointestinal infections), *K. pneumoniae* (pneumonia, meningitis, wound or surgical site infections), and *P. Vulgaris* (bloodstream or respiratory tract infections, wound infections) (Kumar, et al., 2021; Mukhtar, et al., 2021; Shi, et al., 2021). As the gram-negative bacteria species, *S. aureus* may cause cellulitis, endocarditis, pneumonia, and skin infections (Mukhtar, et al., 2021). In addition, *Aspergillus* is fungus species which could be found in soil, air and surface water. It may cause allergic diseases, respiratory infections and generate toxic metabolites (aflatoxins) that will affect human health (Sun, et al., 2021a; Zhang, et al., 2021b). The conventional disinfection methods, including UV disinfection, ozonation, chlorination, adsorption and filtration. However, these methods have the disadvantages, such as higher cost, generation of carcinogenic and harmful by-products and the sludge production may induce the secondary pollution (Wang, et al., 2020; Roshith, et al., 2021). Therefore, the photocatalysis has becoming a promising technology for the inactivation of pathogenic microorganisms.

Basically, the antimicrobial mechanisms could be the direct contact of the metal ions, the resistance of the bacterial adhesion via hydrophobic interface and

electrostatic repulsion, cell membrane rupture by sharp edges nanoparticle, and most significantly the generation of ROS that destruct the bacterial cell membranes through oxidation (Tshangana, et al., 2020; Liu, et al., 2021a; Wang, et al., 2021a). The antimicrobial activities could be determined through the measurement of the zone of inhibition (ZOI) or the colony counting method on plate which observed under a fluorescence microscope (Quek, et al., 2018; Tshangana, et al., 2020; Wang, et al., 2020; Roshith, et al., 2021). Jaffari, et al. (2019b) synthesized silver decorated bismuth ferrite (Ag-BiFeO<sub>3</sub>) photocatalyst and study the photocatalytic antibacterial activity of the as-synthesized photocatalyst. In their study, the zone of inhibition (ZOI) was conducted towards the *E. coli* and *M. luteus* bacteria under visible irradiation. They found that the ZOIs for *E. coli* and *M. luteus* were 28 mm and 32 mm, respectively. Moreover, Wang and co-workers (2020) conducted the photocatalytic disinfection of *S. aureus* using the synthesized cuprous oxide anchored MXene (Cu<sub>2</sub>O/MXene). The inactivation of bacteria can be observed through the photographs. Less bacteria stains were obtained for both bacteria colonies when the Cu<sub>2</sub>O/MXene composites were used as compared to pristine MXene or Cu<sub>2</sub>O. Figures 2.6 (a) and (d) illustrate the antimicrobial activities in different conditions. The enhancement of the antimicrobial activities was attributed to the synergistic effect of the direct interaction of sharp edges MXene to bacteria membrane, and the generation of Cu<sup>+</sup> and Cu<sup>2+</sup> ions by the Cu<sub>2</sub>O posed toxicity effect to the bacteria through the denaturing of bacteria DNA.



**Figures 2.6: Inactivation of *S. aureus* Bacteria in (a) Control, (b) Pristine MXene, (c) Bare Cu<sub>2</sub>O, and (d) Cu<sub>2</sub>O/MXene composites (Wang, et al., 2020).**

## 2.6 Summary

The characteristics of the dyestuff wastewater has been first discussed in this chapter. It was then followed by numerous treatment technologies reported in treating the real dyestuff wastewater. Each of the treatment technologies had different levels of success in eliminating the contaminants in wastewater. The principle and working mechanism of the heterogeneous photocatalysis was also stated to understand on the process. Small bandgap  $V_2O_5$  photocatalyst is a promising candidate in photocatalysis as it can be activated under visible light irradiation. Owing to the limitations of  $V_2O_5$ , incorporation the ferromagnetic  $NiFe_2O_4$  with  $V_2O_5$  to form the binary photocatalysts was also proposed the first time in this study. The advantages of  $NiFe_2O_4$  in composite, including effective separation of  $e_{cb}^- - h_{vb}^+$  pairs along with the extension of recombination rate, ferromagnetic property of  $NiFe_2O_4$  allowed easy recovery of photocatalyst by external magnetic field, while the introduction of non-noble-metal  $Ti_3C_2$  as co-catalyst to couple with the binary  $NiFe_2O_4/V_2O_5$  to further enhance the separation of charge carriers. The effect of process parameters, such as the co-catalyst content, catalyst loading, and solution pH have been described as they were reported to significantly affect the photocatalytic activities. To the best of our knowledge, there are no report on the degradation of dyestuff wastewater and microbial inactivation using a ternary  $Ti_3C_2-NiFe_2O_4/V_2O_5$  composite under visible light irradiation. Therefore, the performance of  $Ti_3C_2-NiFe_2O_4/V_2O_5$  composite in treating dyestuff wastewater and antimicrobial towards *E. coli* and *A. Niger* will be evaluated in this study.

## **CHAPTER 3**

### **RESEARCH METHODOLOGY**

The experimental setup and methodology of the experiment was discussed in this chapter. A summary of the study is given by a flowchart in Figure 3.1.

#### **3.1 Chemicals and Materials**

All the chemicals used in this research study were under analytical grade with no further purification was performed before used. In this study, deionized water was utilized for the preparation of chemicals while ethanol was used as dispersing agent for the synthesis of composite materials. All chemicals used were listed in Table 3.1.

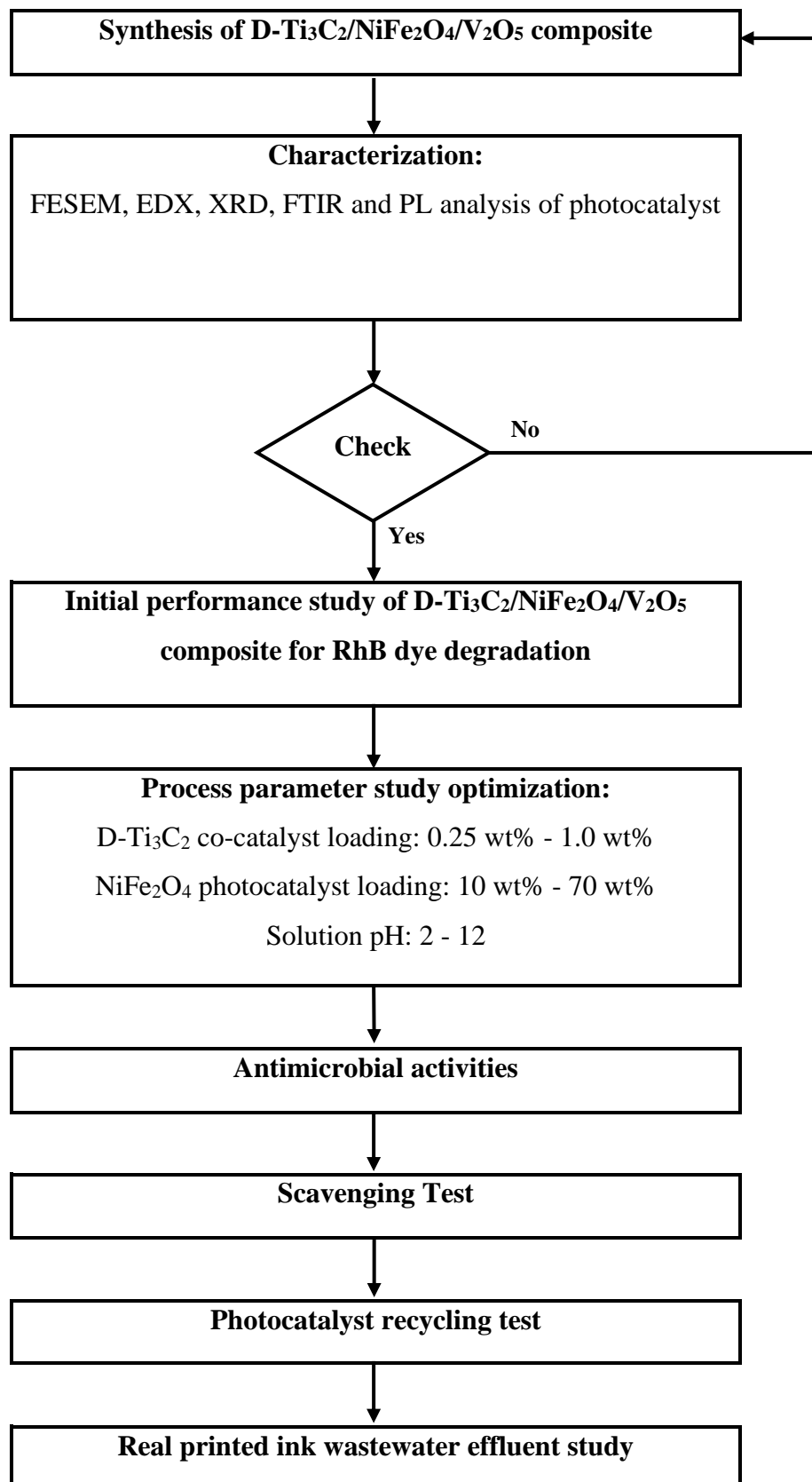


Figure 3.1: Flowchart of Experimental Work Involved in This Study.

**Table 3.1: Lists of Chemicals and Materials Used.**

<b>Chemicals/ Reagent</b>	<b>Purity (%)</b>	<b>Supplier</b>	<b>Purpose of Use</b>
Ammonium metavanadate (NH <sub>4</sub> VO <sub>3</sub> )	≥ 99	Merck	To synthesis V <sub>2</sub> O <sub>5</sub> photocatalyst.
Iron (III) nitrate nonahydrate (Fe(NO <sub>3</sub> ) <sub>3</sub> •9H <sub>2</sub> O)	98	GENE Chemical	To synthesis NiFe <sub>2</sub> O <sub>4</sub> photocatalyst.
Nickel (II) nitrate hexahydrate (Ni(NO <sub>3</sub> ) <sub>2</sub> •6H <sub>2</sub> O)	>97	SYSTEM	To synthesis NiFe <sub>2</sub> O <sub>4</sub> photocatalyst.
Titanium aluminium carbide (Ti <sub>3</sub> AlC <sub>2</sub> )	≥ 99	Shanghai Xinglu Chemical	To synthesis 2D nanosheet co-catalyst.
Hydrofluoric acid	40%	Merck	As etching solution for Ti <sub>3</sub> AlC <sub>2</sub> .
Tetramethylammonium hydroxide (TMAOH)	25%	Sigma Aldrich	To use as intercalation agent.
Hydrochloric acid (HCl)	37%	Merck	To adjust solution pH.
Sodium hydroxide (NaOH)	1M	Sigma Aldrich	To adjust solution pH.
Deionized water (DI)	Resistivity = 18.2 MΩ	NEW HUMAN UP	For the preparation of chemicals.
Ethanol (C <sub>2</sub> H <sub>5</sub> OH)	95	Medigene	To use as dispersing agent and disinfectant.
Rhodamine B (RhB)	≥ 90	Merck	Acts as the synthetic dye wastewater.
Escherichia coli ( <i>E. coli</i> )	-	Himedia	To culture bacteria.
Aspergillus Niger ( <i>A. Niger</i> )	-	TBC	To culture fungus.
Nutrient Broth	-	Himedia	To provide nutrient for bacteria.
Nutrient Agar	-	Himedia	As the culture medium.
Sodium chloride (NaCl)	85%	Gene Chemical	To dilute culture solution.
Sodium sulphate (Na <sub>2</sub> SO <sub>4</sub> )	0.5M	R & M Chemical	To use as electrolyte for photoelectrochemical testing.
Printed ink wastewater	-	-	To use as real dyestuff wastewater effluent for photocatalytic degradation study.

## 3.2 Apparatus and Equipment

### 3.2.1 Photocatalysis Experimental Apparatus

The photocatalytic degradation of rhodamine B dye under visible light irradiation was carried out in the fume hood with black cover. The experimental setup was in this study is depicted in Figure 3.2. The experimental setup included a magnetic stirrer plate with a beakers used as the photocatalytic reactor, one unit of a 150W indoor LED light bulb was used as the visible light source and a flow meter with air flow rate of 2 L/min to provide oxygen. Function of each device can discuss one-by-one after this sentence. The current form is too messy. The magnetic stirring rate was set at 300 rpm and run for 8 hours.

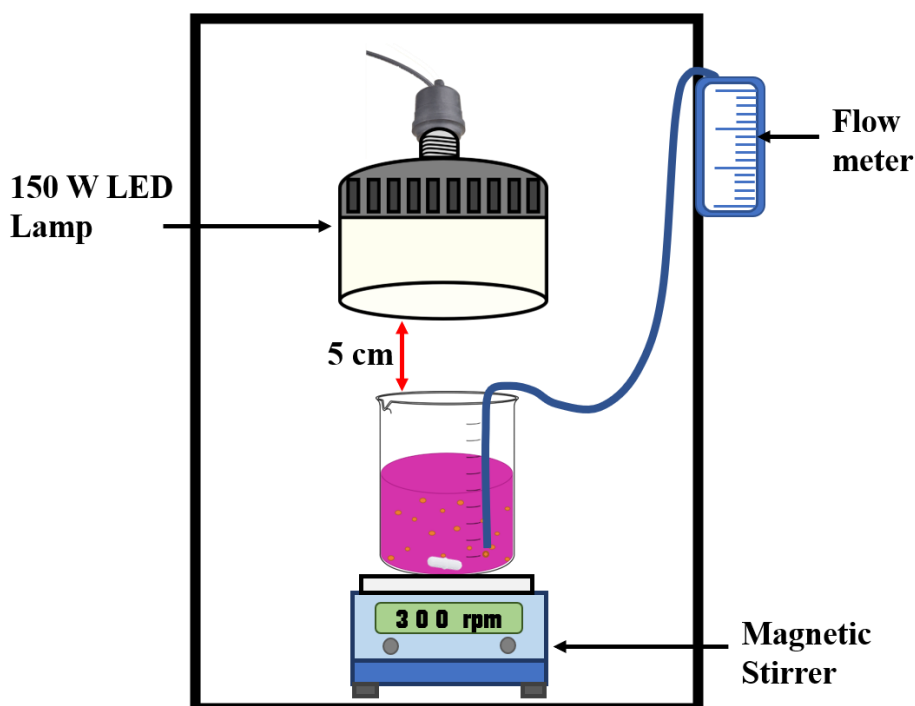


**Figure 3.2: Schematic Diagram of Photocatalytic Degradation System.**

### 3.2.2 UV-Vis Spectrophotometer

The UV-Vis spectrophotometer was used to determine the RhB colour concentration before and after the photocatalytic degradation for 8 hours. The sample solution was

poured into a quartz cuvette with specific light wavelength ( $\lambda$ ) was set in the UV-Vis spectrophotometer for light absorption. When the light penetrates through the sample, some light will be absorbed by the molecules and some will be directly penetrated through. This will reduce the intensity of light that passed through the sample and the degree of absorption by the molecules was recorded by the spectrophotometer. The UV-Vis spectrophotometer can be then used to determine the concentration of pollutants in solution by using the molar absorptivity or plotting a calibration curve (Clark, 2016). The Beer-Lambert Law presents the relationship between the absorbance and the concentration of pollutants as shown in Eq. (3.1) (Oh and Kim, 2021).

$$A = \epsilon lc \quad (3.1)$$

Where  $A$  is the measure of absorbance at specific  $\lambda$ ,  $\epsilon$  is the coefficient of molar absorptivity in  $\text{L mol}^{-1} \text{cm}^{-1}$ ,  $l$  is the length of path that light passed through in cm and  $c$  is the concentration of solution in  $\text{mg L}^{-1}$ .

### 3.3 Analytical Procedures

#### 3.3.1 Chemical Oxygen Demand (COD) Analysis

The COD analysis was conducted to determine the mineralization efficiency of RhB dye and the real printed ink wastewater in the optimize composite photocatalyst. The procedures in examining the COD were according to the *HACH* Reactor Digestion Method 8000 in *HACH* Water Analysis Handbook (HACH, 2019). Generally, 2 mL of sample solution was withdrawn at different time intervals and was injected into COD High Range (HR) Digestion Reagent vials. The COD vials were then digested in a *Hanna HI-839800* reactor at  $150^\circ\text{C}$  for 2H. After the reaction, the vials were allowed to cool at ambient temperature prior to the determination of COD value. The COD value was determined with a *HACH DR890* colorimeter which expressed in  $\text{mg L}^{-1}$ . These steps were duplicated to obtain average results for accuracy data.

### 3.3.2 Biological Oxygen Demand (BOD) Analysis

The BOD represents the amount of oxygen consumed by microorganisms to decompose the organic constituents in water under aerobic condition (Ma, et al., 2020; Sale, et al., 2020). The BOD is the measurement of the difference in dissolved oxygen (DO) in water for certain durations. The BOD<sub>5</sub> was measured according to the standard method of American Public Health Association (APHA) 5210B (APHA, 2018). Generally, the dilution of sample was done based on the desired dilution factor and the sample was poured into a 300 mL BOD bottle. The initial DO value ( $DO_0$ ) was determined using a *EUTECH DO 2700* DO meter. Next, the BOD bottle was sealed with parafilm immediately to avoid additional atmospheric oxygen from dissolving into the solution as this will affect the actual BOD value. The BOD bottle together with the lid were wrapped with aluminium foil to prevent the solution exposure to light. The BOD bottle was then placed in a *VELP SCIENTIFICA FOC 225E* BOD incubator under dark condition at 20°C for 5 days. The final DO value ( $DO_5$ ) was measured after 5 days incubation. The BOD<sub>5</sub> value was calculated using the Eq. (3.1).

$$BOD_5 = DO_0 - DO_5 / \text{Dilution Factor} \quad 3.2$$

Where  $DO_0$  is the initial DO and  $DO_5$  is the final DO value after 5 days incubation which expressed in mg L<sup>-1</sup>.

### 3.3.3 Turbidity Analysis

Turbidity analysis is conducted to measure the suspended biological and chemical particles that present in solution (Farrell, et al., 2018). It is also an important water parameter to indicate clean water quality. The high turbidity in water may be due to high microbial pathogens, clay and silts, hazardous chemicals such as iron and manganese that may affect human health (WHO, 2017). The turbidity of water can be determined according to the instruction manual of *Hanna HI-98703* turbidimeter (Hanna Instruments, 2018). Prior to the turbidity analysis, calibration of the instrument was conducted by using the standard solution given (0.1 NTU, 15 NTU, 100 NTU and

750 NTU). To analyze the turbidity of solution, the sample solution was filled to a sample cell until the marking line. The surface of sample cell was wiped with a cloth to clean the stain that will block the light penetration into the cell. The sample cell was then put into the turbidimeter and the value was read in the unit of Nephelometric Turbidity Unit (NTU). The measurement was repeated to obtain an average value for higher accuracy.

### **3.3.4 pH Analysis**

pH is the expression of the concentration of  $H^+$  ions in water (USEPA, 2021). The pH analysis is an important water quality parameter to determine the acidity or alkalinity of sample solution. At lower pH value, most of the aquatic creatures could not survive. On the other hand, high pH value will also reduce the biodiversity as high alkalinity will damage the organs of organisms (Gensemer, et al., 2017). The solution pH can be determined using a *Hanna HI-2211* pH meter. To analyze the solution pH, the pH probe was cleaned with distilled water before and after every value taken, then it was put into the sample solution to read the value. The pH value was duplicated to obtain an average result for accuracy data.

### **3.3.5 Colour Analysis**

The colour analysis is an important water parameter as it may reflect to the high pollution by coloured salts and dye molecules (Albert, et al., 2021; Iwar, Utsev and Hassan, 2021). The colour can be determined according to *HACH* Platinum-Cobalt Standard Method 8025 in Water Analysis Handbook (HACH, 2014). Based on this method, 50 mL sample solution was first added with a pH 8 buffer powder pillow followed by pH adjustment to pH 7.6 using 1.0 N HCl or 1.0 N NaOH. Next, the sample solution was filtered using a 0.45  $\mu$ m filter. The filtered sample solution was filled into a 10 mL sample cell and the cell was wiped to remove stains on cell. The colour of the sample was read which expressed in Pt-Co.

### 3.4 Preparation of Photocatalyst

In this study, the preparation of  $V_2O_5$ ,  $NiFe_2O_4$ , Delaminated  $Ti_3C_2$  MXene (D- $Ti_3C_2$ ) co-catalyst and D- $Ti_3C_2/NiFe_2O_4/V_2O_5$  composite were systematically synthesized in the subsequent sections.

#### 3.4.1 Synthesis of $V_2O_5$ Photocatalyst

The  $V_2O_5$  photocatalyst was synthesized by a simple thermal decomposition process. The ammonium metavanadate ( $NH_4VO_3$ ) powder was burnt in a muffle furnace at 400 °C for 30 minutes after grounded using mortar and pestle for 1 hour (Zelege et al., 2019; Shafeeq, et al., 2020). A flowchart of the synthesis process is illustrated in Figure 3.3.

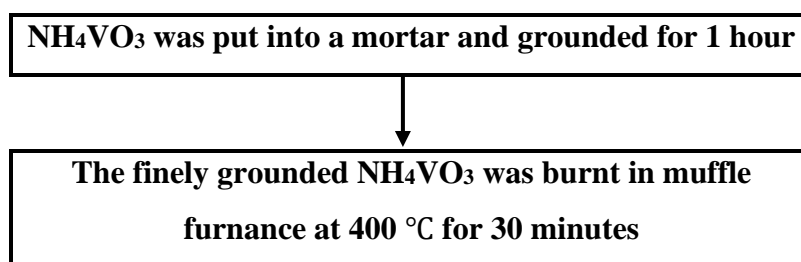


**Figure 3.3: Flowchart of Thermal Decomposition of  $NH_4VO_3$  to Yield  $V_2O_5$ .**

#### 3.4.2 Preparation of $NiFe_2O_4/V_2O_5$ Binary Composite

The  $NiFe_2O_4/V_2O_5$  (NFO/V) composite was synthesized through a simple hydrothermal process (Veisi, et al., 2021; Xie, et al., 2021). In the process, 0.727 g  $Ni(NO_3)_2 \cdot 6H_2O$  and 2.02 g  $Fe(NO_3)_3 \cdot 9H_2O$  were dissolved in 75 mL of DI water. The solution was mixed and stirred for 30 mins. Next, 0.59 g of as-synthesized  $V_2O_5$  was added gradually to the mixture and sonicated for 1H. 2M NaOH solution was added dropwise to the mixture to adjust the pH of solution to 12. The homogeneous solution was transferred to a Teflon-lined autoclave and heated at 180 °C for 12H. After the reaction, the reactor was cooled to room temperature. The precipitate formed was

centrifuged and washed for three times with DI water. Finally, the collected composite was dried at 80 °C for 12 hours. The wt% of NFO to V according to the above procedures was 50 wt% (50-NFO/V). Varying mass of V<sub>2</sub>O<sub>5</sub> were added to obtain series NFO/V composite (10-NFO/V and 20-NFO/V). The pristine NFO was also synthesized for comparison through the same procedures without adding of V<sub>2</sub>O<sub>5</sub>. The preparation process was depicted in Figure 3.4.

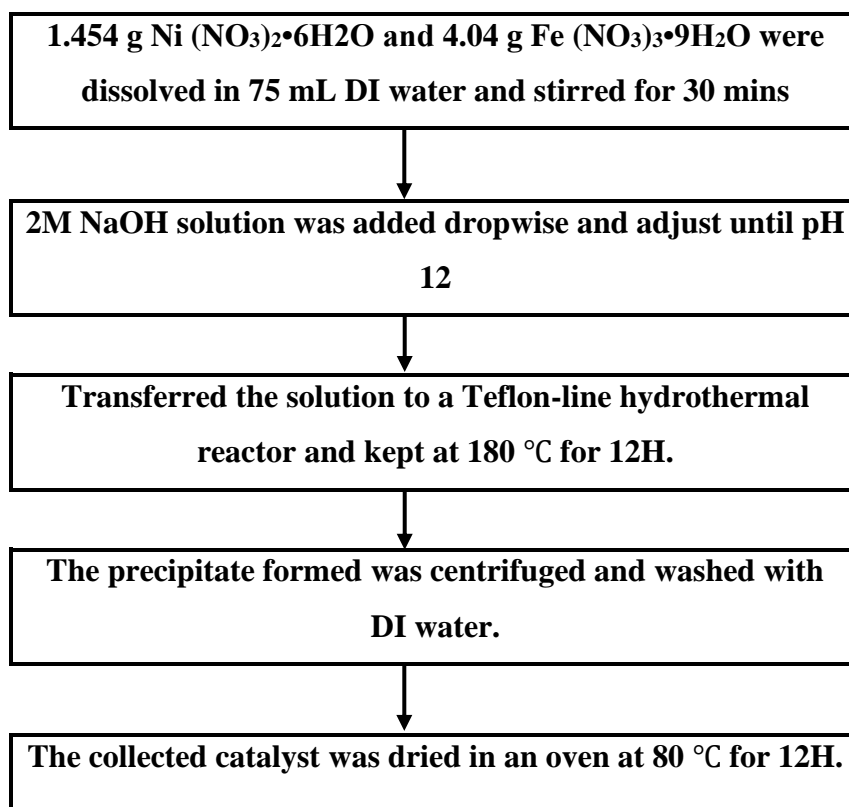


**Figure 3.4: Flowchart of the Preparation of NiFe<sub>2</sub>O<sub>4</sub> Nanoparticles.**

### **3.4.3 Synthesis of Delaminated Ti<sub>3</sub>C<sub>2</sub> MXene Co-catalyst**

Next, the synthesis of 2D Ti<sub>3</sub>C<sub>2</sub> MXene was conducted via a chemical etching using hydrofluoric acid (HF) and stirred for 24 hours at 60 °C (Zhan, et al., 2020). The etched Ti<sub>3</sub>C<sub>2</sub> was let to set for 24 hours before filtered using 0.22 μm nylon filter paper with assisted by vacuum filtration system and washed with nitrogen-purged DI water until the pH of filtrate dropped to the range of pH 6–7. The filtered Ti<sub>3</sub>C<sub>2</sub> was dried under -50 °C of freeze-drying for 8 hours. Subsequently, the dried Ti<sub>3</sub>C<sub>2</sub> was delaminated

using the tetramethylammonium hydroxide (TMAOH) to further increase the interlayer structure of  $\text{Ti}_3\text{C}_2$  (Alhabeib, et al., 2017). The delaminated  $\text{Ti}_3\text{C}_2$  (D- $\text{Ti}_3\text{C}_2$ ) was centrifuged and washed with ultrapure water for 5 times at 7000 rpm for 30 minutes. The process of synthesis was displayed in Figure 3.5.

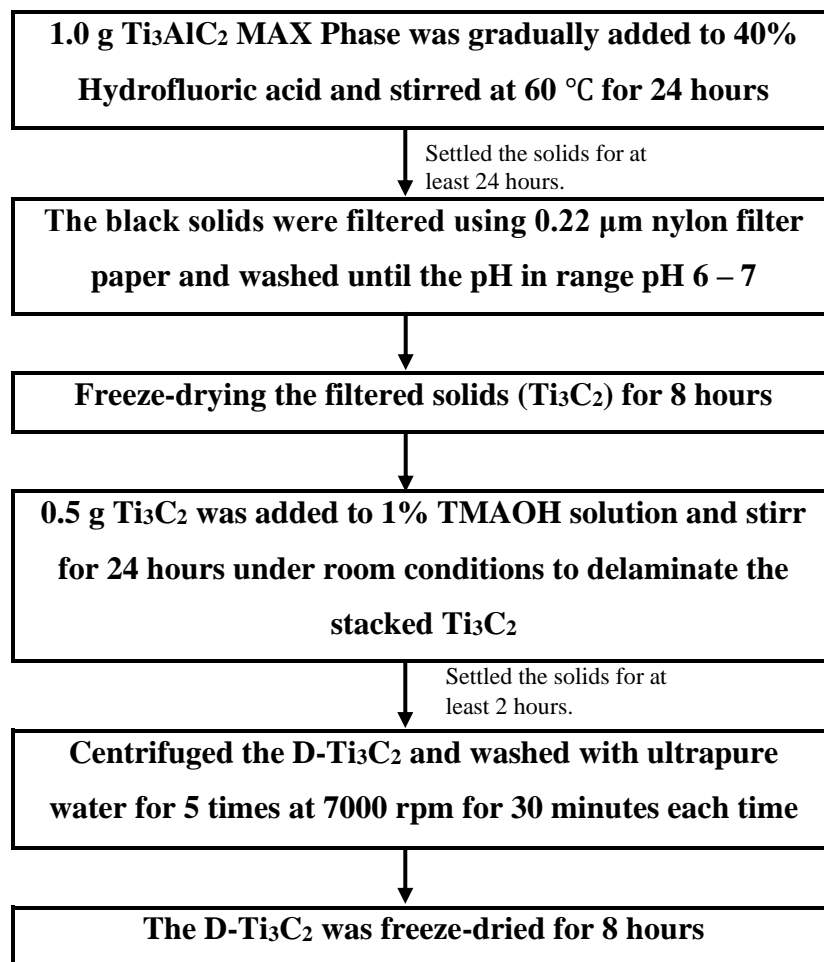


**Figure 3.5: Flowchart of Synthesis 2D  $\text{Ti}_3\text{C}_2$  MXene.**

#### 3.4.4 Preparation of D- $\text{Ti}_3\text{C}_2$ /NiFe<sub>2</sub>O<sub>4</sub>/V<sub>2</sub>O<sub>5</sub> Composite

Lastly, the MV composite was synthesized by dispersing D- $\text{Ti}_3\text{C}_2$  in ethanol under sonication together with adding of  $\text{V}_2\text{O}_5$  for 30 minutes (Zhao, et al., 2018). The ethanol was then evaporated, and the composite was calcined in a tube furnace under nitrogen condition at 300 °C for 1 hour. The flowchart in Figure 3.6 depicted the synthesis process of the composite material.

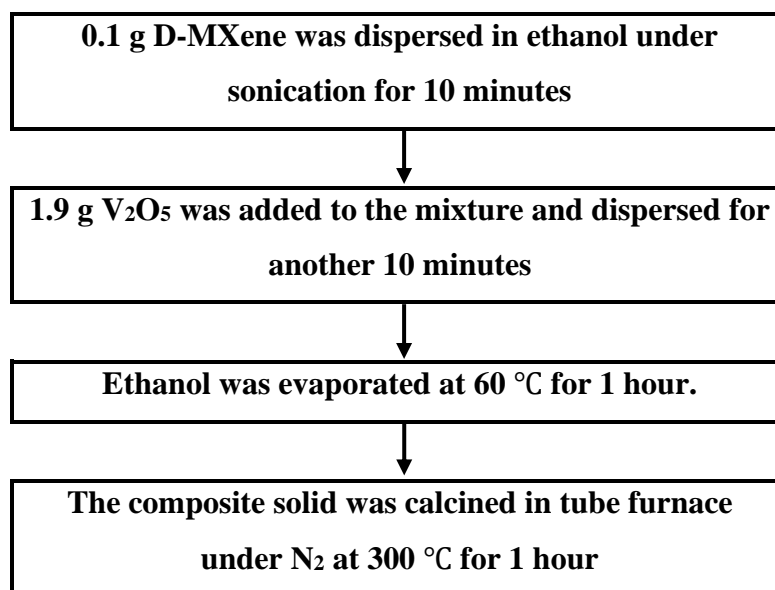


**Figure 3.6: Flowchart of D-Ti<sub>3</sub>C<sub>2</sub>/NiFe<sub>2</sub>O<sub>4</sub>/V<sub>2</sub>O<sub>5</sub> Composite Fabrication.**

### **3.5 Characterization of D-Ti<sub>3</sub>C<sub>2</sub>/NiFe<sub>2</sub>O<sub>4</sub>/V<sub>2</sub>O<sub>5</sub> Composite**

#### **3.5.1 Morphology and Composition Analysis**

The morphology and elemental composition of the as-synthesized D-Ti<sub>3</sub>C<sub>2</sub>/NiFe<sub>2</sub>O<sub>4</sub>/V<sub>2</sub>O<sub>5</sub> composite will be determined through the Field-Emission Scanning Electronic Microscopy with Energy Disperse X-Ray (FESEM-EDX). The analysis was conducted using *Jeol JSM-6701F* FESEM-EDX instrument. Prior to the analysis, the sample was tap on aluminium tube with the carbon tape. The sample photocatalyst was coated with fine layer of platinum through *Jeol JSM-1600* auto fine coater and then vacuumed for 5 minutes for degassing. This morphological and elemental analyse were carried out in at the Faculty of Science in UTAR.

### 3.5.2 Crystallization Analysis

The crystalline properties of the as-synthesized composite can be tested through the a X-ray Diffraction (XRD) analysis. The analysis was done by the *Philips PW1820* diffractometer with Cu K $\alpha$  incident radiation ( $\lambda = 1.5406 \text{ \AA}$ ) within a  $2\theta$  range of  $10^\circ$  to  $80^\circ$ . This crystallization phase analysis was conducted at Faculty of Science in UTAR.

### 3.5.3 UV-Vis Diffuse Reflectance Spectroscopy

The optical properties and the band gap of the as-synthesized catalyst were investigated using the UV-Vis Diffuse Reflectance Spectroscopy (UV-Vis DRS). The UV-Vis DRS spectra were obtained using a *JASCO V-730* UV-Vis spectrophotometer with scanning range of 200 nm to 800 nm. This analysis was tested at Faculty of Engineering and Green Technology in UTAR.

### 3.5.4 Photoelectrochemical Analysis

The photoelectrochemical properties of the as-synthesized photocatalysts were conducted using an Electrochemical Potentiostat (*Gamry Interface 1000*) with a standard three-electrode cell. The setup of the potentiostat was as follows: a bulk cell was filled with 0.5 M Na<sub>2</sub>SO<sub>4</sub> as electrolyte, pure Pt as the counter electrode, Ag/AgCl served as the reference electrode and the fluorine doped tin oxide (FTO) glass coated with photocatalyst as the active electrode. The light source used to initial the reaction was a 150 W LED lamp. Some of the photoelectrochemical tests were conducted, including Transient Photocurrent Response (TPR), Linear Sweep Voltametry (LSV) and Electrochemical Impedance (EIS) Nyquist plot.

### 3.6 Photocatalytic Degradation of Dyestuff

The photocatalytic degradation of RhB dye was conducted for bare  $V_2O_5$ ,  $NiFe_2O_4$ , D- $Ti_3C_2$ , and D- $Ti_3C_2/NiFe_2O_4/V_2O_5$  composites. Initially, 200 mL of 10 mg/L RhB dye was poured into beaker and certain amounts of catalysts were added to each beaker. Before the visible light irradiation, the pollutants with catalyst were underwent the dark reaction for 30 minutes. Then, a 150W LED lamp was switched on and the degradation of dyestuff was determined for 30 minutes interval for total 8 hours reaction time. The samples were centrifuged and the supernatants were tested its concentration using UV-Vis spectrophotometer.

### 3.7 Mineralization Study

The mineralization of RhB dye solution was conducted through a COD analysis. After the LED lamp was switched on for the photocatalytic activities by the D- $Ti_3C_2/NiFe_2O_4/V_2O_5$  composites, the sample solution was extracted every 30 mins. The solution extracted was centrifuged to remove the particles. Then, the mineralization efficiency can be calculated using Eq. (3.3).

$$\text{Mineralization Efficiency (\%)} = [(COD_i - COD_f)/COD_i] \times 100\% \quad \text{Eq. 3.3}$$

Where  $COD_i$  is the initial COD value (mg/L) at  $t = 0$  and  $COD_f$  is the COD value (mg/L) at given time,  $t$  expressed in min.

### 3.8 Parameter Studies

#### 3.8.1 Co-catalyst Loading

Amounts of co-catalyst to be incorporated to semiconductor photocatalyst has great effect to the photocatalytic performance. In this study, the D- $Ti_3C_2$  MXene co-catalyst loading used ranging from 0.25 wt% to 1.0 wt%. The selection of the loading range

was based on the literatures done by Zhuang, Liu and Meng (2019), Liu, et al. (2020a) and Yi, et al. (2020). The experiments were conducted with constant initial RhB dye concentration of 5 mg/L under natural pH 6.9.

### **3.8.2 Catalyst Loading**

The increase in the catalyst loading will increase the photocatalytic degradation efficiency of pollutants (Frindy and Sillanpää, 2020; Hasanpour and Hatami, 2020; Rafique, et al., 2020). The catalyst loading of NiFe<sub>2</sub>O<sub>4</sub> in the binary NiFe<sub>2</sub>O<sub>4</sub>/V<sub>2</sub>O<sub>5</sub> composite was studied at the range from 10 wt% to 50 wt%. The selection of the loading was based on the literatures conducted by Reddy, et al. (2020), Faraji, et al. (2021), Veisi, et al. (2021) and Zhao, et al. (2021). The experiments were conducted under natural pH 6.9 with initial RhB concentration of 5 mg/L.

### **3.8.3 Solution pH**

The pH of the solution has great influence on the photocatalytic degradation of different pollutants. The effect of solution pH on the photocatalytic degradation of dyestuff was studied with ranging from pH 2 to pH 10. The different initial pH of the solution was adjusted using 1.0 M NaOH and 1.0 M HCl. The pH ranges selection was based on the literature carried out by Li, et al. (2018), Chen, et al. (2020) and Singh and Basu (2020). The experiments were conducted at initial RhB concentration of 5 mg/L with optimized NiFe<sub>2</sub>O<sub>4</sub>/V<sub>2</sub>O<sub>5</sub> catalyst loading.

## **3.9 Antimicrobial Activity**

Antimicrobial activities for the pristine V<sub>2</sub>O<sub>5</sub>, NiFe<sub>2</sub>O<sub>4</sub>, D-Ti<sub>3</sub>C<sub>2</sub>, and D-Ti<sub>3</sub>C<sub>2</sub>/NiFe<sub>2</sub>O<sub>4</sub>/V<sub>2</sub>O<sub>5</sub> composites were examined through the inhibition of *S. aureus* and *B. cereus* bacteria. These two bacteria were selected because they are common

type bacteria found in foods, natural water bodies and wastewater effluent. The photocatalytic antibacterial activities were carried out by a spread plate method to observe the viable bacterial cell colonies. Typically, all the glassware and apparatus together with culture medium used in this study were sterilized in an autoclave operated at 120 °C for 20 mins. The kwik-stik was used to culture the bacteria in 50 mL nutrient broth and incubated in orbital shaker at 37 °C for 16H. The bacteria were obtained through centrifugation at 4000 rpm and diluted to  $10^7$  CFU/mL using 85% saline water. The photocatalytic inactivation of bacteria was conducted using the reactor as described in Section 3.2.1. 100 mL of 0.85% saline solution containing bacteria cell with concentration of  $10^7$  CFU/mL was added to the reactor. After that, 0.5 g/L of photocatalyst was loaded and stirred magnetically. The mixture was reacted under dark condition for 30 min before the LED light was switched on. At constant interval times, 2 mL of sample was extracted and filtered using 0.45  $\mu$ m PTFE membrane filter. 0.5 mL of the filtered sample was spread evenly on a nutrient agar plate. The number of viable cells was then observed through photograph after incubated for 24 h at 37 °C. A control experiment was conducted with the LED light irradiation only without the addition of photocatalyst.

### **3.10 The Role of Reactive Oxygen Species (ROS) for Degradation of Dyestuff**

Under the visible light irradiation, the photocatalysis process can generate various ROSs, including  $h^+$ ,  $\bullet$ OH radicals,  $H_2O_2$  and  $O_2\bullet^-$  radicals responsible for the degradation of dyestuff. To investigate the role of ROS in the degradation of dyestuff, the scavenging tests were conducted using common radical scavengers including Catalase, Isopropanol (IPA), Potassium iodide (KI), and Benzoquinone (BQ). 2 mmol of each scavenger was added to reaction solution to scour  $H_2O_2$ ,  $\bullet$ OH,  $h^+$  and  $O_2\bullet^-$ , respectively (Dadigala, et al., 2019; Jaffari, et al., 2019a; Wong, Lam and Sin, 2019).

### 3.11 The Hydroxyl ( $\bullet\text{OH}$ ) Radicals Analysis

According to literature studies, the photogenerated  $h^+$ ,  $\text{H}_2\text{O}_2$  and  $\bullet\text{O}_2^-$  radicals produced in the photocatalytic activity would foster the generation of  $\bullet\text{OH}$  radicals which is the predominant in degrading organic constituents (Jayaraj, et al., 2018; Ali, Nair and Sandya, 2019; Jaffari, et al., 2019b). To further verify the generation of  $\bullet\text{OH}$  radicals over the  $\text{Ti}_3\text{C}_2\text{-V}_2\text{O}_5$  composite in photocatalytic degradation of dyestuff, the terephthalic acid photoluminescence (TA-PL) technique was applied (Wong, Lam and Sin, 2019). The TA was used due to its non-fluorescence property, which could react with  $\bullet\text{OH}$  radicals to be converted into a fluorescent 2-hydroxyterephthalic acid (HTA). Generally, the PL spectra of  $\text{V}_2\text{O}_5$  excited at 315 nm from the TA molecules under light irradiation, while HTA found at the 425 nm peak of the PL intensity indicated that the amount of  $\bullet\text{OH}$  radicals formed on the catalyst (Chai, Lam and Sin, 2019; Shafeeq, et al., 2020).

### 3.12 Recycling Test

To evaluate the stability of D- $\text{Ti}_3\text{C}_2/\text{NiFe}_2\text{O}_4/\text{V}_2\text{O}_5$  composite after photocatalytic reaction, the recycling test was conducted. Generally, the composite was collected after one cycle of photocatalytic process in dyestuff and use for another set of experiment with the same condition (Dadigala, et al., 2019; Zhang et al., 2021). The degradation efficiency was determined. In the typical procedure, the used D- $\text{Ti}_3\text{C}_2/\text{NiFe}_2\text{O}_4/\text{V}_2\text{O}_5$  composite was collected via external magnetic force. The sample collected was then dried in a vacuum oven at 60 °C for overnight. The dried sample was then run for several times to test the durability of the photocatalyst.

### 3.13 Real Printed Ink Wastewater Effluent Study

The photocatalytic degradation of real printed ink wastewater effluent (PIWE) will be conducted using the optimized composite and process parameters. The PIWE was collected at Bercham, Ipoh. After collected from the paper printing industry, the PIWE

was first filtered with 38 µm stainless steel mesh sieve to remove large particles in wastewater. The wastewater was stored in a plastic drum at 5 °C in a refrigerator. Several preliminary studies were also conducted, including COD, BOD, turbidity, pH and colour. The mineralization efficiency of the real PIWE was determined through the COD analysis.

## CHAPTER 4

### RESULTS AND DISCUSSION

This chapter explained the experimental results of the current research. The first part of the chapter presented the characterization studies on the synthesized D-M/NFO/V ternary composite utilized in the photocatalytic degradation of dyestuff. In the second part of this chapter, the preliminary performance of the developed D-M/NFO/V ternary composite in photocatalytic degradation of the synthetic dyestuff wastewater was depicted. In the next part of this chapter, several process parameters including the NFO catalyst loading, D-M co-catalyst loading and the solution pH were studied to evaluate the photocatalytic degradation performance. Subsequently, the antibacterial activities using the optimised D-M/NFO/V ternary photocatalyst towards *Bacillus cereus* (*B. cereus*) and *Pseudomonas aeruginosa* (*P. aeruginosa*) via the zone of inhibition (ZOI) testing. In the fifth part of this chapter, the radical scavenging test was conducted to determine the major reactive oxygen species (ROS) responsive in photodegradation of dyestuff wastewater. This was followed by the reusability study of the optimised ternary photocatalyst. Lastly, the photocatalytic degradation of real printed ink wastewater utilizing the best ternary catalyst at the optimum condition was also studied.

#### 4.1 Characterization of the Synthesized Photocatalysts

Characterization of the synthesized photocatalysts utilized in the photodegradation of dyestuff wastewater such as  $V_2O_5$  (V),  $NiFe_2O_4$  (NFO), Delaminated  $Ti_3C_2$  MXene (D-M), NFO/V binary and D-M/NFO/V ternary composites were conducted. The

characterization techniques used including the surface morphology, elemental composition, crystallization phase, band gap and photoelectrochemical test to evaluate the physiochemical, optical and electronic properties of the photocatalysts. The morphological of the synthesized photocatalysts was examined through FESEM images while the elemental composition analysis was carried out using the EDX technique. The XRD analysis was conducted to determine the crystallization phase of the synthesized photocatalysts. Next, the optical property of the catalysts was identified using the UV-vis DRS technique to obtain the band gap energy of the catalysts. Lastly, the photoelectrochemical tests such as the TPR, LSV, EIS and MS were conducted to study the electronic properties of the catalysts.

#### 4.1.1 Morphological Analysis

Figure 4.1 depicts the morphological structures of the synthesized catalysts including V, NFO, M, D-M, NFO/V binary composite and D-M/NFO/V ternary composite, respectively obtained from the FESEM images. The FESEM image obtained for the  $V_2O_5$  synthesized via the simple thermal decomposition revealed that  $V_2O_5$  have irregular flake-like morphologies. The measured particle diameters of  $V_2O_5$  were varying from 80 nm to 700 nm, while the particle lengths were ranging from 0.18  $\mu\text{m}$  to 1.14  $\mu\text{m}$ . It could be observed that the image of NFO revealed its morphology existed as sphere-like particles with a measured particle diameters ranging from 22 nm to 76 nm.

Figure 4.1 (c) shows the  $Ti_3C_2$  MXene synthesized through the etching of Al from  $Ti_3AlC_2$  MAX phase using hydrofluoric acid (HF) displayed the stack-layered structure which are in consistent to the literatures reported by Ihsanullah (2020), Jeon, et al. (2020) and Dixit, et al. (2022). The delaminated structures of MXene are illustrated in Figure 4.1 (d). The delamination of MXene was conducted via the mixing of MXene in tetramethylammonium hydroxide (TMAOH) assisted with sonication. The morphologies of D-M were less stacked and present to be few layered or single sheets. This could be contributed to the higher active site for the chemical reaction (Hwang, et al., 2020).

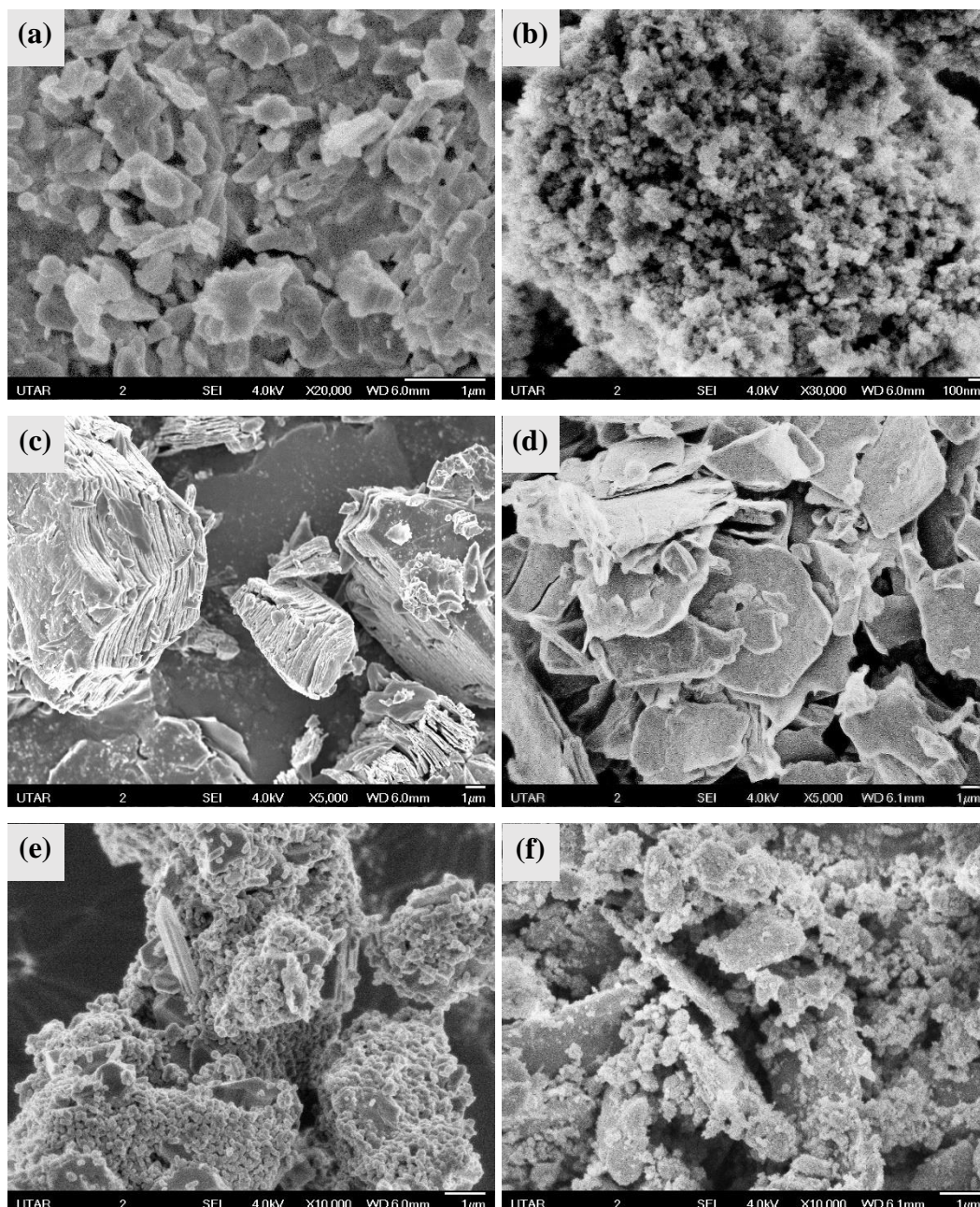


**Figure 4.1: FESEM Images of (a) V, (b) NFO, (c) M, (d) D-M, (e) NFO/V and (f) D-M/NFO/V.**

Based on the FESEM images for the NFO/V binary composite (Figure 4.1 (e)), it can be observed that the irregular shapes of  $V_2O_5$  particles were surrounded with nanosized spherical NFO particles. It was worth noting that the NFO nanoparticles were evenly distributed over the  $V_2O_5$  surfaces forming binary photocatalyst. Lastly, the D-M/NFO/V ternary composite photocatalyst illustrated in Figure 4.1 (f) has the similar morphology as in the NFO/V binary composite with additional of thin sheet

presented in the FESEM images. This indicated that the existence of delaminated MXene in the binary composite forming well-incorporated ternary structure. Nonetheless, the D-M thin sheets are not noticeable in the FESEM images due to its low weight percentage content in the ternary composite. The presence of delaminated  $\text{Ti}_3\text{C}_2$  MXene in the ternary composite can be elucidated by the EDX Mapping as displayed in Figure 4.3.

#### 4.1.2 Elemental Composition Analysis

The analyses of elemental composition of the synthesized photocatalysts were conducted using the Energy Disperse X-ray (EDX) technique. The results obtained for each catalyst, V, NFO, M, D-M, NFO/V and D-M/NFO/V are displayed in Figures 4.2 (a) to (f), respectively. The EDX spectrum of the  $\text{V}_2\text{O}_5$  photocatalyst was composed of V and O elements only, indicating the high purity of the  $\text{V}_2\text{O}_5$  products synthesized through simple thermal decomposition. The results obtained were also in consistent to the EDX spectra reported in literatures (Zelege and Kuo, 2019; Rafique, et al., 2020; Zhang, et al., 2021a). Figure 4.3 (b) displays the EDX spectra of NFO catalyst which mainly composed of Ni, Fe and O elements. Subsequently, the EDX spectrum of the synthesized MXene and Delaminated MXene were depicted in Figures 4.2 (c) and (d). Both obtained results showed that the major chemical compositions are Ti and C elements. The high C peaks existed in the spectra could also be attributed to the carbon tape for holding the sample during the analysis. Figure 4.3 (e) illustrates the EDX spectra of NFO/V binary composite, while Figure 4.3 (f) shows the EDX spectra of D-M/NFO/V ternary composite materials. The results of the EDX analysis for the binary composite contained the elements Ni, Fe, V and O, whereas the ternary composite consisted additional peaks for elements Ti and C. This indicating that the Delaminated  $\text{Ti}_3\text{C}_2$  MXene had successfully incorporated to the NFO/V binary photocatalyst and resulting the ternary composite materials.

The EDX mapping of the synthesized D-M/NFO/V ternary composite material was illustrated in Figure 4.3. The results showed that the existence elements, Ti, C,

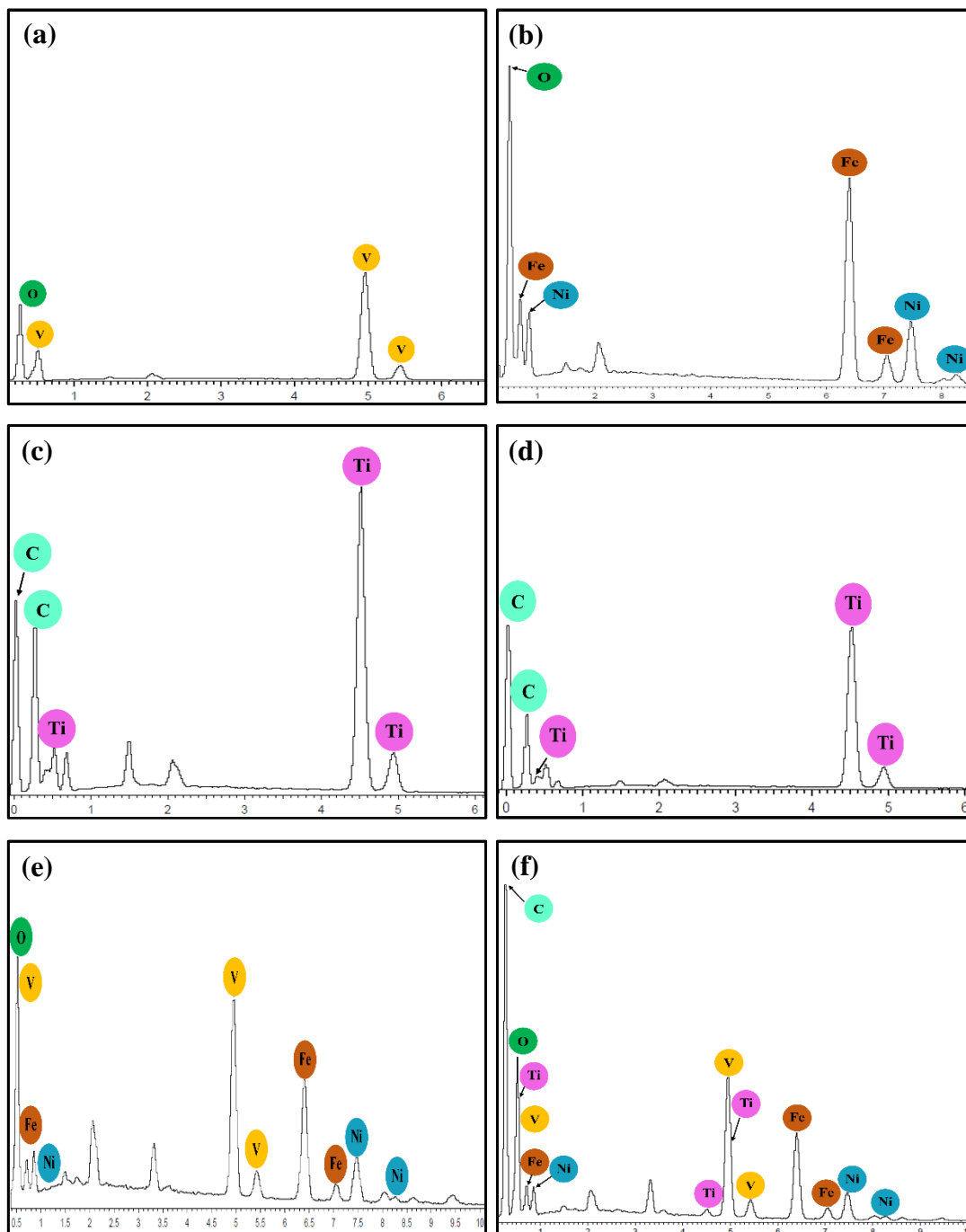


**Figure 4.2: EDX Spectra of (a) V, (b) NFO, (c) M, (d) D-M, (e) NFO/V and (f) D-M/NFO/V.**

Ni, Fe, V and O were distributed evenly in the composite structure. This result further confirmed the XRD finding as above discussion.

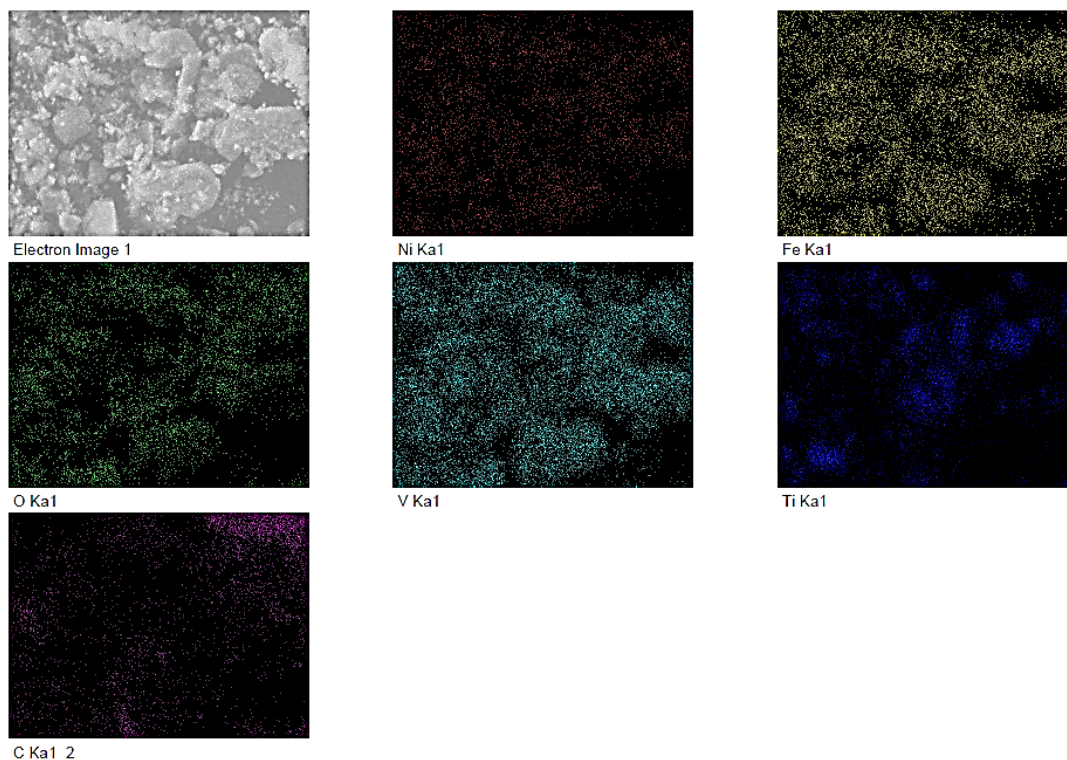


**Figure 4.3: EDX Mapping of D-M/NFO/V Ternary Composite.**

### 4.1.3 Crystallization Phase Analysis

The crystallization phases of the synthesized photocatalysts were characterized through the XRD analyses and the results were depicted in Figure 4.4. As displayed in the figure, the pure  $V_2O_5$  photocatalyst has the characteristic peaks existed at  $2\theta = 15.45^\circ, 20.35^\circ, 21.78^\circ, 26.23^\circ, 31.08^\circ, 32.45^\circ, 34.35^\circ, 41.32^\circ$ , which corresponded to the (200), (001), (101), (110), (400), (011), (310) and (002) crystal planes. These diffraction peaks corresponded to the respective planes confirmed the orthorhombic of the synthesized  $V_2O_5$  crystal structures. The results were consistent with the standard card JCPDS No. 41-426 (Zelege and Kuo, 2019; Karthik, et al., 2020; Rafique, et al., 2020; Shafeeq, et al., 2020; Zhang, et al., 2021a). As for the pure NFO, the diffraction peaks appeared at  $2\theta = 18.44^\circ, 30.34^\circ, 35.73^\circ, 43.42^\circ, 53.88^\circ, 57.42^\circ, 63.05^\circ$ , which matched to the indexes at (111), (220), (311), (400), (422), (511) and (440), respectively. The results reflected that the pure NFO existed as cubic spinel

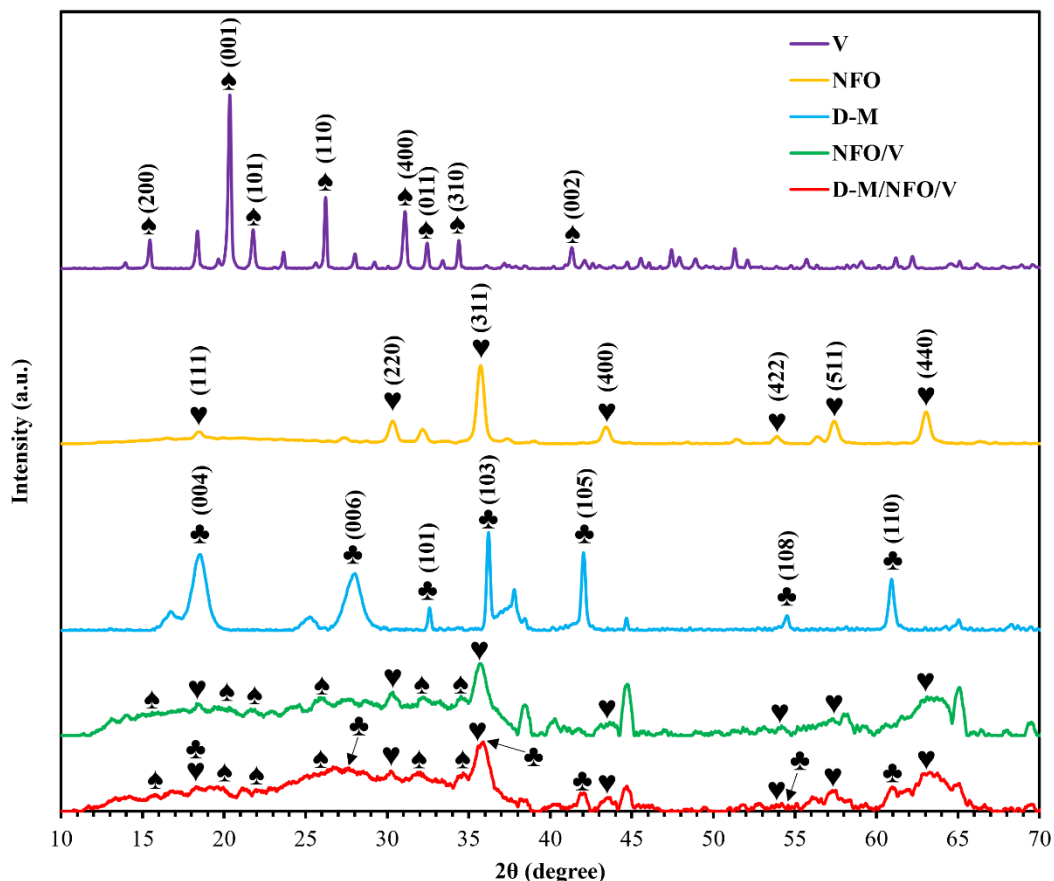


**Figure 4.4: XRD patterns of the Synthesized Photocatalysts.**

structures which referred to the standard JCPDS No. 54-0964 (Reddy, et al., 2020; Baig, et al., 2021; Faraji, et al., 2021; Veisi, et al., 2021).

Moreover, the XRD patterns of the delaminated MXene (D-M) were illustrated in the figure at the angles of  $18.52^\circ$ ,  $28.72^\circ$ ,  $32.51^\circ$ ,  $36.13^\circ$ ,  $41.96^\circ$ ,  $54.42^\circ$ ,  $60.87^\circ$ , which referred to structure planes at (004), (006), (101), (103), (105), (108) and (110), correspondingly. Figure 4.5 demonstrates the XRD patterns for the MAX phase, MXene and delaminated MXene (D-M) for comparison. All the D-M and MXene structures having the similar diffraction peaks which in consistent to the  $\text{Ti}_3\text{AlC}_2$  MAX phase with standard JCPDS No. 52-0875 (Fang, Cao and Chen, 2019; Huang, et al., 2020; Rasheed, et al., 2021). Notably, the strong (104) peaks of the MAX phase at the diffraction angle of  $39^\circ$  was disappeared in both D-M and MXene. This was attributed to the etching of Al element during the HF treating (Yan, et al., 2019; Yang, et al., 2019; Li, et al., 2021a).

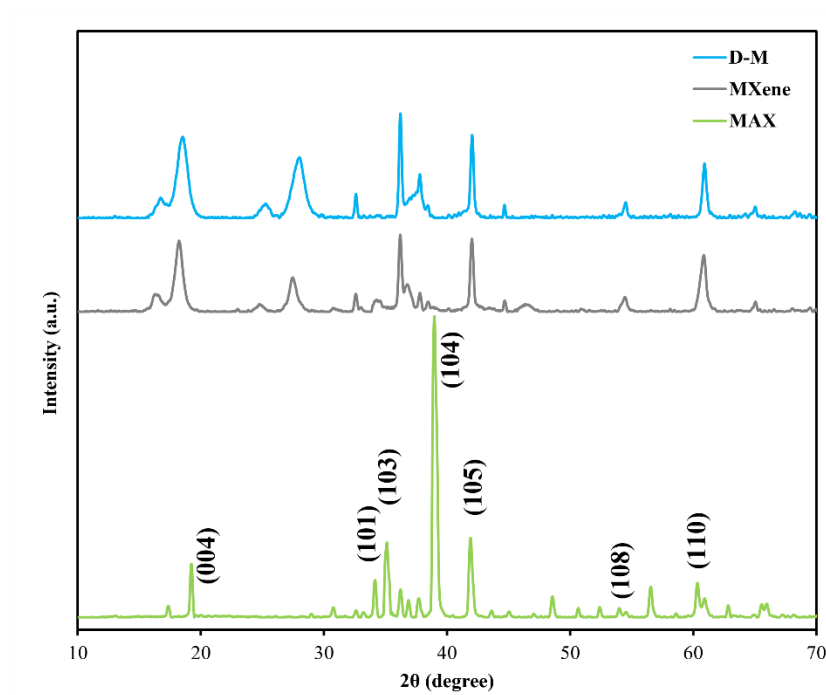


**Figure 4.5: XRD patterns of MAX, MXene and D-M.**

On the other hands, the XRD patterns for the NFO/V binary and D-M/NFO/V ternary composite materials depicted the characteristic peaks for each component, indicating the well-synthesized composite photocatalysts. Figure 4.6 displays the magnified (004) plane for the ternary composite. The peak at  $18.52^\circ$  confirmed the presence of D-M in the ternary photocatalyst.

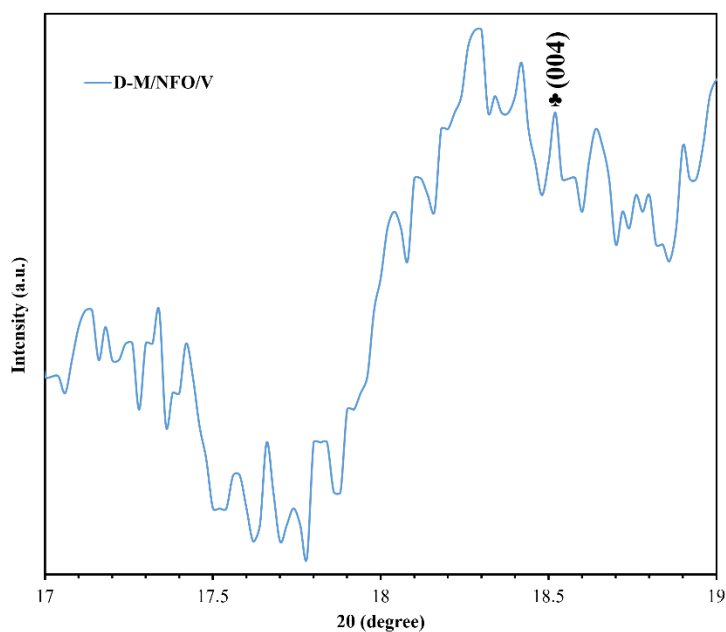


**Figure 4.6: Magnified image indicating the presence of D-M in ternary composite.**

#### 4.1.4 Band Gap Energy Analysis

The optical properties of the synthesized photocatalysts including V, NFO, NFO/V and D-M/NFO/V were determined via the UV-vis Diffuse Reflectance Spectroscopy (DRS) analysis. In Figure 4.7, the UV-vis DRS spectra of the synthesized catalysts presented that the characteristic light absorption edges for V, NFO, NFO/V and D-M/NFO/V were 380 nm, 530 nm, 470 nm and 490 nm, respectively. The results indicated that all the synthesized photocatalysts exhibited visible light absorption capacity. As observed from the figure, the NFO/V binary composite had shifted from 380 nm to 470 nm as compared to pure  $V_2O_5$ . This can be attributed to the interaction between NFO and V forming the heterojunction (Chen, et al., 2021; Zhang, et al., 2021a). On the other hand, the D-M/NFO/V ternary composite revealed longer visible light absorption edges at 490 nm as compared to bare  $V_2O_5$  (380 nm) and NFO/V (470 nm) binary composite. The black colour delaminated MXene incorporated in the composite structure has improved the light absorption and photon harvesting capability (Yan, et al., 2019; Zhuang, Liu and Meng, 2019). This property can be improved the photocatalytic activities in degrading the pollutants which will be further discussed in Section 4.3.

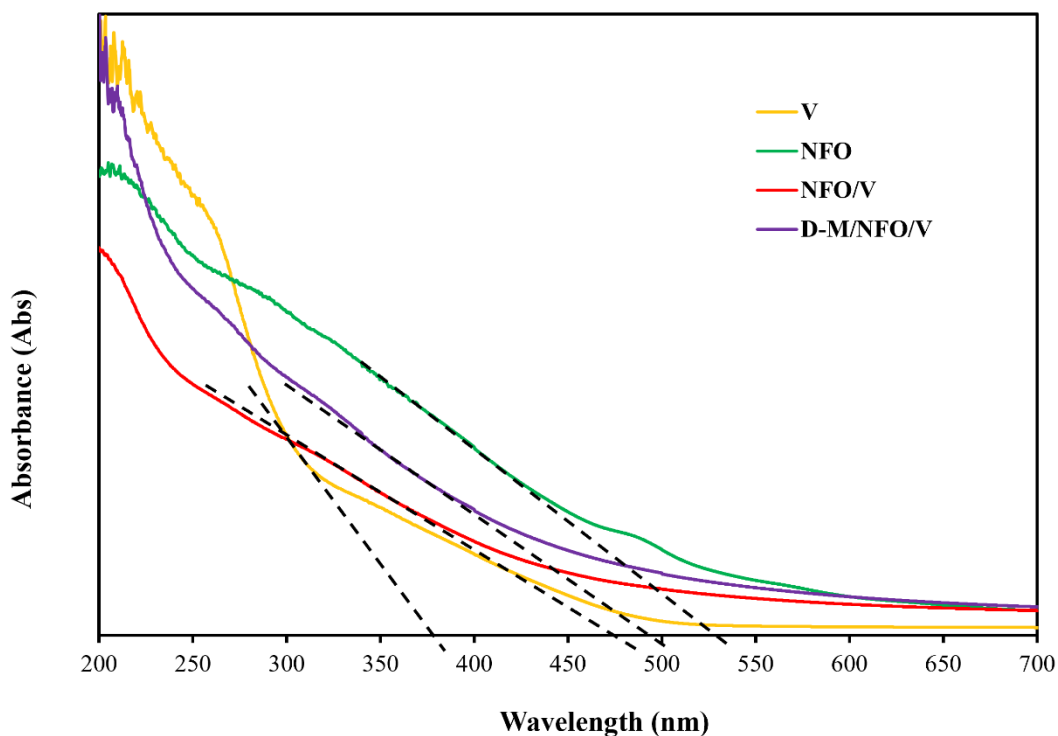


**Figure 4.7: UV-vis DRS Spectra of the Synthesized Photocatalysts.**

The optical band gap ( $E_g$ ) of the semiconductor is estimated through the Tauc's method expression as displayed in Eq. (4.1) to relate the optical absorption edge of photocatalyst to the energy gap (Fang, Cao and Chen, 2019; Tan, et al., 2019; Zhang, et al., 2021d; Zhao, et al., 2021).

$$(\alpha h\nu)^{1/n} = A(h\nu - E_g) \quad (4.1)$$

Where  $\alpha$ ,  $h$ ,  $\nu$ ,  $A$  and  $E_g$  denote the light absorption coefficient, Planck's constant ( $4.136 \times 10^{-15} \text{ eV Hz}^{-1}$ ), frequency of light (Hz), proportional constant and band gap energy (eV), respectively. The value of  $n$  in the expression indicating the direct ( $n=0.5$ ) or indirect ( $n=2$ ) transition band gap of the materials.

Furthermore, the band gap energies of the synthesized photocatalysts were calculated by the extrapolating of  $(F(R)h\nu)^2$  versus the photon energy ( $h\nu$ ) expressed in eV through the Kubelka-Munk function as depicted in Eq. (4.2) and the photon energy is given by the equation in Eq. (4.3) (Li and Wu, 2015; Makula, Pacia and Macyk, 2018; Tan, et al., 2019).

$$F(R) = \frac{(1-R)^2}{2R} \quad (4.2)$$

$$E_g = \frac{hc}{\lambda} \quad (4.3)$$

Where  $F(R)$  is the Kubelka-Munk function,  $R$  is the reflectance (%) of the material,  $E_g$  is the band gap energy (eV),  $c$  is the velocity of light travel in vacuum ( $3.0 \times 10^8 \text{ m s}^{-1}$ ) and  $\lambda$  denotes as the wavelength (nm) of light absorption.

The linear expression of the  $(F(R)h\nu)^2$  versus  $h\nu$  for determining band gap energies for each photocatalyst was plotted and depicted in Figure 4.8. From the figure, a tangent line was drawn to obtain the optical band gap energy. The attained band gap energies for V, NFO, NFO/V and D-M/NFO/V were 2.78 eV, 2.00 eV, 2.63 eV and 2.45 eV, correspondingly. The moderately wide band gap of  $\text{V}_2\text{O}_5$  was constricted with the addition of NFO forming narrower band gap of NFO/V binary composite materials. The results are well-aligned with the literature reports (Borrás, et al., 2020; Reddy, et al., 2020; Paul and Dhar, 2020; Chen, et al., 2021). In the literatures, the addition of

narrow band gap material to that of wide band could reduce the band gap energy with enhanced visible light absorption for the improved photocatalytic activities. Moreover, the addition of D-M as a co-catalyst could further improve the light absorption capacity with diminished band gap energy. Similar findings were reported in other literatures (Fang, Cao and Chen, 2019; Shen, et al., 2019; Rasheed, et al., 2021).

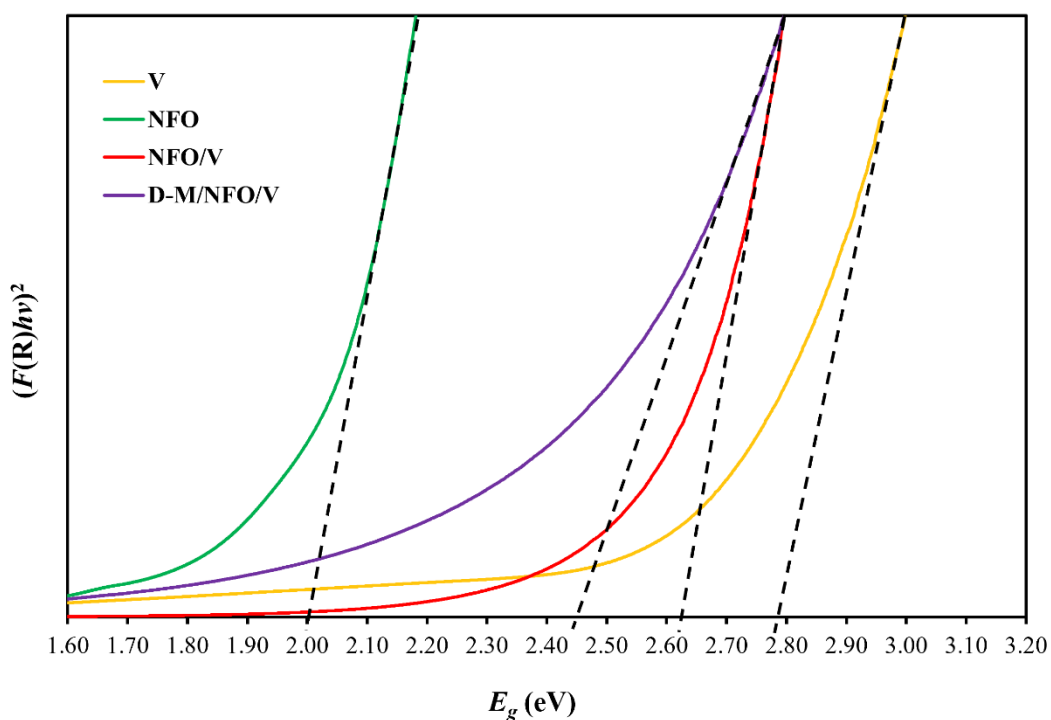


**Figure 4.8: Kubelka-Munk Function Plot of  $(F(R)hv)^2$  versus  $hv$  of V, NFO, NFO/V and D-M/NFO/V photocatalysts.**

#### 4.1.5 Photoelectrochemical Test

Figures 4.9 (a) and (b) show the Transient Photocurrent Response (TPR) and Electrochemical Impedance Spectroscopy (EIS) for the synthesized photocatalysts. The TPR measurement was used to investigate the charge carrier separation efficiency while the EIS was to further validate the photoinduced charge carrier transmission (Zeng, et al., 2016; Xia, et al., 2018; Veisi, et al., 2021). As depicted in Figure 4.9 (a), the photocurrent responses increased in all the samples instantly when the LED light is switched on and dropped immediately when the light was turned off. The results indicated all the photocatalysts were responded to the LED light illumination.

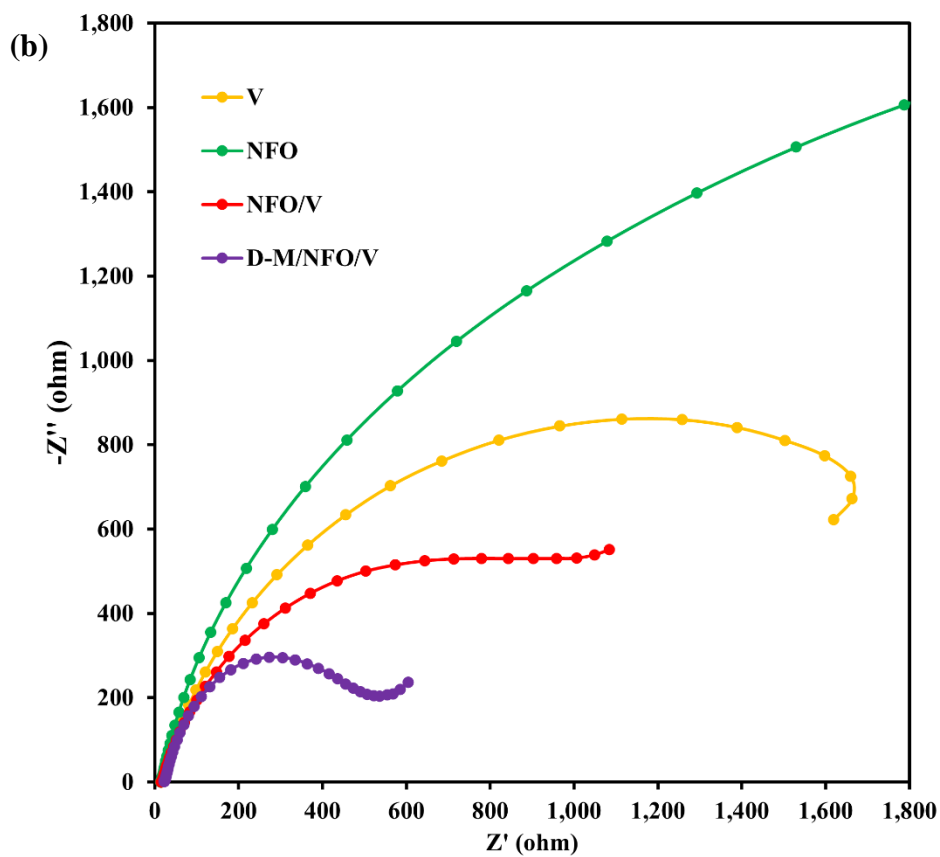
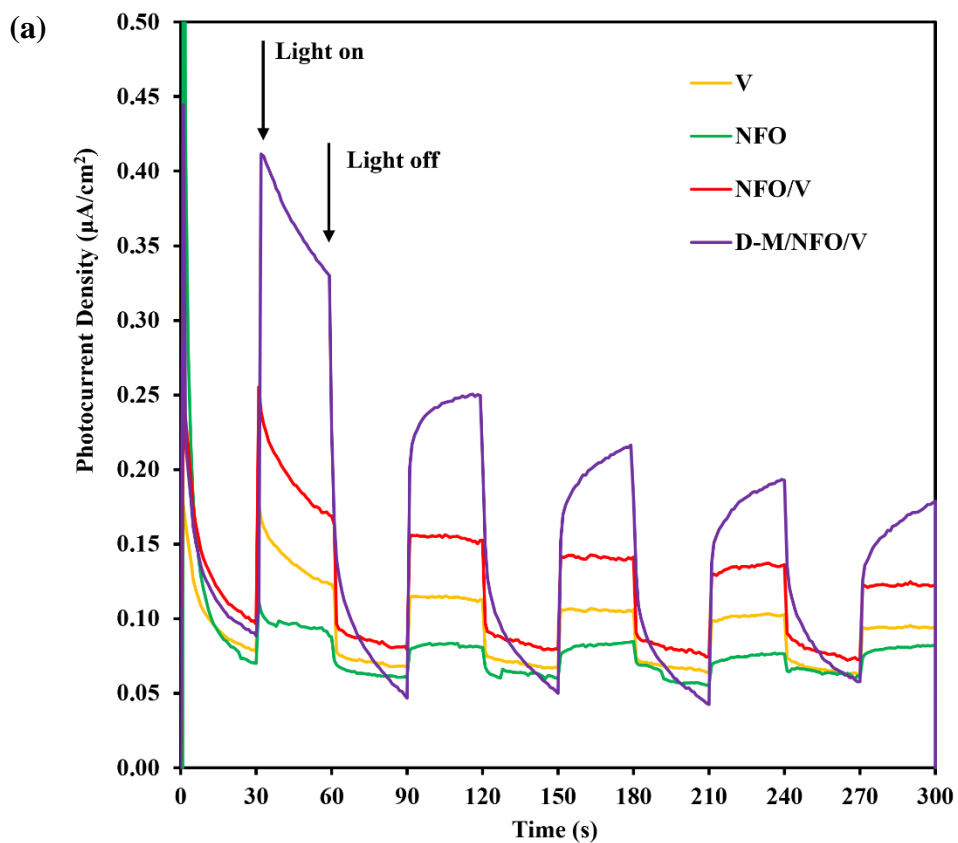


Figure 4.9: (a) TPR and (b) EIS Nyquist Plot of the Synthesized Photocatalyst.

The photocurrent generated by pure NFO and pure V single photocatalyst were low, indicating poor charge carrier separation of individual catalysts component. The binary NFO/V had improved photocurrent response due to the formation of heterojunction between the pure V and pure NFO (Raizada, et al., 2021; Sin, et al., 2021; Xie, et al., 2021). When the D-M was incorporated with NFO/V binary catalyst, the photoexcited  $e_{cb}^-$  migrated from the binary composite to the large surface D-M. The D-M was expected to work as the co-catalyst and formed the Schottky barriers with the binary NFO/V catalysts, inhibiting the possible recombination of  $e_{cb}^- - h_{vb}^+$  pairs in the binary structure (Li, et al., 2021a; Zhong, Li and Zhang, 2021). Consequently, the ternary D-M/NFO/V could exhibit better photocatalytic activities as compared to binary and unary catalysts.

Furthermore, the EIS Nyquist curves depicted in Figure 4.9 (b) also revealed that the enhanced charge separation and migration of charge carriers was obtained for the ternary D-M/NFO/V photocatalyst. Larger semicircle arcs were observed for both pure NFO and pure V unary catalysts. The results indicated poor charge separation efficiency and higher recombination rate of  $e_{cb}^- - h_{vb}^+$  pairs which exhibited poorer photocatalytic activities. The order of the reduction in semicircle arc size was as followed: NFO > V > NFO/V > D-M/NFO/V. Among the samples, the smallest semicircle arc observed in the ternary compound implied that the minor interfacial charge-transfer resistance and hold strong ability in shunting  $e_{cb}^- - h_{vb}^+$  pairs for the photoreaction (Zeng, et al., 2016; Vattikuti, Nam and Shim, 2018; Zhang, et al., 2021c). This EIS Nyquist outcomes were consistent with the TPR result.

To determine the band position of the synthesized photocatalysts, the Mott-Schottky (MS) analysis was conducted and illustrated in Figure 4.10. The conductive band potential ( $E_{cb}$ ) of the bare V can be determined by drawing a tangent line to the  $x$ -axes of the graph (Figure 4.10 (a)). The  $E_{cb}$  of the V was evaluated to be + 0.46 eV. The positive slope in this plot, indicating that V is a  $n$ -type semiconductor. Meanwhile, the negative slope was obtained for pure NFO as shown in Figure 4.10 (b), revealing that it is a  $p$ -type photocatalyst. The measured  $E_{cb}$  for pure NFO was -0.79 eV. By integrating the UV-vis DRS and the MS analyses, the valence band ( $E_{vb}$ ) of the semiconductor can be calculated by the formula in Eq. (4.4) (Atacan, Güy and Özacar, 2021; Duan, et al., 2021; Feizpoor, et al., 2021).

$$E_{cb} = E_{vb} - E_g \quad (4.4)$$

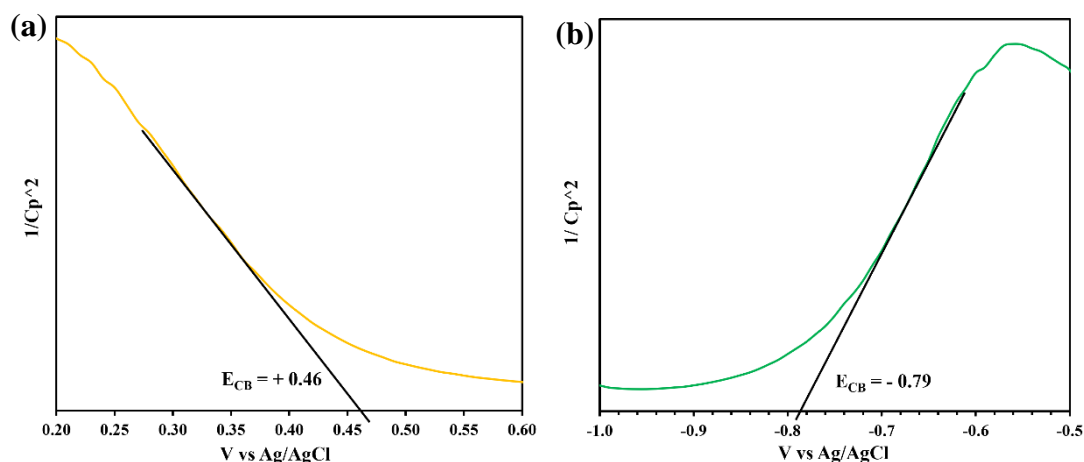


**Figure 4.10: Mott-Schottky Plot for (a) Pure V and (b) Pure NFO.**

Therefore, the  $E_{vb}$  of each photocatalyst was calculated and illustrated in Table 4.1.

**Table 4.1: The Potential Band of the Synthesized Photocatalysts.**

Photocatalyst	$E_g$	$E_{cb}$	$E_{vb}$
V	2.78 eV	+0.46 eV	+3.24 eV
NFO	2.00 eV	-0.79 eV	+1.21 eV

## 4.2 Preliminary Study of Photocatalytic Degradation of RhB Dye

In the preliminary study, the RhB dye was treated to evaluate its dye removal efficiency under the photolysis and photocatalysis. Under the photolysis, the RhB dye was treated solely under LED light irradiation without adding any photocatalyst. Meanwhile, under the photocatalysis, 0.5 g/L of D-M/NFO/V photocatalyst was added to the treatment system to compare the dye removal efficiency with and without the presence of catalyst. Figure 4.11 shows the photolysis process with little dye removal efficiency of 15.5 % in 360 min under LED light irradiation. On the contrary, when D-M/NFO/V photocatalyst was added to the RhB dye reactor at the same condition as in the photolysis, a remarkably high decolorization efficiency was obtained at 90.2 %.

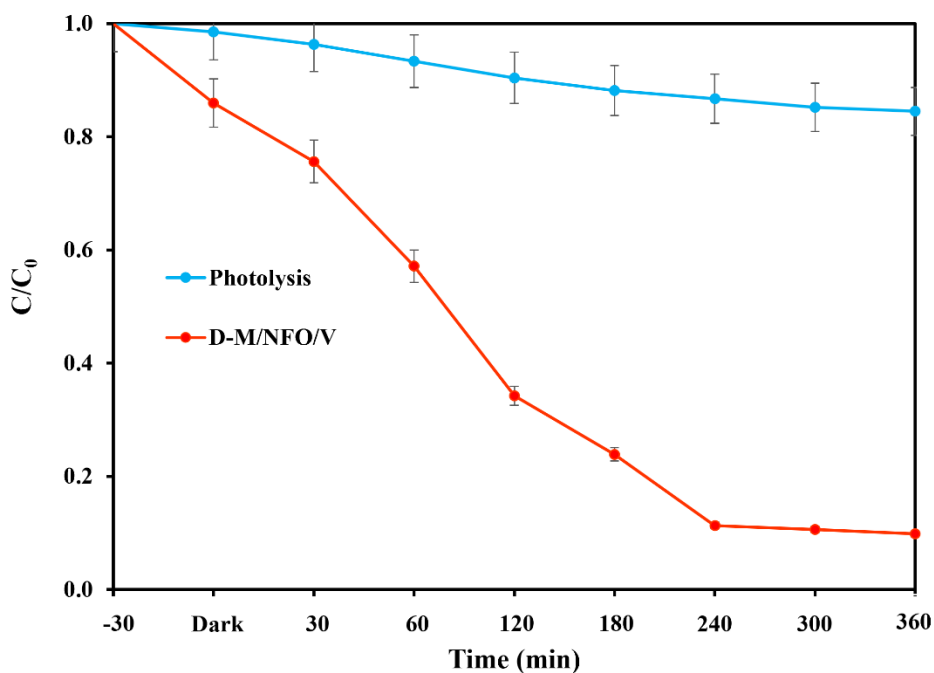


**Figure 4.11: RhB Dye Removal Efficiency under Photolysis and Photocatalysis ([RhB Dye] = 5 mg/L; [Catalyst] = 0.5 g/L; Solution pH = 12.0).**

The outstanding decolorization efficiency was obtained under the photocatalytic degradation of RhB dye. Under the light illumination, the D-M/NFO/V ternary compound with band gap energy of 2.45 eV was activated by accepting the photon energy from the LED light source. The  $e_{cb}^- - h_{vb}^+$  pairs were generated with higher TPR and notably small EIS value indicating excellent charge separation efficiency that could be contributed to the generation of ROS (Sajid, et al., 2020; Zhao, et al., 2021). The photoactivated  $h_{vb}^+$  at the valence band will react with the hydroxide ions generated from the dissociation of water molecules in the aqueous solution. Thereby, producing the highly oxidative  $\bullet\text{OH}$  radicals with redox potential of 2.8 eV which effectively degrade dye molecules to produce  $\text{CO}_2$ ,  $\text{H}_2\text{O}$  and degraded products (Vattikuti, et al., 2018; Mishra, et al., 2020; Shen, et al., 2021).

In the present study, the quality parameters studies of RhB dye wastewater such as COD, colour, turbidity and solution pH were also conducted using the D-M/NFO/V ternary composite under the LED light irradiation. Table 4.2 displays the parameters of RhB dye before and after the photocatalytic degradation by the ternary composite. As depicted in the table below, the initial COD of RhB dye was 80 mg/L and the COD

value of the wastewater after 6 hours photocatalytic treatment was 41 mg/L, which corresponding to the COD removal efficiency of 48.75 %. Furthermore, the turbidity reduction and the true colour removal efficiency were 66.47 % and 62.78 %, respectively. As for the solution pH, a decrease of solution pH from pH 12.01 to 9.34 was observed after the photocatalysis. The decrease in the solution pH could be ascribed as the OH<sup>-</sup> ions in the solution reacted with the photoinduced  $h_{\nu b}^+$  to generate •OH radicals, which responsible in degrading the dye molecules (Weldegebrerial and Sibhatu, 2021).

**Table 4.2: Parameters of the RhB dye before and after Photocatalytic Degradation using D-M/NFO/V Ternary Composite.**

Parameters	Unit	Before Treatment	After Treatment	Efficiency (%)
COD	mg/L	80.0	41.0	48.75
Colour	Pt-co	90.8	33.8	62.78
Turbidity	NTU	24.1	8.1	64.47
pH	-	12.01	9.34	-

In addition, the UV-Vis adsorption spectrum of the RhB dye solution at the wavelength ( $\lambda$ ) of 553 nm against the different time intervals was depicted in Figure 4.12. The results showed that the RhB dye absorbance decreased with time when treated with D-M/NFO/V ternary photocatalyst for 360 mins.

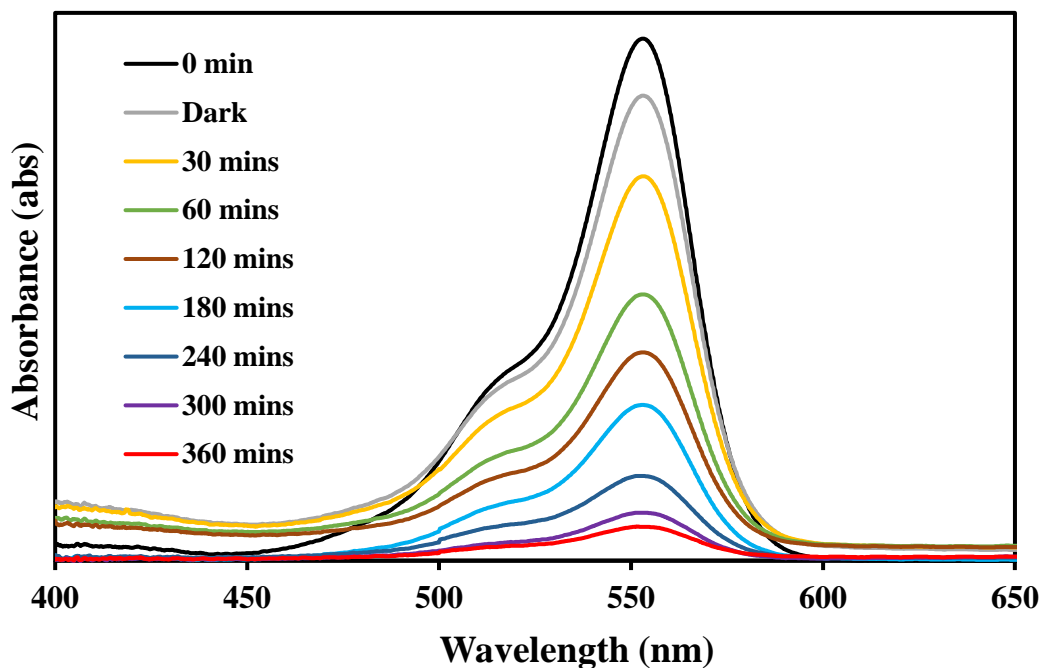


**Figure 4.12: UV-vis Absorption Spectrum of RhB at  $\lambda = 553$  nm Against Time.**

### **4.3 Effect of Process Parameter Studies on Photocatalytic Degradation of Dyestuff**

The effect of process parameter studies was evaluated to optimise the photocatalytic degradation of dyestuff wastewater using the synthesized D-M/NFO/V ternary composite materials. The operational parameters to be studied including the NFO loading in NFO/V binary compound, the D-M co-catalyst loading in D-M/NFO/V ternary system and dye solution pH.

#### **4.3.1 Effect of NFO Catalyst Loading in NFO/V Binary Composite**

In the binary composite materials, the appropriate ratio of NFO weight percentage (%wt) on the V catalyst loading was highly affected the photocatalytic activities. In the present study, the NFO weight loading was ranging from 10 wt%, 20 wt%, 50 wt% and 70%, which denoted as 10NFO/V, 20NFO/V, 50NFO/V and 70NFO/V,

accordingly. The experiments were carried out in the same conditions of 0.5 g/L catalyst loading, RhB concentration at 5 mg/L and solution pH of 12.0. Figure 4.13 displays the photocatalytic degradation efficiency of the RhB dye solution using bulk V, bare NFO, and different %wt NFO to V under the LED light irradiation for 240 min. The photocatalytic degradation of dye for pure V and pure NFO were 31.8% and 43.3%, respectively. When the pure NFO was added onto the V catalyst, the photocatalytic degradation efficacy exhibited significant enhancement. The removal efficiency was increased from 44.4% to 73.9% when increasing NFO loading from 10 wt% to 50 wt%. However, further increase in the NFO loading, the removal efficiency of binary composite was reduced to 49.0%.

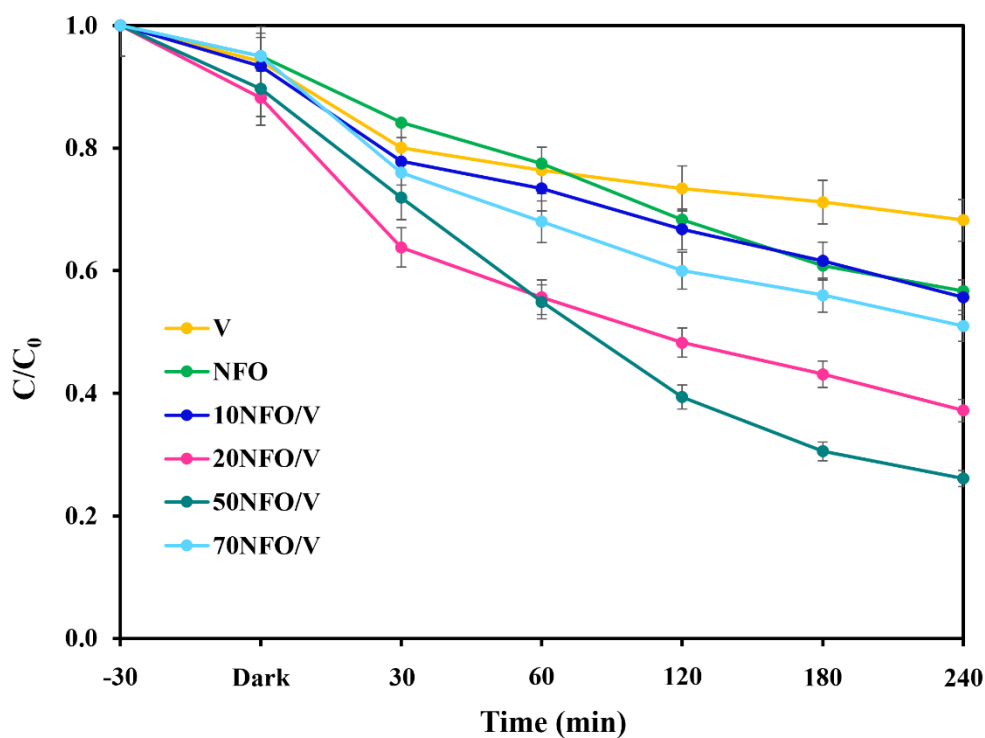


**Figure 4.13: Photocatalytic Activity of Pure V, Pure NFO and NFO/V with various NFO loadings toward the Degradation of RhB Dye ([RhB] = 5 mg/L; [Catalyst] = 0.5 g/L; Solution pH = 12).**

The NFO/V binary composite displayed remarkable removal efficiency as compared to the single photocatalyst. This can be ascribed to the enhancement of the  $e_{cb}^- - h_{vb}^+$  pairs separation of Z-scheme heterojunction composite, promoting the charge separation between the two materials (Hong, et al., 2016; Jayaraman, et al., 2019; Fan, et al., 2021; Liu, et al., 2021b). Furthermore, the increase in the NFO dosage

in NFO/V binary compound boosted the photocatalytic activities as the synergetic effect of the heterostructure enhanced the charge separation which prolonged the redox activities. Nevertheless, the surplus quantities of NFO inhibited the photocatalysis process. This could be attributed to the excess amount of NFO obstructed the light absorption which weakened the generation rate of  $e_{cb}^- - h_{vb}^+$  pairs (Dadigala, et al., 2019; Cao, et al., 2021). Additionally, the overdosage of NFO can conceal the surface of the active sites which resulted in the shielding effect that hindered the charge carrier production and declined the photocatalytic performance (Mishra, et al., 2020; Huang, et al., 2021).

Similar findings were reported by Liu, et al. (2021b) when increasing in the amount of  $\text{Bi}_2\text{S}_3$  catalyst in  $\text{Bi}_2\text{S}_3/\text{BiVO}_4/\text{TiO}_2$  nanorods (BVT) ternary composite from 3 mol to 4 mol, the photodegradation of methyl orange enhanced from 62% to 76% under 300W Xenon lamp for 180 min. When further increase the dosage of  $\text{Bi}_2\text{S}_3$  catalyst to 5 mol, the degradation efficiency reduced to 69%. The results revealed that the excess amount of  $\text{Bi}_2\text{S}_3$  had hindered the light absorption can be inhibited the separation of  $e_{cb}^- - h_{vb}^+$  pairs. On the other hand, Chachvalvutikul and colleagues (2021) studied the effect of  $\text{FeVO}_4$  (FV) catalyst dosage in ternary compounds. In their study, the addition of the FV contents from 0.5 wt% to 1 wt%, the photocatalytic degradation efficiency improved from 93.2% to 99.3%. A deterioration in the degradation efficacy of 80.8% was observed as FV content increased to 3 wt% in the ternary composites. The findings were indicated that the suppress of the recombination rate of the charge carrier as well as the reduction of catalyst reactive sites due to the shielding effect by the excessive FV contents.

#### **4.3.2 Effect of D-M Co-catalyst Loading in D-M/NFO/V Ternary Composite**

To further enhanced the Z-scheme heterojunction of NFO/V, the D-M with different loadings were evaluated toward the degradation of RhB dye. The D-M loading was varied from 0.25 wt% to 1.0 wt%. Figure 4.14 demonstrates the photoactivities of D-M/NFO/V ternary composite with different D-M loadings. Addition of D-M loadings from 0.25 wt% to 0.5 wt% enhanced the photocatalytic degradation efficiency

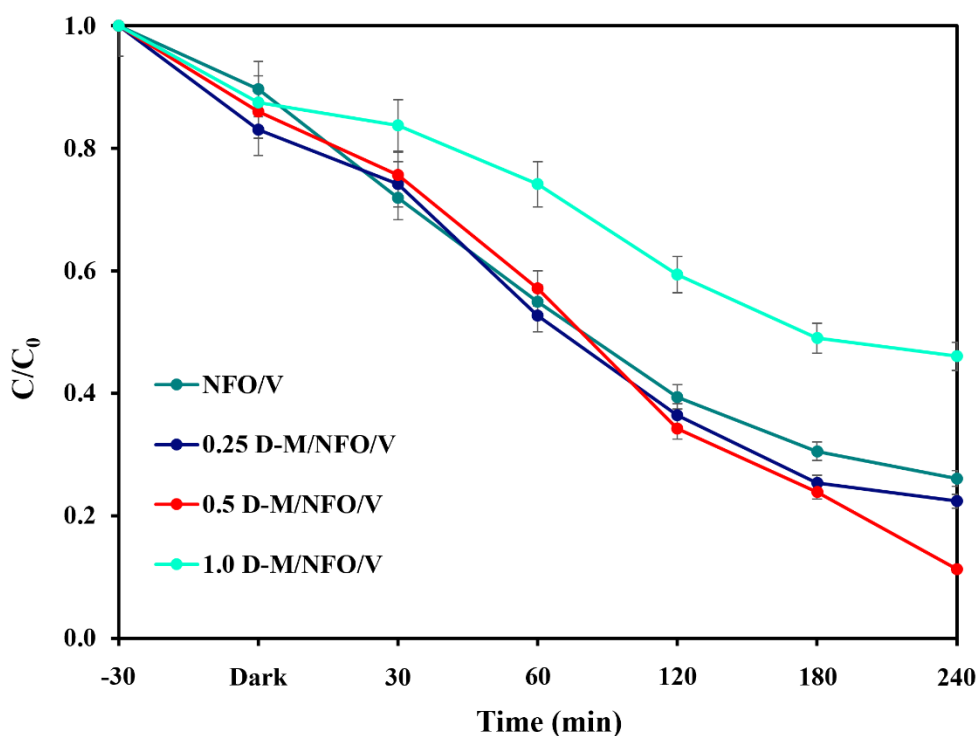


**Figure 4.14: Photocatalytic Activity D-M/NFO/V Ternary Compound at Different D-M loadings toward Degradation of RhB Dye ([RhB] = 5 mg/L; [Catalyst] = 0.5 g/L; Solution pH = 12).**

drastically to 77.6% and 88.7%, respectively. Nonetheless, the further merged of D-M content was significantly deteriorated the removal efficiency to 54.0%. In comparison to the photocatalytic degradation of RhB with binary NFO/V (73.9%), the 1.0 wt% D-M/NFO/V exhibited the best degradation efficiency of 88.7%.

Incorporation of D-M can work as a co-catalyst to further enhance the transmission of the photoinduced charge carriers in the ternary composite materials. Appropriate amount of co-catalyst loadings can be dramatically enhanced the photocatalytic performance. This can be ascribed as the integration of D-M co-catalyst can broaden the light absorption range, the highly conductive metallic D-M promote fast migration of photogenerated  $e_{cb}^-$  from the binary NFO/V to large surface area of D-M and the contact interfaces providing more active sites for reactions (Yang, et al., 2019; Liu, et al., 2020b; Wu, et al., 2021). As the loadings of D-M were added excessively, the degradation efficiency of ternary composite dropped. The results can be attributed to the higher amount of black colour D-M had minimized the light penetration and scattered the light transmission to activate the photocatalysis process

and thus weakened the segregation of  $e_{cb}^- - h_{vb}^+$  pairs of the binary photocatalyst (Choudhury and Gogoi, 2021). This finding was consistent with other literatures (Raja, Son and Kang, 2021; Sun, et al., 2021b; Zhang, et al., 2021d).

Liu and co-workers (2020b) examined the effect of MXene loading in MXene  $\text{Ti}_3\text{C}_2/\text{TiO}_2/\text{BiOCl}$  ternary composites in the degradation of RhB dye under Xenon lamp for 120 min. In their studies, the increase in the MXene co-catalyst loading from 1% to 4%, the photodegradation efficiency improved from 60% to 85%. When the loading was further elevated to 5%, the degradation rate was declined to 75%. They explained that proper weightage of MXene in ternary composite exhibited good photocatalytic activities due to the improved charge transmission and prolonged of the recombination of charge carrier. Declining in the photocatalysis with the increasing in the MXene loading caused the shielding effect and deteriorated the light absorption capability. Another study conducted by Wang et al. (2021), the increase in the delaminated  $\text{Ti}_3\text{C}_2$  MXene loading in  $\text{Ti}_3\text{C}_2/\text{SnNb}_2\text{O}_6$  binary compound from 2% to 5% presented improved photocatalytic removal of tetracycline hydrochloride from 55% to 70%. However, when the  $\text{Ti}_3\text{C}_2$  loading was increased to 10%, the reactivity was showed declination. They described that the black  $\text{Ti}_3\text{C}_2$  with appropriate amount can be advantageous for improving the light absorption capacities. Nevertheless, the higher quantity of  $\text{Ti}_3\text{C}_2$  will tends to convert the photon into thermal energy which suppress the photocatalytic performance.

### 4.3.3 Effect of Solution pH

The solution pH is a crucial operational parameter of the photocatalysis as it affects the surface of photocatalyst which directly influences the photocatalytic activity. In the present study, the effect of RhB solution pH in the photocatalytic degradation performance was carried out with pH ranging from pH 2 to pH 12, while the other parameters were remained constant. The solution pH was adjusted by the addition of 1.0 M HCl or 1.0 M KOH. Figure 4.15 displays the photocatalytic activities of D-M/NFO/V ternary composite at different solution pH under the LED light irradiation for 4 h. In the natural pH (without adding pH adjuster), the photodegradation rate of

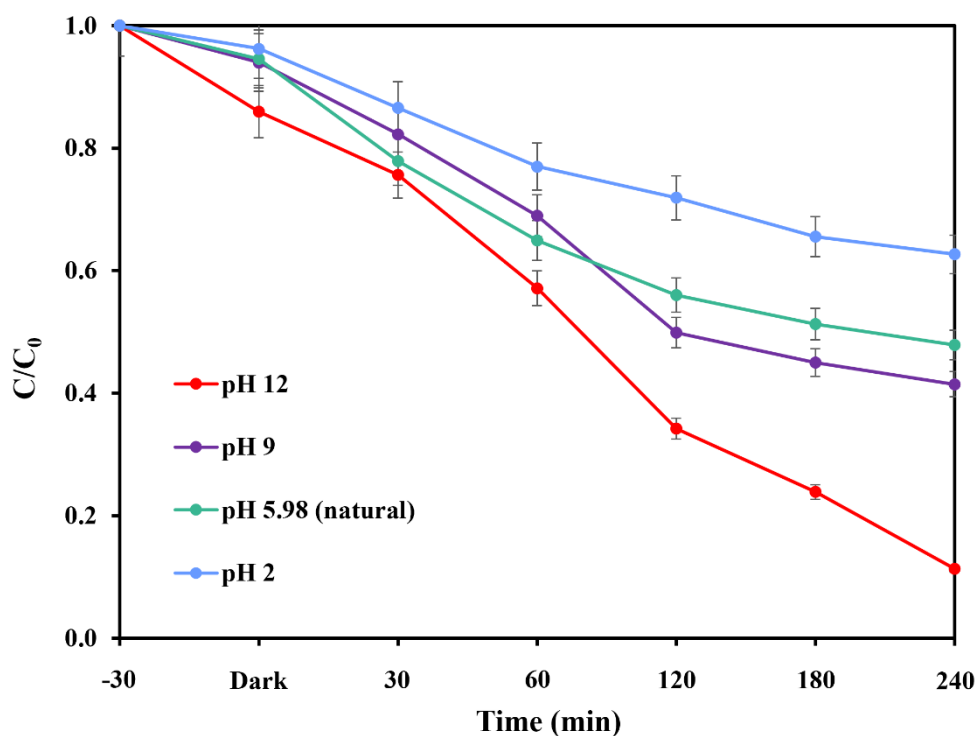


**Figure 4.15: Photocatalytic Activity of D-M/NFO/V ternary composite at different solution pH toward Degradation of RhB ([RhB] = 5 mg/L; [Catalyst] = 0.5 g/L).**

RhB was low with removal efficiency of 52.2%. Increasing the solution pH to pH 9 and 12, the photodegradation efficiencies were 58.6% and 88.7%, respectively. On the contrary, when the solution pH was altered to 2, the photocatalysis efficiency was suppressed to 42.8%.

The photocatalytic degradation of dye can be attributed to the three mechanisms, (1) direct reduction by photoexcited  $e_{cb}^-$ , (2) direct oxidation by photoinduced  $h_{vb}^+$ , and (3) attacking by  $\bullet\text{OH}$  radicals (Rafiq, et al., 2021). At lower pH, photoinduced  $h_{vb}^+$  can be generated as the major reactive oxygen species (ROS), meanwhile the  $\bullet\text{OH}$  radicals can be produced at higher solution pH. Another factor caused by the effect of solution pH was the surface chemistry of the photocatalyst. At higher pH environment, deprotonation process occurred and the surface of the photocatalyst will become positively charged. On the contrary, protonation process will occur in acidic condition which led to the positively charged surface of the photocatalyst (Javanbakht and Mohammadian, 2021).

RhB is a cationic dye which will ionise into positively charged ions in aqueous solution. As illustrated in figure, the outstanding degradation of cationic RhB was obtained at pH 12. This was ascribed to the surface of the D-M/NFO/V had become negatively charged and attracted to the positively charged RhB molecule by strong electrostatic forces. Moreover, the higher concentration of OH<sup>-</sup> ions at higher pH contributed to the generation of abundant of •OH radicals, which was responsible for the photodegradation process (Lohar, et al., 2021; Sutar, Barkul and Patil, 2021; Vema, et al., 2021). Furthermore, the photocatalytic performance was deteriorated at lower solution pH. This can be explained as the surface repulsion between protonated photocatalyst in acidic condition with cationic RhB.

Consistent results were reported in the literature studies (Li, et al., 2021c; Sutar, Barkul and Patil, 2021; Wang, et al., 2021b). Sutar and co-workers (2021) conducted the study to investigate the effect of pH in the degradation of cationic dye using ZnO-Zn<sub>2</sub>TiO<sub>4</sub> (ZT) catalyst. The optimum pH in photodegradation of dye was obtained at pH 11 under the irradiation of sunlight for 7 h. They explained that the excellent photocatalytic performance obtained at higher pH was due to the generation of •OH radicals as well as the strong electrostatic attractions between the anionic surface of ZT catalyst and cationic dye. Another report by Li, et al. (2021c) demonstrated that the highest photocatalytic degradation of astrazon brilliant red (ABR) dye removal was obtained at the alkaline environment (pH 11). They justified that the remarkable high degradation efficiency was due to the generation of •OH and •O<sub>2</sub><sup>-</sup> radical under alkaline pH superior to that in acidic pH.

#### **4.4 Antimicrobial Activities**

The microbial pathogens, including *S. aureus*, *E. coli*, *B. cereus*, *P. aeruginosa*, *K. pneumoniae*, and *P. Vulgaris* are present in real wastewater due to the high organic contents. The photocatalytic antibacterial activities were carried out by a spread plate method to observe the viable bacterial cell colonies. In the present study, the photocatalytic inhibition of gram-positive *Staphylococcus aureus* (*S. aureus*) and *Bacillus cereus* (*B. cereus*) were conducted under the LED light irradiation using the

synthesized photocatalysts. Figures 4.16 and 4.17 display the photocatalytic antibacterial activities toward *S. aureus* and *B. cereus*, respectively under LED light irradiation for 240 min. The results demonstrated that under the photolysis (without photocatalyst), no observable change indicating both *S. aureus* and *B. cereus* cannot be inhibited under the LED light. When the synthesized photocatalysts were added to evaluate the photocatalytic disinfection activities, the number of bacterial colonies had noticeable reduction as compared to that of photolysis. The disinfection effect was not observable under the dark condition. Comparing the photocatalytic antibacterial activities of V and NFO unary samples, both the binary NFO/V and ternary D-M/NFO/V composites exhibited higher disinfection effects. Among the samples, the ternary composite displayed the remarkable antibacterial activities. The order of the photocatalytic antibacterial activities of the synthesized photocatalyst against *S. aureus* was as followed: D-M/NFO/V > NFO/V > V > NFO. Similar order for the photocatalytic inhibition of *B. cereus*.

The photocatalytic disinfection of bacteria was influenced by various factors including morphology, surface charges and generation of ROS. The slight disinfection effect was observed for all the photocatalysts under the dark condition. The results can be attributed to the production of positively charged ions ( $V^{5+}$ ,  $Ni^{2+}$ ,  $Fe^{3+}$ ,  $Ti^{4+}$ ) from the respective samples (Karthik, et al., 2019; Hajipour, et al., 2021; Li, et al., 2021d). The release of cations adsorbed by the negatively charged bacteria cell wall and destroyed the cell wall causing the dead of bacteria. On the other hand, under the LED light irradiation, the photocatalytic inhibition of *S. aureus* was observed after 240 min. This could be ascribed to the photogenerated  $e_{cb}^- - h_{vb}^+$  pairs leading to the production of ROS responsible for cell inhibition. The formation of  $\bullet OH$  and  $\bullet O_2^-$  radicals reacted with intercellular cytoplasm and bacterial membrane. Consequently, led to the dysfunction of cell walls, peroxidation of lipids membranes, oxidation of proteins as well as denaturation of DNA (Jayaraj, et al., 2019; Alsafari, et al., 2021; Ma, et al., 2021b).

The D-M/NFO/V exhibited the profound photocatalytic inhibition of *S. aureus* under LED irradiation for 240 min. The results can be attributed to the effective  $e_{cb}^- - h_{vb}^+$  pairs separation for yielding the highest amount of  $\bullet OH$  and  $\bullet O_2^-$  radicals responsible for the redox reaction in killing the bacteria cells (Liu, et al., 2021).

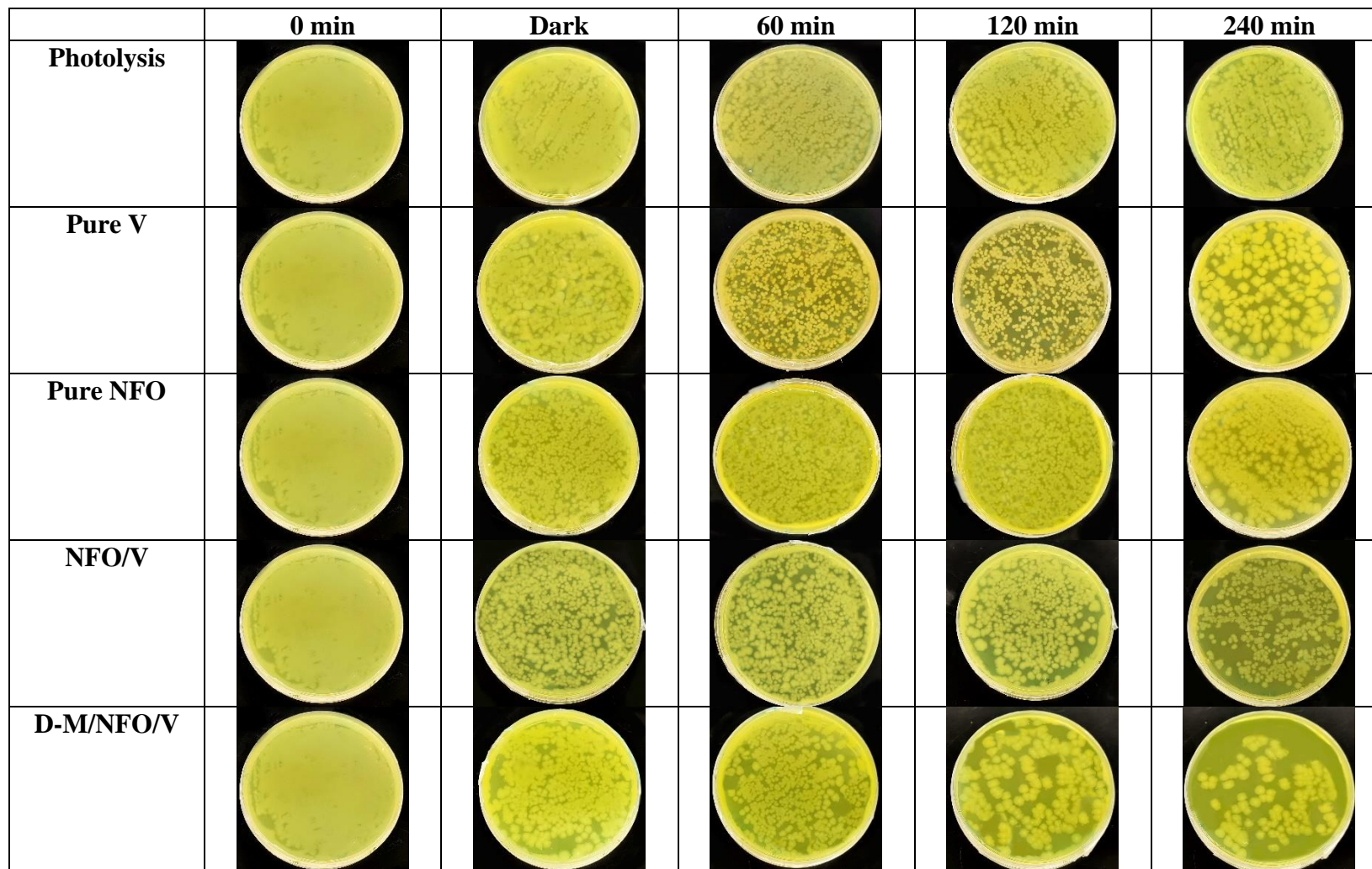


**Figure 4.16: The Photocatalytic Antibacterial Activities toward *S. aureus* under as-prepared Photocatalysts.**

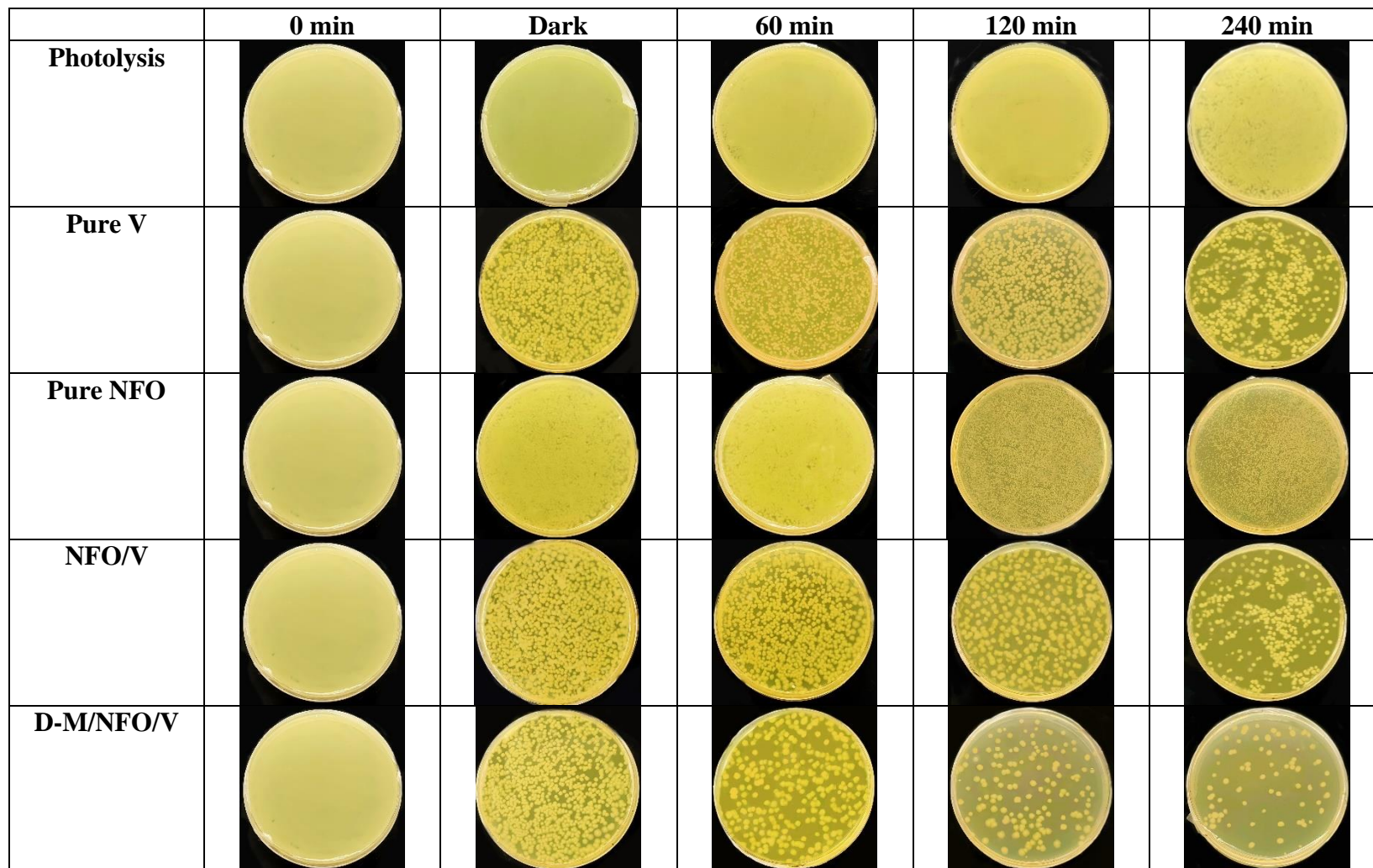


**Figure 4.17: The Photocatalytic Antibacterial Activities toward *B. cereus* under as-prepared Photocatalysts.**

Moreover, the existence of positive ions ( $V^{5+}$ ,  $Ni^{2+}$ ,  $Fe^{3+}$ ,  $Ti^{4+}$ ) attacked and entered the negatively charged bacterial cell membrane subsequently led to the cell denatured (Li, et al., 2021d). As compared the NFO/V to the D-M/NFO/V ternary composites, the incorporation of D-M enhanced the photocatalytic antibacterial effects. This revealed that the D-M co-catalyst boosted the migration of photogenerated  $e_{cb}^-$  and hence prolonged the recombination rate (Feng, et al., 2021; Shi, et al., 2021). Additionally, the structure of D-M existed as thin and sharp sheets also helped for the destroying of bacteria cells through direct physical interactions (Wang, et al., 2020).

Wang and co-workers (2020) conducted the photocatalytic antibacterial activities using  $Cu_2O$  anchored MXene toward *S. aureus* and *P. aeruginosa*. The enhanced antibacterial activities were observed on  $Cu_2O$ /MXene when compared to pure  $Cu_2O$  and MXene. They explained that the binary composite had improved the charge separation for promoting high yield ROS responsible for antibacterial capability. Furthermore, the sharp edges MXene also damaged the bacterial cell wall via direct physical contacts leading to the leakage of DNA. Another study carried out by Hajipour et al. (2021), the photocatalytic disinfection of *S. aureus* under white light using  $CuO$  modified  $TiO_2$  composite material. High antibacterial activity was obtained for  $CuO/TiO_2$  sample due to the enhanced charge carrier separation for the formation of ROS. They described that the photogenerated  $\bullet OH$  responsible in the peroxidation of lipids layer resulting in the damaging of cell organelles as well as the DNA structure.

#### 4.5 Reactive Oxygen Species Responsible for RhB Removal

In the photocatalysis, the reactive oxygen species (ROS) played the important roles toward the degradation of RhB molecules. The role of each ROS was evaluated via the radical scavenging test by adding of ROS quencher to inhibit its activity. According to the literatures, the common free radical trapping agents including ammonium oxalate (AO), benzoquinone (BQ), isopropanol (IPA) and silver nitrate (AgN) to scavenge  $h_{vb}^+$ ,  $\bullet O_2^-$ ,  $\bullet OH$  and  $e_{cb}^-$ , respectively (Liu, et al., 2020c; Cao, et al., 2021; Veisi, et al., 2021; Zhao, et al., 2021). Figure 4.18 demonstrates the photocatalytic degradation of RhB using D-M/NFO/V ternary composite with and without adding of radical scavengers.

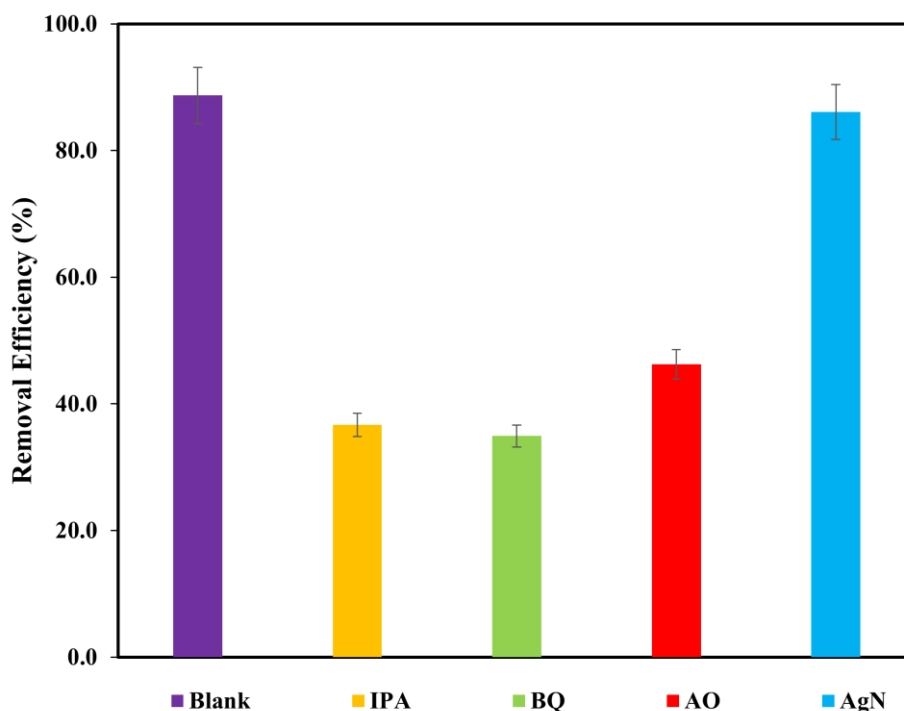


**Figure 4.18: Effects of Various Scavengers on LED light Photocatalytic Degradation of RhB over D-M/NFO/V Ternary Composite ([RhB] = 5 mg/L; [Catalyst] = 0.5 g/L; Solution pH = 12).**

As displayed in the figure, the dye removal efficiency was achieved at 88.7% under the LED light irradiation for 240 min without adding of any quencher. Meanwhile, with the addition of the respective trapping agents, the degradation rate was reduced drastically under the same condition. The photodegradation rate was deteriorated to 36.7%, 34.9%, 46.2% and 86.1% for  $\bullet\text{OH}$ ,  $\bullet\text{O}_2^-$ ,  $h_{vb}^+$  and  $e_{cb}^-$ , respectively. The results revealed that the order of reactive species responsible for the degradation of RhB molecules was as followed:  $\bullet\text{O}_2^- > \bullet\text{OH} > h_{vb}^+ > e_{cb}^-$

Among the ROS,  $\bullet\text{O}_2^-$  and  $\bullet\text{OH}$  were the major species for the degradation of RhB. This can be attributed to the band edge potential of the synthesized ternary materials which capable to generate more  $\bullet\text{O}_2^-$  and  $\bullet\text{OH}$  species for degradation process upon irradiation of LED light. As described in Sections 4.1.4 and 4.1.5, the band gap energy V photocatalyst was 2.78 eV with CB and VB potential of +0.46 eV and +3.24 eV, respectively. The well-positioned of the VB potential allowed it to generate the  $\bullet\text{OH}$  radical as the VB potential is more positive than the redox potential

of  $\text{H}_2\text{O}/\cdot\text{OH}$  (+2.70 eV vs NHE) (Hong, et al., 2016; Dadigala, et al., 2019; Chachvalvutikul, Luangwanta and Kaowphong, 2021). However, the CB potential of V is less negative than the redox potential of  $\text{O}_2/\cdot\text{O}_2^-$  (-0.33 eV vs NHE). As a result, no  $\cdot\text{O}_2^-$  radicals can be generated for the photocatalysis.

Furthermore, the coupled of NFO to V produced binary composite that can generate  $\cdot\text{O}_2^-$  and  $\cdot\text{OH}$  species for photodegradation of RhB. The band gap energy of NFO was 2.00 eV with CB position at -0.79 eV. These characteristics were contributed to the generation of  $\cdot\text{O}_2^-$  as the CB potential of NFO is more negative than the redox potential of  $\text{O}_2/\cdot\text{O}_2^-$  (Faraji, et al., 2021; Zhao, et al., 2021). D-M in the heterostructure work as the co-catalyst which trap the photogenerated  $e_{cb}^-$  and hence improved the performance of the photocatalysis (Li, et al., 2021a; Zhong, Li and Zhang, 2021). When the  $e_{cb}^-$  was scavenged in the aqueous solution, the degradation rate exhibited minor effect and good photocatalytic performance was observed. This could be assigned to the formation of Z-scheme heterojunction between NFO and V photocatalyst as well as D-M co-catalyst trapped the  $e_{cb}^-$  which providing good charge carrier separation for notably high photocatalytic activities (Cui, et al., 2020; Liu, et al., 2021b). The mechanism of the photodegradation of RhB using D-M/NFO/V ternary composite under the LED light irradiation was depicted in Figure 4.19.

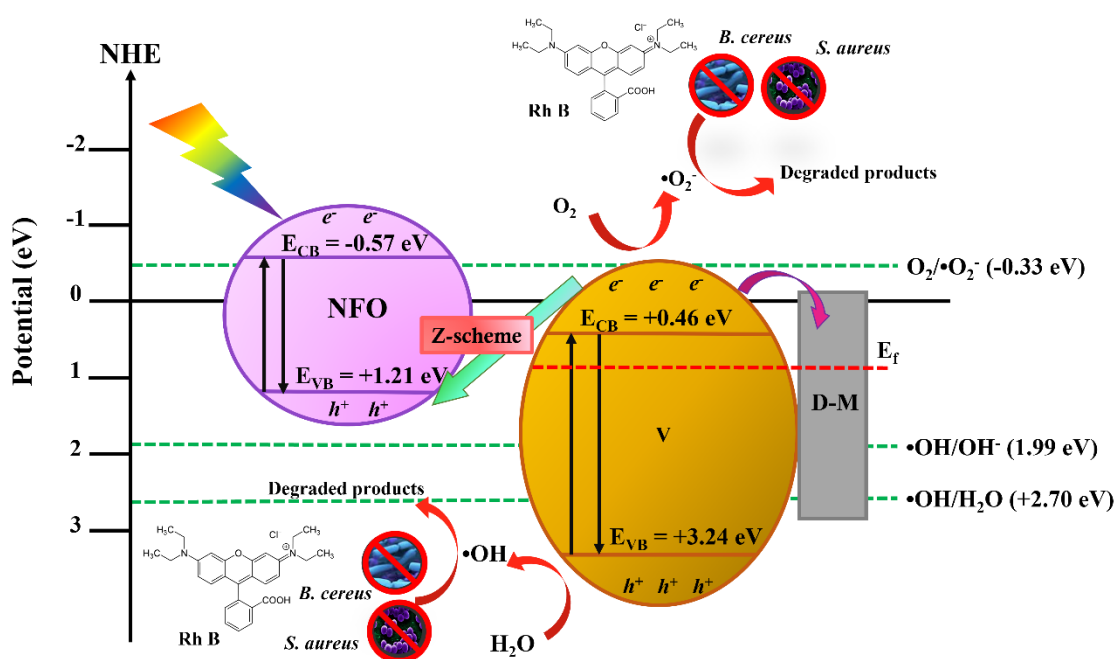


**Figure 4.19: Schematic diagram for Mechanism of Photodegradation over D-M/NFO/V Ternary Composite.**

#### 4.6 Reusability Study

The stability and reusability of the optimized ternary composite was evaluated through the recycling test. Generally, the D-M/NFO/V ternary sample was conducted with its photocatalytic activities toward the degradation of RhB. The collected sample was washed with ethanol and distilled for several times followed by drying in oven at 80°C for overnight (Liu, et al., 2020c). The dried sample was then used in the photocatalysis experiment three consecutive runs under the same condition to evaluate its reusability as well as the stability. Figure 4.20 demonstrates the recycling test of the optimized catalyst with four consecutive runs under the irradiation of LED light for 240 min treatment time. The results revealed that the photocatalytic degradation of RhB using the fresh sample was achieved at 88.7%. The dye removal efficiency remained notably high at 84.2% for the fourth cycle.

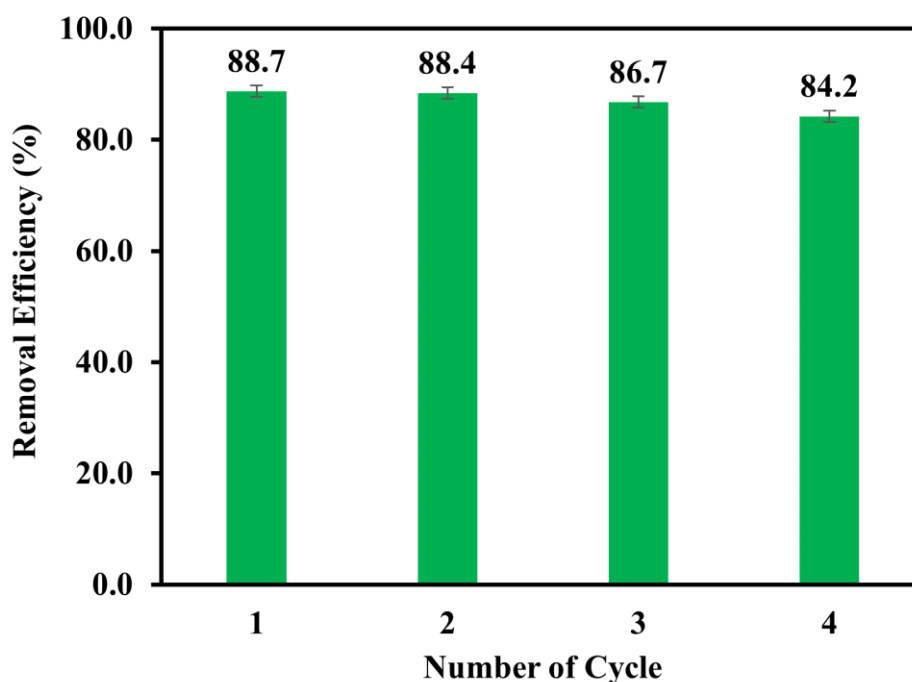


**Figure 4.20: The Recycling Experiment for the Photocatalytic Degradation of RhB over D-M/NFO/V ([RhB] = 5 mg/L; [Catalyst] = 0.5 g/L; Solution pH = 12).**

The photocatalytic performance remained at high dye removal efficiency after four cycles indicated the highly stable of the synthesized D-M/NFO/V ternary compound (Kumar, et al., 2020; Feizpoor, et al., 2021). The high stability of the composite revealed that it had higher capability to generate more radicals for notably

photocatalytic performance. However, there was slightly deterioration in the dye removal efficacy of the reused sample after the four cycles was noticed. It could be assigned to the inevitable loss of active photocatalyst during the washing and recovery process (Jayaraman, et al., 2019; Liu, et al., 2021b; Veisi, et al., 2021). Another reason for the insignificant declination in dye removal could be due to the indestructible RhB adsorbed on the photocatalyst's surface which led to the reducing in the catalyst active site for reactivity (Chachvalvutikul, Luangwanta and Kaowphong, 2021). The used sample was also easily to be recovered through external magnetic force after the reaction as depicted in Figures 4.21 (a) and (b).

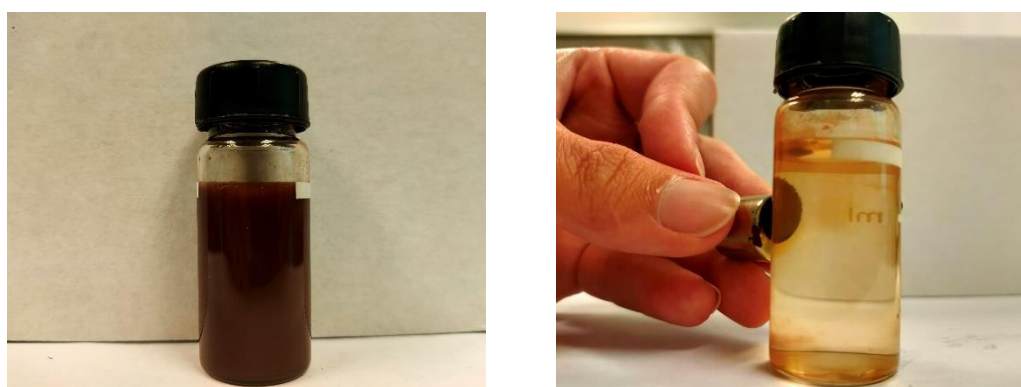


**Figure 4.21: D-M/NFO/V Ternary Composite (a) Suspended in aqueous and (b) Separated by External Magnetic Force.**

The results of the current study were agreed to several literature reports (Cui, et al., 2019; Jayaraman, et al., 2019; Rafique, et al., 2020; Zhang, et al., 2021a). Jayaraman and colleagues (2019) tested the stability and retrievability of  $\text{BiFeO}_3/\text{V}_2\text{O}_5$  for the degradation of methylene blue dye under visible light irradiation for 2 h. The result displayed that the synthesized sample retained high catalytic performance at 90% with minor degradation in activities after four cycles. They mentioned that the synthesized composite had high reproduction rate with little losses during the recovery process. Furthermore, another catalyst feasibility test conducted by Zhang and the teams (2021a) illustrated high photocatalytic activities toward methyl orange using  $\text{V}_2\text{O}_5/\text{P-g-C}_3\text{N}_4$  binary compound. High degradation rates were remained after four consecutive cycles of experiment. The results revealed that the high stability and recovery rate of the catalyst which could be practically applied in real wastewater treatment.

#### 4.7 Real Printed Ink Wastewater Study

The optimized D-M/NFO/V ternary composite was also tested using real printed ink wastewater to reveal its potential application in wastewater treatment. RhB was used as the synthetic dyestuff wastewater as it was widely adopted in various industries including textile, cosmetic, paper and pulp factories. In the present study, the real printed ink wastewater (PIWW) was applied in the optimized D-M/NFO/V ternary photocatalyst under the LED light illumination for 4 h. Table 4.3 depicts several water parameters with the degradation efficiency.

**Table 4.3: Parameters of the Real Printed Ink Wastewater before and after Photocatalytic Degradation using D-M/NFO/V Ternary Composite under LED light irradiation for 4 h.**

Parameters	Unit	Before Treatment	After Treatment	Efficiency (%)
COD	mg/L	43.0	21.0	51.2
BOD <sub>5</sub>	mg/L	54.8	36.8	32.9
Colour	Pt-co	355.0	55.0	84.5
Turbidity	NTU	64.5	4.2	93.6
pH	-	12.11	9.72	-

As shown in the table, the initial COD of the PIWW was 43.0 mg/L and the final COD of the wastewater after 4 h photocatalytic reaction under LED light was 21.0 mg/L, which indicated a degradation efficiency of 46.25%. Moreover, the initial and final BOD<sub>5</sub> of PIWW were 54.8 mg/L and 36.8 mg/L, respectively with degradation efficiency of 32.9%. On the other hand, remarkably high degradation efficiencies were obtained in colour and turbidity at 84.5% and 93.6%, respectively. The pH of the PIWW was adjusted to pH 12 to simulate the same treatment condition as in the degradation of synthetic RhB dye solution. A slight decrease in the solution pH from 12.11 to 9.72 was attained in the treatment of PIWW. This reduction of pH could be assigned to the reaction between the photogenerated  $h_{vb}^+$  at the valence band of the photocatalyst with OH<sup>-</sup> ions in aqueous solution to produce reactive •OH radicals. Subsequently, responsible in the photocatalytic degradation of pollutants in PIWW (Hasanpour and Hatami, 2020; Ma, et al., 2021a).

## CHAPTER 5

### CONCLUSION AND RECOMMENDATIONS

#### 5.1 Conclusion

In the present study, the ternary D-M/NFO/V composite was successfully synthesized via a simple thermal decomposition and applied in the dyestuff wastewater treatment and antimicrobial activity under LED light irradiation. The as synthesized photocatalysts were characterized through FESEM, EDX, XRD, UV-vis DRS and photoelectrochemical analyses. The irregular flake-like structure V and sphere-like particle NFO were witnessed in the microscopic images. Both V and NFO catalysts were found to disperse on the surface of single sheet-like D-M.

The EDX analysis showed that the ternary D-M/NFO/V compound contained V, Ni, Fe, O, Ti and C elements distributed evenly in the composite structure. The XRD analysis presented the orthorhombic pure V catalyst and cubic spinel pure NFO catalyst. The D-M illustrated in XRD patterns revealed the similar diffraction peaks as the MXene which consistent to the literatures. Moreover, the UV-Vis DRS analysis displayed the band gap energy of D-M/NFO/V, NFO/V, V and NFO were 2.45 eV, 2.63 eV, 2.78 eV and 2.00 eV, respectively. The photoelectrochemical experiments demonstrated that D-M/NFO/V exhibited the improved  $e_{cb}^- - h_{vb}^+$  pairs separation, which advantageous for the photocatalytic performance.

Using the RhB as the model pollutant, the D-M/NFO/V photocatalyst demonstrated profound visible light photocatalytic performance as compared to those of binary NFO/V and unary V and NFO. The enhanced photocatalytic was due to the

excellent charge separation efficiency that can be contributed to the generation of ROS. Several quality parameters studies of RhB such as COD, colour, turbidity and solution pH were degraded using the D-M/NFO/V ternary composite under the LED light irradiation.

Furthermore, the effect of several process parameter studies including NFO catalyst loadings in binary NFO/V compound, D-M co-catalyst loadings in D-M/NFO/V ternary composite and solution pH were investigated. The result of the present study concluded that the optimum NFO loading was 50 wt% to V catalyst, 0.5 wt% of D-M co-catalyst content in treating RhB dye under pH 12. A notable photodegradation efficiency of RhB was achieved at 88.7% using the D-M/NFO/V ternary composite under LED light irradiation in 240 min. The experimental results concluded that the appropriate weightage of NFO loadings and D-M co-catalyst loadings were highly influencing the photocatalytic performance.

The antimicrobial activity of the synthesized photocatalysts were determined against the inactivation activities of *S. aureus* and *B. cereus* under LED light irradiation for 240 min. The order of the antibacterial performance of the synthesized photocatalysts against *S. aureus* was as followed: D-M/NFO/V > NFO/V > V > NFO. Similar order was observed for the photocatalytic inhibition of *B. cereus*. The enhanced photocatalytic disinfection of microbial can be attributed to the following reasons: (1) production of positively charged ions ( $V^{5+}$ ,  $Ni^{2+}$ ,  $Fe^{3+}$ ,  $Ti^{4+}$ ) from the respective samples attacked and entered the negatively charged bacterial cell membrane; (2) the effective  $e_{cb}^- - h_{vb}^+$  pairs separation for yielding the highest amount of  $\bullet OH$  and  $\bullet O_2^-$  radicals responsible for the redox reaction in killing the bacteria cells; and (3) the structure of D-M existed as thin and sharp sheets for the destroying of bacteria cells through direct physical interactions.

Moreover, the roles of reactive oxygen species (ROS) in the photocatalysis were also studied. Among the ROS,  $\bullet O_2^-$  and  $\bullet OH$  were the major species for the degradation of RhB. This can be attributed to the suitability of band edge potential of the synthesized ternary materials, which capable to generate more  $\bullet O_2^-$  and  $\bullet OH$  species for degradation process upon irradiation of LED light. A possible mechanism

of the photodegradation of RhB using D-M/NFO/V ternary composite under the LED light irradiation was also proposed.

Additionally, the reusability of the optimized ternary composite was evaluated through the recycling test. The D-M/NFO/V ternary compound displayed outstanding recyclability which attained high removal efficiency of 84.2% after four successive runs. A slight deterioration in the dye removal efficacy of the reused sample over the four cycles was observed and this could be assigned to the inevitable loss of active photocatalyst during the washing and recovery process. Lastly, the optimized D-M/NFO/V ternary composite was also tested using real printed ink wastewater to reveal its potential application in wastewater treatment. The result demonstrated that several water parameters such as COD, BOD, colour, turbidity and pH were reduced under the LED light irradiation for 240 min. As a conclusion, this study revealed that the synthesized D-M/NFO/V ternary composite is a promising candidate for the photodegradation of organic pollutants and concurrently disinfection of microbial in the real dyestuff wastewater.

## **5.2 Recommendations**

Upon the completion of the present study, several fundamentals and engineering aspects were acquired and should be taken into consideration in the future research works.

1. The effect of other operation parameters such as the catalyst loading, velocity of air flow and light intensity could be investigated to further improve the photocatalytic degradation efficiency.
2. The photocatalytic degradation of other types of dyes including anionic and non-ionic dye as the real dyestuff wastewater contained various types of dye molecules.
3. The HPLC and GC analyses should be carried out to further evaluate the intermediates that may be produced during the photocatalytic reactions and to further study the photodegradation mechanism.

## REFERENCES

- Alakhras, F., Alhajri, E., Haounati, R., Ouachtak, H., Addi, A.A. and Saleh, T.A., 2020. A comparative study of photocatalytic degradation of Rhodamine B using natural-based zeolite composites. *Surfaces and Interfaces*, 20, pp. 100611 - 100619.
- Alhabeab, M., Maleski, K., Anasori, B., Lelyukh, P., Clark, L., Sin, S. and Gogotsi, Y., 2017. Guidelines for synthesis and processing of two-dimensional titanium carbide ( $\text{Ti}_3\text{C}_2\text{T}_x$  MXene). *Chemistry of Materials*, 29, pp. 7633 - 7644.
- Ali, M.M., Nair, J.S.A. and Sandhya, K.Y., 2019. Role of reactive oxygen species in the visible light photocatalytic mineralization of rhodamine B dye by P25-carbon dot photocatalyst. *Dyes and Pigments*, 163, pp. 274 - 284.
- Al-Mamun, M.R., Kader, S., Islam, M.S. and Khan, M.Z.H., 2019. Photocatalytic activity improvement and application of UV-TiO<sub>2</sub> photocatalysis in textile wastewater treatment: A review. *Journal of Environmental Chemical Engineering*, 7, p.103248.
- Alsafari, I.A., Munir, S., Zulfiqar, S., Saif, M.S., Warsi, M.F. and Shahid, M., 2021. Synthesis, characterization, photocatalytic and antibacterial properties of copper Ferrite/MXene ( $\text{CuFe}_2\text{O}_4/\text{Ti}_3\text{C}_2$ ) nanohybrids. *Ceramics International*, 47, pp. 28874 - 28883.
- Anantha, M.S., Jayanth, V., Olivera, S., Anarghya, D., Venkatesh, K., Jayanna, B.K., Sachin, H.P. and Muralidhara, H.B., 2021. Microwave treated Bermuda grass as a novel photocatalyst for the treatment of methylene blue dye from wastewater. *Environmental Nanotechnology, Monitoring & Management*, 15, p.100447.
- APHA, 2018. 5210 *Biological Oxygen Demand (BOD)*. [online] Standard Methods.org. Available at: <<https://www.standardmethods.org/doi/full/10.2105/SMWW.2882.102>> [Accessed 10 July 2021]
- Ariyanti, D., Maillot, M. and Gao, W., 2018. Photo-assisted degradation of dyes in a binary system using TiO<sub>2</sub> under simulated solar radiation. *Journal of environmental chemical engineering*, 6, pp. 539 - 548.
- Atacan, K., Güy, N. and Özacar, M., 2021. Design and synthesis of magnetically separable  $\text{CuFe}_2\text{O}_4/\text{MoS}_2$  p-n heterojunction for photocatalytic efficiency of

- Rhodamine B degradation. *Colloid and Interface Science Communications*, 40, pp. 100359 - 100369.
- Balasurya, S., Das, A., Alyousef, A.A., Alqasim, A., Almutairi, N. and Khan, S.S., 2021. Facile synthesis of Bi<sub>2</sub>MoO<sub>6</sub>-Ag<sub>2</sub>MoO<sub>4</sub> nanocomposite for the enhanced visible light photocatalytic removal of methylene blue and its antimicrobial application. *Journal of Molecular Liquids*, 337, p. 116350.
- Bethi, B., Sonawane, S.H., Bhanvase, B.A. and Gumfekar, S.P., 2016. Nanomaterials-based advanced oxidation processes for wastewater treatment: A review. *Chemical Engineering and Processing-Process Intensification*, 109, pp. 178 - 189.
- Bhat, A.P. and Gogate, P.R., 2020. Degradation of nitrogen-containing hazardous compounds using advanced oxidation processes: A review on aliphatic and aromatic amines, dyes, and pesticides. *Journal of Hazardous Materials*, 403, p. 123657.
- Bilińska, L., Blus, K., Foszpańczyk, M., Gmurek, M. and Ledakowicz, S., 2020. Catalytic ozonation of textile wastewater as a polishing step after industrial scale electrocoagulation. *Journal of Environmental Management*, 265, p. 110502.
- Borrás, M.C., Sluyter, R., Barker, P.J., Konstantinov, K. and Bakand, S., 2020. Y<sub>2</sub>O<sub>3</sub> decorated TiO<sub>2</sub> nanoparticles: Enhanced UV attenuation and suppressed photocatalytic activity with promise for cosmetic and sunscreen applications. *Journal of Photochemistry and Photobiology B: Biology*, 207, pp. 111883 - 111894.
- Bu, F., Zagho, M.M., Ibrahim, Y., Ma, B., Elzatahry, A. and Zhao, D., 2020. Porous MXenes: Synthesis, structures, and applications. *Nano Today*, 30, p. 100803.
- Byrne, C., Subramanian, G. and Pillai, S.C., 2018. Recent advances in photocatalysis for environmental applications. *Journal of Environmental Chemical Engineering*, 6, pp. 3531 - 3555.
- Cai, T., Wang, L., Liu, Y., Zhang, S., Dong, W., Chen, H., Yi, X., Yuan, J., Xia, X., Liu, C. and Luo, S., 2018. Ag<sub>3</sub>PO<sub>4</sub>/Ti<sub>3</sub>C<sub>2</sub> MXene interface materials as a Schottky catalyst with enhanced photocatalytic activities and anti-photocorrosion performance. *Applied Catalysis B: Environmental*, 239, pp. 545 - 554.
- Cao, J., Jing, Y., Du, Z., Chu, W., Li, J. and Cen, W., 2021. WC/BiOCl binary composite photocatalyst for accelerating interfacial charge separation and sulfamethoxazole degradation. *Applied Surface Science*, 570, pp. 151201 - 151212.
- Cao, Y., Fang, Y., Lei, X., Tan, B., Hu, X., Liu, B. and Chen, Q., 2020. Fabrication of novel CuFe<sub>2</sub>O<sub>4</sub>/MXene hierarchical heterostructures for enhanced photocatalytic degradation of sulfonamides under visible light. *Journal of Hazardous Materials*, 387, p. 122021.
- Chachvalvutikul, A., Luangwanta, T. and Kaowphong, S., 2021. Double Z-scheme FeVO<sub>4</sub>/Bi<sub>4</sub>O<sub>5</sub>Br<sub>2</sub>/BiOBr ternary heterojunction photocatalyst for simultaneous

- photocatalytic removal of hexavalent chromium and rhodamine B. *Journal of Colloid and Interface Science*, 603, pp. 738 - 757.
- Chai, H.Y., Lam, S.M. and Sin, J.C., 2019. Green synthesis of magnetic Fe-doped ZnO nanoparticles via Hibiscus rosa-sinensis leaf extracts for boosted photocatalytic, antibacterial and antifungal activities. *Materials Letters*, 242, pp. 103 - 106.
- Chankhanittha, T. and Nanan, S., 2021. Visible-light-driven photocatalytic degradation of ofloxacin (OFL) antibiotic and Rhodamine B (RhB) dye by solvothermally grown ZnO/Bi<sub>2</sub>MoO<sub>6</sub> heterojunction. *Journal of Colloid and Interface Science*, 582, pp. 412 - 427.
- Chen, Q., Zhang, Y., Zhang, D. and Yang, Y., 2017. Ag and N co-doped TiO<sub>2</sub> nanostructured photocatalyst for printing and dyeing wastewater. *Journal of Water Process Engineering*, 16, pp.14-20.
- Chen, Y., Jiang, Z., Xu, L., Liu, C., Cheng, Y., Zou, Y. and Zhang, Q., 2021. Composite magnetic photocatalyst Bi<sub>24</sub>O<sub>31</sub>Br<sub>10</sub>/NiFe<sub>2</sub>O<sub>4</sub>: Hydrothermal preparation, characterization and photocatalytic mechanism. *Materials Science in Semiconductor Processing*, 126, pp. 105669 - 105680.
- Chen, Y., Qian, J., Wang, N., Xing, J. and Liu, L., 2020. In-situ synthesis of CNT/TiO<sub>2</sub> heterojunction nanocomposite and its efficient photocatalytic degradation of Rhodamine B dye. *Inorganic Chemistry Communications*, 119, p.108071.
- Choerudin, C., Arrahmah, F.I., Daniel, J.K., Watari, T., Yamaguchi, T. and Setiadi, T., 2021. Evaluation of combined anaerobic membrane bioreactor and downflow hanging sponge reactor for treatment of synthetic textile wastewater. *Journal of Environmental Chemical Engineering*, 9, p. 105276.
- Choudhury, B.K. and Gogoi, S.K., 2021. Reduced graphene oxide and Ag/AgCl composite (RGO–Ag/AgCl) for photocatalytic degradation of RhB using WLED. *Nano-Structures & Nano-Objects*, 26, pp. 100704 - 100714.
- Clark, J., 2016. *The Beer-Lambert Law*. [online] Chemguide.co.uk. Available at: <<https://www.chemguide.co.uk/analysis/uvvisible/beerlambert.html>> [Accessed 31 March 2021]
- Corona-Bautista, M., Picos-Benítez, A., Villaseñor-Basulto, D., Bandala, E. and Peralta-Hernández, J.M., 2021. Discoloration of azo dye Brown HT using different advanced oxidation processes. *Chemosphere*, 267, p.129234.
- Cui, C., Guo, R., Xiao, H., Ren, E., Song, Q., Xiang, C., Lai, X., Lan, J. and Jiang, S., 2020. Bi<sub>2</sub>WO<sub>6</sub>/Nb<sub>2</sub>CT<sub>x</sub> MXene hybrid nanosheets with enhanced visible-light-driven photocatalytic activity for organic pollutants degradation. *Applied Surface Science*, 505, pp. 144595 - 144605.
- Cui, X., Liu, Z., Li, G., Zhang, M., Song, Y. and Wang, J., 2019. Self-generating CeVO<sub>4</sub> as conductive channel within CeO<sub>2</sub>/CeVO<sub>4</sub>/V<sub>2</sub>O<sub>5</sub> to induce Z-scheme-

- charge-transfer driven photocatalytic degradation coupled with hydrogen production. *International Journal of Hydrogen Energy*, 44, pp. 23921 - 23935.
- Dadigala, R., Bandi, R., Gangapuram, B.V., Dasari, A., Belay, H.H. and Guttena, V., 2019. Fabrication of novel 1D/2D  $V_2O_5/g-C_3N_4$  composites as Z-scheme photocatalysts for CR degradation and Cr (VI) reduction under sunlight irradiation. *Journal of Environmental Chemical Engineering*, 7, pp. 102822 - 102833.
- Department of Environment, 2010. Environmental Requirements: A Guide for Investors. [pdf] Putrajaya, Malaysia: DOE. Available at: <<https://www.doe.gov.my/portalv1/wp-content/uploads/2010/12/A-Guide-For-Investors.pdf>> [Accessed 18 March 2021]
- Dewil, R., Mantzavinos, D., Poulios, I. and Rodrigo, M.A., 2017. New perspectives for advanced oxidation processes. *Journal of Environmental Management*, 195, pp.93 - 99.
- Dixit, F., Zimmermann, K., Dutta, R., Prakash, N.J., Barbeau, B., Mohseni, M. and Kandasubramanian, B., 2022. Application of MXenes for water treatment and energy-efficient desalination: A review. *Journal of Hazardous Materials*, 423 pp.127050 - 127068.
- Duan, X., Yang, J., Hu, G., Yang, C., Chen, Y., Liu, Q., Ren, S. and Li, J., 2021. Optimization of  $TiO_2/ZSM-5$  photocatalysts: Energy band engineering by solid state diffusion method with calcination. *Journal of Environmental Chemical Engineering*, 9, pp. 105563 - 105574.
- Emamjomeh, M., Kakavand, S., Jamali, H., Alizadeh, S.M., Safdari, M., Mousavi, S.E.S., Hashim, K.S. and Mousazadeh, M., 2020. The treatment of printing and packaging wastewater by electrocoagulation–flotation: the simultaneous efficacy of critical parameters and economics. *Desalination and Water Treatment*, 205, pp. 161 – 174.
- Erkan, H.S., Çağlak, A., Soysalolu, A., Takatas, B. and Engin, G.O., 2020. Performance evaluation of conventional membrane bioreactor and moving bed membrane bioreactor for synthetic textile wastewater treatment. *Journal of Water Process Engineering*, 38, p. 101631.
- Fan, H., Yi, G., Zhang, Z., Zhang, X., Li, P., Zhang, C., Chen, L., Zhang, Y. and Sun, Q., 2021. Binary  $TiO_2/RGO$  photocatalyst for enhanced degradation of phenol and its application in underground coal gasification wastewater treatment. *Optical Materials*, 120, pp. 111482 - 111491.
- Fang, Y., Cao, Y. and Chen, Q., 2019. Synthesis of an  $Ag_2WO_4/Ti_3C_2$  Schottky composite by electrostatic traction and its photocatalytic activity. *Ceramics International*, 45, pp. 22298 - 22307.
- Faraji, A., Mehrdadi, N., Mahmoodi, N.M., Baghdadi, M. and Pardakhti, A., 2021. Enhanced photocatalytic activity by synergic action of ZIF-8 and  $NiFe_2O_4$  under visible light irradiation. *Journal of Molecular Structure*, 1223, pp. 129028 - 129037.

- Farrell, C., Hassard, F., Jefferson, B., Leziart, T., Nocker, A. and Jarvis, P., 2018. Turbidity composition and the relationship with microbial attachment and UV inactivation efficacy. *Science of the Total Environment*, 624, pp. 638 - 647.
- Feizpoor, S., Habibi-Yangjeh, A., Chand, H. and Krishnan, V., 2021. Integration of Bi<sub>5</sub>O<sub>7</sub>I with TiO<sub>2</sub>: Binary photocatalysts with boosted visible-light photocatalysis in removal of organic contaminants. *Journal of Photochemistry and Photobiology A: Chemistry*, 410, pp. 113190 - 113203.
- Feng, H., Wang, W., Wang, W., Zhang, M., Wang, C., Ma, C., Li, W. and Chen, S., 2021. Charge transfer channels of silver@ cuprous oxide heterostructure core-shell nanoparticles strengthen high photocatalytic antibacterial activity. *Journal of Colloid and Interface Science*, 601, pp. 531 - 543.
- Frindy, S. and Sillanpää, M., 2020. Synthesis and application of novel  $\alpha$ -Fe<sub>2</sub>O<sub>3</sub>/graphene for visible-light enhanced photocatalytic degradation of RhB. *Materials & Design*, 188, p. 108461.
- Gensemer, R.W., Gondek, J.C., Rodriguez, P.H., Arbildua, J.J., Stubblefield, W.A., Cardwell, A.S., Santore, R.C., Ryan, A.C., Adams, W.J. and Nordheim, E., 2018. Evaluating the effects of pH, hardness, and dissolved organic carbon on the toxicity of aluminum to freshwater aquatic organisms under circumneutral conditions. *Environmental Toxicology and Chemistry*, 37, pp. 49 - 60.
- Ghorai, K., Panda, A., Bhattacharjee, M., Mandal, D., Hossain, A., Bera, P., Seikh, M.M. and Gayen, A., 2021. Facile synthesis of CuCr<sub>2</sub>O<sub>4</sub>/CeO<sub>2</sub> nanocomposite: A new Fenton like catalyst with domestic LED light assisted improved photocatalytic activity for the degradation of RhB, MB and MO dyes. *Applied Surface Science*, 536, p. 147604.
- GilPavas, E., Dobrosz-Gómez, I. and Gómez-García, M.Á., 2018. Optimization of sequential chemical coagulation-electro-oxidation process for the treatment of an industrial textile wastewater. *Journal of Water Process Engineering*, 22, pp. 73 - 79.
- Govindaraj., T., Mahedrana, C., Archana, J., Shkir, M. and Chandrasekaran, J., 2021. Fabrication of WO<sub>3</sub> nanorods/RGO hybrid nanostructures for enhanced visible-light-driven photocatalytic degradation of Ciprofloxacin and Rhodamine B in an ecosystem. *Journal of Alloys and Compounds*, 868 (2021), pp. 159091 - 159104.
- HACH, 2014. *Water analysis handbook* (10<sup>th</sup> ed.). US: Hach Company, USA.
- HACH, 2019. *Water analysis handbook* (10<sup>th</sup> ed.). US: Hach Company, USA.
- Hajipour, P., Eslami, A., Bahrami, A., Hosseini-Abari, A., Saber, F.Y., Mohammadi, R. and Mehr, M.Y., 2021. Surface modification of TiO<sub>2</sub> nanoparticles with CuO for visible-light antibacterial applications and photocatalytic degradation of antibiotics. *Ceramics International*, 47, pp. 33875 - 33885.
- Hamdy, M.S., Abd-Rabboh, H.S., Benaissa, M., Al-Metwaly, M.G., Galal, A.H. and Ahmed, M.A., 2021. Fabrication of novel polyaniline/ZnO heterojunction for

- exceptional photocatalytic hydrogen production and degradation of fluorescein dye through direct Z-scheme mechanism. *Optical Materials*, 117, p. 111198.
- Hanna Instruments, 2018. Instruction Manual- HI 98703 Portable Turbidimeter. [online] Available at: <<https://www.hannainstruments.co.uk/turbidity-meter.html>> [Accessed 10 July 2021]
- Hasanpour, M. and Hatami, M., 2020. Photocatalytic performance of aerogels for organic dyes removal from wastewaters: Review study. *Journal of Molecular Liquids*, 309, pp. 113094 - 113115.
- Hiremath, V., Deonikar, V.G., Kim, H. and Seo, J.G., 2020. Hierarchically assembled porous TiO<sub>2</sub> nanoparticles with enhanced photocatalytic activity towards Rhodamine-B degradation. *Colloids and Surfaces A: Physicochemical and Engineering Aspects*, 586, pp. 124199 - 124210.
- Holkar, C.R., Jadhav, A.J., Pinjari, D.V., Mahamuni, N.M. and Pandit, A.B., 2016. A critical review on textile wastewater treatments: possible approaches. *Journal of Environmental Management*, 182, pp. 351 - 366.
- Hong, Y., Jiang, Y., Li, C., Fan, W., Yan, X., Yan, M. and Shi, W., 2016. In-situ synthesis of direct solid-state Z-scheme V<sub>2</sub>O<sub>5</sub>/g-C<sub>3</sub>N<sub>4</sub> heterojunctions with enhanced visible light efficiency in photocatalytic degradation of pollutants. *Applied Catalysis B: Environmental*, 180, pp. 663 - 673.
- Hu, J., Ding, J. and Zhong, Q., 2021. Ultrathin 2D Ti<sub>3</sub>C<sub>2</sub> MXene Co-catalyst anchored on porous g-C<sub>3</sub>N<sub>4</sub> for enhanced photocatalytic CO<sub>2</sub> reduction under visible-light irradiation. *Journal of Colloid and Interface Science*, 582, pp. 647 - 657.
- Huang, M., Li, J., Huang, Y., Zhou, X., Qin, Z., Tong, Z., Fan, M., Li, B. and Dong, L., 2021. Construction of g-C<sub>3</sub>N<sub>4</sub> based heterojunction photocatalyst by coupling TiO<sub>2</sub>-SnO<sub>2</sub> solid solution for efficient multipurpose photocatalysis. *Journal of Alloys and Compounds*, 864, pp.158132 - 158145.
- Hwang, S.K., Kang, S.M., Rethinasabapathy, M., Roh, C. and Huh, Y.S., 2020. MXene: An emerging two-dimensional layered material for removal of radioactive pollutants. *Chemical Engineering Journal*, 397, pp. 125428 - 125445.
- Ihsanullah, I., 2020. MXenes (two-dimensional metal carbides) as emerging nanomaterials for water purification: Progress, challenges and prospects. *Chemical Engineering Journal*, 388, pp. 124340 - 124357.
- Ismael, M., 2020. A review on graphitic carbon nitride (g-C<sub>3</sub>N<sub>4</sub>) based nanocomposites: Synthesis, categories, and their application in photocatalysis. *Journal of Alloys and Compounds*, 846, p.156446.
- Jaffari, Z.H., Lam, S.M., Sin, J.C. and Mohamed, A.R., 2019a. Constructing magnetic Pt-loaded BiFeO<sub>3</sub> nanocomposite for boosted visible light photocatalytic and antibacterial activities. *Environmental Science and Pollution Research*, 26, pp. 10204 -10218.

- Jaffari, Z.H., Lam, S.M., Sin, J.C. and Zeng, H., 2019b. Boosting visible light photocatalytic and antibacterial performance by decoration of silver on magnetic spindle-like bismuth ferrite. *Materials Science in Semiconductor Processing*, 101, pp. 103 -115.
- Javanbakht, V. and Mohammadian, M., 2021. Photo-assisted advanced oxidation processes for efficient removal of anionic and cationic dyes using Bentonite/TiO<sub>2</sub> nano-photocatalyst immobilized with silver nanoparticles. *Journal of Molecular Structure*, 1239, pp. 130496 - 130508.
- Jayaraj, S. K. and Paramasivam, T., 2019. Surface engineering of Au decorated V<sub>2</sub>O<sub>5</sub> nanorods-Enhanced photodegradation of Rh-6G under visible light with high cyclability and stability'. *Journal of Environmental Chemical Engineering*, 7, pp. 103512 - 103524.
- Jayaraj, S.K. and Paramasivam, T., 2018. Enhanced visible-light-driven photodegradation of Rh-6G by surface engineered Pd-V<sub>2</sub>O<sub>5</sub> heterostructure nanorods. *Journal of Environmental Chemical Engineering*, 6, pp.5320 - 5331.
- Jayaraj., S.K., Sadishkumar, V., Arun, T. and Thangadurai, P., 2018. Enhanced photocatalytic activity of V<sub>2</sub>O<sub>5</sub> nanorods for the photodegradation of organic dyes: A detailed understanding of the mechanism and their antibacterial activity. *Materials Science in Semiconductor Processing*, 85, pp. 122 - 133.
- Jayaraman, V., Sarkar, D., Rajendran, R., Palanivel, B., Ayappan, C., Chellamuthu, M. and Mani, A., 2019. Synergistic effect of band edge potentials on BiFeO<sub>3</sub>/V<sub>2</sub>O<sub>5</sub> composite: enhanced photo catalytic activity. *Journal of Environmental Management*, 247, pp. 104 - 114.
- Jegatheesan, V., Pramanik, B.K., Chen, J., Navaratna, D., Chang, C.Y. and Shu, L., 2016. Treatment of textile wastewater with membrane bioreactor: a critical review. *Bioresource Technology*, 204, pp. 202 - 212.
- Jeon, M., Jun, B.M., Kim, S., Jang, M., Park, C.M., Snyder, S.A. and Yoon, Y., 2020. A review on MXene-based nanomaterials as adsorbents in aqueous solution. *Chemosphere*, 261, pp.127781 - 127799.
- Kanakaraju, D., Glass, B.D. and Oelgemöller, M., 2018. Advanced oxidation process-mediated removal of pharmaceuticals from water: a review. *Journal of Environmental Management*, 219, pp.189 - 207.
- Karthik, K., Nikolova, M.P., Phuruangrat, A., Pushpa, S., Revathi, V. and Subbulakshmi, M., 2020. Ultrasound-assisted synthesis of V<sub>2</sub>O<sub>5</sub> nanoparticles for photocatalytic and antibacterial studies. *Materials Research Innovations*, 24, pp. 229 - 234.
- Kausley, S.B., Desai, K.S., Shrivastava, S., Shah, P.R., Patil, B.R. and Pandit, A.B., 2018. Mineralization of alkyd resin wastewater: Feasibility of different advanced oxidation processes. *Journal of Environmental Chemical Engineering*, 6, pp. 3690-3701.

- Khalik, W.F., Ho, L.N., Ong, S.A., Voon, C.H., Wong, Y.S., Yusoff, N., Lee, S.L. and Yusuf, S.Y., 2017. Optimization of degradation of Reactive Black 5 (RB5) and electricity generation in solar photocatalytic fuel cell system. *Chemosphere*, 184, pp.112-119.
- Kishor, R., Purchase, D., Saratale, G.D., Saratale, R.G., Ferreira, L.F.R., Bilal, M., Chandra, R. and Bharagava, R.N., 2021. Ecotoxicological and health concerns of persistent coloring pollutants of textile industry wastewater and treatment approaches for environmental safety. *Journal of Environmental Chemical Engineering*, 9, p. 105012.
- Korpe, S. and Rao, P.V., 2021. Application of Advanced Oxidation Processes and Cavitation Techniques for Treatment of Tannery Wastewater-A Review. *Journal of Environmental Chemical Engineering*, 9, p. 105234.
- Kosera, V.S., Cruz, T.M., Chaves, E.S. and Tiburtius, E.R., 2017. Triclosan degradation by heterogeneous photocatalysis using ZnO immobilized in biopolymer as catalyst. *Journal of Photochemistry and Photobiology A: Chemistry*, 344, pp. 184-191.
- Kumar, A., Sharma, S.K., Sharma, G., Naushad, M. and Stadler, F.J., 2020. CeO<sub>2</sub>/g-C<sub>3</sub>N<sub>4</sub>/V<sub>2</sub>O<sub>5</sub> ternary nano hetero-structures decorated with CQDs for enhanced photo-reduction capabilities under different light sources: Dual Z-scheme mechanism. *Journal of Alloys and Compounds*, 838, p. 155692.
- Kumar, R.S., Ryu, J., Kim, H., Mergu, N., Park, J.Y., Shin, H.J., Kim, M.G., Lee, S.G. and Son, Y.A., 2021. Synthesis, characterization, and photocatalytic disinfection studies of porphyrin dimer/TiO<sub>2</sub>-based photocatalyst. *Journal of Molecular Structure*, 1236, p. 130276.
- Kwon, Y.J., Ko, W.C., Kang, S., Kim, K.M. and Jeong, Y.K., 2020. Surface passivation of highly stable TiO<sub>2</sub>/V<sub>2</sub>O<sub>5</sub> photocatalyst by atomic layer deposited-Al<sub>2</sub>O<sub>3</sub>. *Applied Surface Science*, 507, p. 145128.
- Lam, S.M., Sin, J.C., Lin, H., Li, H. and Zeng, H., 2020. Greywater and bacteria removal with synchronized energy production in photocatalytic fuel cell based on anodic TiO<sub>2</sub>/ZnO/Zn and cathodic CuO/Cu. *Chemosphere*, 245, p. 125565.
- Li, B., Kim, I.S., Dai, S., Sarwar, M.N. and Yang, X., 2021d. Heterogeneous Ag@ZnO nanorods decorated on polyacrylonitrile fiber membrane for enhancing the photocatalytic and antibacterial properties. *Colloid and Interface Science Communications*, 45, pp.100543 - 100553.
- Li, C.B., Xiao, F., Xu, W., Chu, Y., Wang, Q., Jiang, H., Li, K. and Gao, X.W., 2021c. Efficient self-photo-degradation of cationic textile dyes involved triethylamine and degradation pathway. *Chemosphere*, 266, pp. 129209 - 129217.
- Li, J. and Wu, N., 2015. Semiconductor-based photocatalysts and photoelectrochemical cells for solar fuel generation: a review. *Catalysis Science & Technology*, 5, pp. 1360 - 1384.

- Li, K., Zhang, S., Li, Y., Fan, J. and Lv, K., 2021a. MXenes as noble-metal-alternative co-catalysts in photocatalysis. *Chinese Journal of Catalysis*, 42, pp. 3-14.
- Li, N., Tang, S., Rao, Y., Qi, J., Wang, P., Jiang, Y., Huang, H., Gu, J. and Yuan, D., 2018. Improved dye removal and simultaneous electricity production in a photocatalytic fuel cell coupling with persulfate activation. *Electrochimica Acta*, 270, pp. 330-338.
- Li, Y., Ding, L., Liang, Z., Xue, Y., Cui, H. and Tian, J., 2020. Synergetic effect of defects rich MoS<sub>2</sub> and Ti<sub>3</sub>C<sub>2</sub> MXene as cocatalysts for enhanced photocatalytic H<sub>2</sub> production activity of TiO<sub>2</sub>. *Chemical Engineering Journal*, 383, p. 123178.
- Li, Y., Zheng, X., Yang, J., Zhao, Z. and Cui, S., 2021b. Enhanced photocatalytic degradation of 2, 4, 6-trichlorophenol and RhB with RhB-sensitized BiOClBr catalyst based on response surface methodology. *Journal of the Taiwan Institute of Chemical Engineers*, 119, pp.213-223.
- Liu, H., Yang, C., Jin, X., Zhong, J. and Li, J., 2020b. One-pot hydrothermal synthesis of MXene Ti<sub>3</sub>C<sub>2</sub>/TiO<sub>2</sub>/BiOCl ternary heterojunctions with improved separation of photoactivated carriers and photocatalytic behavior toward elimination of contaminants. *Colloids and Surfaces A: Physicochemical and Engineering Aspects*, 603, pp. 125239 - 125251.
- Liu, J., Zhou, S., Gu, P., Zhang, T., Chen, D., Li, N., Xu, Q. and Lu, J., 2020c. Conjugate Polymer-clothed TiO<sub>2</sub>@ V<sub>2</sub>O<sub>5</sub> nanobelts and their enhanced visible light photocatalytic performance in water remediation. *Journal of Colloid and Interface Science*, 578, pp. 402 - 411.
- Liu, N., Lu, N., Yu, H., Chen, S. and Quan, X., 2020a. Efficient day-night photocatalysis performance of 2D/2D Ti<sub>3</sub>C<sub>2</sub>/Porous g-C<sub>3</sub>N<sub>4</sub> nanolayers composite and its application in the degradation of organic pollutants. *Chemosphere*, 246, p. 125760.
- Liu, Y., Tian, Y., Han, Q., Yin, J., Zhang, J., Yu, Y., Yang, W. and Deng, Y., 2021a. Synergism of 2D/1D MXene/cobalt nanowire heterojunctions for boosted photo-activated antibacterial application. *Chemical Engineering Journal*, 410, pp.128209 - 128224.
- Liu, Z., Xu, K., Yu, H., Zhang, M. and Sun, Z., 2021b. In-situ preparation of double Z-scheme Bi<sub>2</sub>S<sub>3</sub>/BiVO<sub>4</sub>/TiO<sub>2</sub> ternary photocatalysts for enhanced photoelectrochemical and photocatalytic performance. *Applied Surface Science*, 545, pp.148986 - 148995.
- Lohar, S., Prajapati, D.K., Sharma, A. and Bhardwaj, S., 2021. Wastewater treatment using nanomaterial quaternary photocatalyst ZrCdPbO<sub>4</sub>-Removal of colour pollutant by an eco-friendly process. *Journal of the Indian Chemical Society*, 98, pp. 100194 - 100200.

- Ma, D., Yi, H., Lai, C., Liu, X., Huo, X., An, Z., Li, L., Fu, Y., Li, B., Zhang, M. and Qin, L., 2021a. Critical review of advanced oxidation processes in organic wastewater treatment. *Chemosphere*, 275, pp. 130104 - 130131.
- Ma, H., Yang, S., Tang, X., Xia, Z. and Dai, R., 2021b. Preparation and photocatalytic antibacterial mechanism of porous metastable  $\beta$ - $\text{Bi}_2\text{O}_3$  nanosheets. *Ceramics International*, 47, pp. 34092 - 34105.
- Ma, J., Ding, Y., Cheng, J.C., Jiang, F. and Xu, Z., 2020. Soft detection of 5-day BOD with sparse matrix in city harbor water using deep learning techniques. *Water Research*, 170, p. 115350.
- Makula, P., Pacia, M. and Macyk, W., 2018. How to correctly determine the band gap energy of modified semiconductor photocatalysts based on UV-Vis spectra. *The Journal of Physical Chemistry Letters*, 9, pp. 6814 – 6817.
- Manikandan, S., Karmegam, N., Subbaiya, R., Devi, G.K., Arulvel, R., Ravindran, B. and Awasthi, M.K., 2020. Emerging nano-structured innovative materials as adsorbents in wastewater treatment. *Bioresource Technology*, 320, pp. 124394 - 124405.
- Miklos, D.B., Remy, C., Jekel, M., Linden, K.G., Drewes, J.E. and Hübner, U., 2018. Evaluation of advanced oxidation processes for water and wastewater treatment—A critical review. *Water Research*, 139, pp. 118-131.
- Mishra, A., Panigrahi, A., Mal, P., Penta, S., Padmaja, G., Bera, G., Das, P., Rambabu, P. and Turpu, G.R., 2020. Rapid photodegradation of methylene blue dye by rGO- $\text{V}_2\text{O}_5$  nanocomposite. *Journal of Alloys and Compounds*, 842, pp. 155746 -155753.
- Mukhtar, F., Munawar, T., Nadeem, M.S., ur Rehman, M.N., Riaz, M. and Iqbal, F., 2021. Dual S-scheme heterojunction  $\text{ZnO}-\text{V}_2\text{O}_5-\text{WO}_3$  nanocomposite with enhanced photocatalytic and antimicrobial activity. *Materials Chemistry and Physics*, 263, pp. 124372 - 124385.
- Mustafa, H.M. and Hayder, G., 2021. Recent studies on applications of aquatic weed plants in phytoremediation of wastewater: A review article. *Ain Shams Engineering Journal*, 12, pp. 355 - 365.
- Mydeen, S.S., Kumar, R.R., Sambathkumar, S., Kottaisamy, M. and Vasantha, V.S., 2020. Facile Synthesis of ZnO/AC Nanocomposites using Prosopis Juliflora for Enhanced Photocatalytic Degradation of Methylene Blue and Antibacterial Activity. *Optik*, 224, p. 165426.
- Narenuch, T., Senasu, T., Chankhanittha, T. and Nanan, S., 2021. Solvothermal synthesis of CTAB capped and SDS capped BiOCl photocatalysts for degradation of rhodamine B (RhB) dye and fluoroquinolone antibiotics. *Journal of Solid State Chemistry*, 294, pp.121824 - 121838.
- Ng, K.H., Gan, Y.S., Cheng, C.K., Liu, K.H. and Liong, S.T., 2020. Integration of machine learning-based prediction for enhanced Model's generalization:

- Application in photocatalytic polishing of palm oil mill effluent (POME). *Environmental Pollution*, 267, p. 115500.
- Nivetha, P., Kavitha, B. and Kalanithi, M., 2021. Investigation of photocatalytic and antimicrobial activities of BaWO<sub>4</sub>-MoS<sub>2</sub> nanoflowers. *Journal of Science: Advanced Materials and Devices*, 6, pp. 65 - 74.
- Oh, S.R. and Kim, S., 2021. Micro-volume spectrophotometer with a slope spectroscopy technique. *Measurement*, 167, p. 108270.
- Papadopoulos, K.P., Argyriou, R., Economou, C.N., Charalampous, N., Dailianis, S., Tatoulis, T.I., Tekerlekopoulou, A.G. and Vayenas, D.V., 2019. Treatment of printing ink wastewater using electrocoagulation. *Journal of environmental management*, 237, pp.442-448.
- Paul, A. and Dhar, S.S., 2020. Construction of hierarchical MnMoO<sub>4</sub>/NiFe<sub>2</sub>O<sub>4</sub> nanocomposite: highly efficient visible light driven photocatalyst in the degradation of different polluting dyes in aqueous medium. *Colloids and Surfaces A: Physicochemical and Engineering Aspects*, 585, pp. 124090 -124100.
- Paumo, H.K., Dalhatou, S., Katata-Seru, L.M., Kamdem, B.P., Tijani, J.O., Vishwanathan, V., Kane, A. and Bahadur, I., 2021. TiO<sub>2</sub> assisted photocatalysts for degradation of emerging organic pollutants in water and wastewater. *Journal of Molecular Liquids*, 331, p. 115458.
- Prasad, A.R., Ammal, P.R. and Joseph, A., 2018. Effective photocatalytic removal of different dye stuffs using green synthesized zinc oxide nanogranules. *Materials Research Bulletin*, 102, pp. 116-121.
- Prasad, C., Yang, X., Liu, Q., Tang, H., Rammohan, A., Zulfiqar, S., Zyryanov, G.V. and Shah, S., 2020. Recent advances in MXenes supported semiconductors based photocatalysts: Properties, synthesis and photocatalytic applications. *Journal of Industrial and Engineering Chemistry*, 85, pp. 1 - 33.
- Qian, A., Pang, Y., Wang, G., Hao, Y., Liu, Y., Shi, H., Chung, C.H., Du, Z. and Cheng, F., 2020. Pseudocapacitive Charge Storage in MXene-V<sub>2</sub>O<sub>5</sub> for Asymmetric Flexible Energy Storage Devices. *ACS Applied Materials & Interfaces*, 12, pp. 54791 - 54797.
- Quek, J.A., Lam, S.M., Sin, J.C. and Mohamed, A.R., 2018. Visible light responsive flower-like ZnO in photocatalytic antibacterial mechanism towards *Enterococcus faecalis* and *Micrococcus luteus*. *Journal of Photochemistry and Photobiology B: Biology*, 187, pp. 66 - 75.
- Rafiq, A., Ikram, M., Ali, S., Niaz, F., Khan, M., Khan, Q. and Maqbool, M., 2021. Photocatalytic degradation of dyes using semiconductor photocatalysts to clean industrial water pollution. *Journal of Industrial and Engineering Chemistry*, 97, pp. 111-128.

- Rafique, M., Hamza, M., Shakil, M., Irshad, M., Tahir, M.B. and Kabli, M.R., 2020. Highly efficient and visible light-driven nickel-doped vanadium oxide photocatalyst for degradation of Rhodamine B Dye. *Applied Nanoscience*, 10, pp. 2365 - 2374.
- Raizada, P., Nguyen, T.H.C., Patial, S., Singh, P., Bajpai, A., Nguyen, V.H., Nguyen, D.L.T., Nguyen, X.C., Khan, A.A.P., Rangabhashiyam, S. and Kim, S.Y., 2021. Toward practical solar-driven photocatalytic water splitting on two-dimensional MoS<sub>2</sub> based solid-state Z-scheme and S-scheme heterostructure. *Fuel*, 303, pp. 121302 - 121319.
- Raja, A., Son, N. and Kang, M., 2021. Construction of visible-light driven Bi<sub>2</sub>MoO<sub>6</sub>-rGO-TiO<sub>2</sub> photocatalyst for effective ofloxacin degradation. *Environmental Research*, 199, pp.111261 - 111273.
- Rajalakshmi, S. and Pitchimuthu, S., 2017. Enhanced photocatalytic activity of metal oxides/ $\beta$ -cyclodextrin nanocomposites for decoloration of Rhodamine B dye under solar light irradiation. *Applied Water Science*, 7, pp. 115-127.
- Ramos, J.M.P., Pereira-Queiroz, N.M., Santos, D.H., Nascimento, J.R., de Carvalho, C.M., Tonholo, J. and Zanta, C.L., 2019. Printing ink effluent remediation: a comparison between electrochemical and Fenton treatments. *Journal of Water Process Engineering*, 31, p. 100803.
- Rasheed, T., Rasheed, A., Munir, S., Ajmal, S., Shahzad, Z.M., Alsafari, I.A., Ragab, S.A., Agboola, P.O. and Shakir, I., 2021. A cost-effective approach to synthesize NiFe<sub>2</sub>O<sub>4</sub>/MXene heterostructures for enhanced photodegradation performance and anti-bacterial activity. *Advanced Powder Technology*, 32, pp. 2248 - 2257.
- Reddy, C.V., Koutavarapu, R., Reddy, K.R., Shetti, N.P., Aminabhavi, T.M. and Shim, J., 2020. Z-scheme binary 1D ZnWO<sub>4</sub> nanorods decorated 2D NiFe<sub>2</sub>O<sub>4</sub> nanoplates as photocatalysts for high efficiency photocatalytic degradation of toxic organic pollutants from wastewater. *Journal of Environmental Management*, 268, pp. 110677 - 110689.
- Roshith, M., Pathak, A., Kumar, A.N., Anantharaj, G., Saranyan, V., Ramasubramanian, S., Babu, T.S. and Kumar, D.V.R., 2021. Continuous flow solar photocatalytic disinfection of E. coli using red phosphorus immobilized capillaries as optofluidic reactors. *Applied Surface Science*, 540, p. 148398.
- Sajid, M.M., Shad, N.A., Javed, Y., Khan, S.B., Zhang, Z., Amin, N. and Zhai, H., 2020. Preparation and characterization of Vanadium pentoxide (V<sub>2</sub>O<sub>5</sub>) for photocatalytic degradation of monoazo and diazo dyes. *Surfaces and Interfaces*, 19, pp. 100502 - 100511.
- Samsami, S., Mohamadi, M., Sarrafzadeh, M.H., Rene, E.R. and Firoozbahr, M., 2020. Recent advances in the treatment of dye-containing wastewater from textile industries: Overview and perspectives. *Process Safety and Environmental Protection*, 143, pp. 138 -163.

- Sela, S.K., Nayab-Ul-Hossain, A.K.M., Hussain, S.Z. and Hasan, N., 2020. Utilization of prawn to reduce the value of BOD and COD of textile wastewater. *Cleaner Engineering and Technology*, 1, p.100021.
- Sharma, A., Syed, Z., Brighu, U., Gupta, A.B. and Ram, C., 2019. Adsorption of textile wastewater on alkali-activated sand. *Journal of Cleaner Production*, 220, pp. 23-32.
- Shen, J., Shen, J., Zhang, W., Yu, X., Tang, H., Zhang, M. and Liu, Q., 2019. Built-in electric field induced CeO<sub>2</sub>/Ti<sub>3</sub>C<sub>2</sub>-MXene Schottky-junction for coupled photocatalytic tetracycline degradation and CO<sub>2</sub> reduction. *Ceramics International*, 45, pp. 24146 - 24153.
- Shen, J.H., Tang, Y.H., Jiang, Z.W., Liao, D.Q. and Horng, J.J., 2021. Optimized preparation and characterization of Co-N codoped TiO<sub>2</sub> with enhanced visible light activity: An insight into effect of dopants on surface redox reactions of photogenerated charge carriers for hydroxyl radical formation. *Journal of Alloys and Compounds*, 862, pp. 158697 - 158709.
- Shi, H., Wang, W., Zhang, L., Tang, Z. and Fan, J., 2021. Enhancement of photocatalytic disinfection performance the Bi<sub>4</sub>O<sub>5</sub>Br<sub>2</sub> with the modification of silver quantum dots. *Journal of Environmental Chemical Engineering*, 9, p. 105867.
- Shi, L., Ma, Z., Qu, W., Zhou, W., Deng, Z. and Zhang, H., 2021. Hierarchical Z-scheme Bi<sub>2</sub>S<sub>3</sub>/CdS heterojunction: Controllable morphology and excellent photocatalytic antibacterial. *Applied Surface Science*, 568, pp.150923 - 150933.
- Sin, J.C., Lam, S.M., Zeng, H., Lin, H., Li, H., Tham, K.O., Mohamed, A.R., Lim, J.W. and Qin, Z., 2021. Magnetic NiFe<sub>2</sub>O<sub>4</sub> nanoparticles decorated on N-doped BiOBr nanosheets for expeditious visible light photocatalytic phenol degradation and hexavalent chromium reduction via a Z-scheme heterojunction mechanism. *Applied Surface Science*, 559, pp. 149966 - 149981.
- Singh, G., Kumar, M. and Vaish, R., 2021. Promising multicycatalytic and adsorption capabilities in V<sub>2</sub>O<sub>5</sub>/BiVO<sub>4</sub> composite pellets for water-cleaning application. *Surfaces and Interfaces*, 23, p. 100924.
- Singh, J. and Basu, S., 2020. Synthesis of mesoporous magnetic Fe<sub>2</sub>O<sub>3</sub>/g-C<sub>3</sub>N<sub>4</sub> monoliths for Rhodamine B removal. *Microporous and Mesoporous Materials*, 303, p. 110299.
- Steplinpauselvin, S., Rajaram, R., Silambarasan, T.S. and Chen, Y., 2020. Survival assessment of simple food webs for dye wastewater after photocatalytic degradation using SnO<sub>2</sub>/GO nanocomposites under sunlight irradiation. *Science of The Total Environment*, 721, p.137805.
- Sun, B., Tao, F., Huang, Z., Yan, W., Zhang, Y., Dong, X., Wu, Y. and Zhou, G., 2021. Ti<sub>3</sub>C<sub>2</sub> MXene-bridged Ag/Ag<sub>3</sub>PO<sub>4</sub> hybrids toward enhanced visible-light-driven photocatalytic activity. *Applied Surface Science*, 535, pp.147354 – 147366.

- Sun, D., Mao, J., Cheng, L., Yang, X., Li, H., Zhang, L., Zhang, W., Zhang, Q. and Li, P., 2021a. Magnetic g-C<sub>3</sub>N<sub>4</sub>/NiFe<sub>2</sub>O<sub>4</sub> composite with enhanced activity on photocatalytic disinfection of *Aspergillus flavus*. *Chemical Engineering Journal*, 418, p.129417.
- Sun, Y., Meng, X., Dall'Agnesse, Y., Dall'Agnesse, C., Duan, S., Gao, Y., Chen, G. and Wang, X.F., 2019. 2D MXenes as Co-catalysts in Photocatalysis: Synthetic Methods. *Nano-Micro Letter*, 11, pp. 79 - 101.
- Tan, H.L., Abdi, F.F. and Ng, Y.H., 2019. Heterogeneous photocatalysts: an overview of classic and modern approaches for optical, electronic, and charge dynamics evaluation. *Chemical Society Reviews*, 48, pp. 1255 - 1271.
- Truong, N.T., Thi, H.P.N., Ninh, H.D., Phung, X.T., Van Tran, C., Nguyen, T.T., Pham, T.D., Dang, T.D., Chang, S.W., Rene, E.R. and Ngo, H.H., 2020. Facile fabrication of graphene@ Fe-Ti binary oxide nanocomposite from ilmenite ore: An effective photocatalyst for dye degradation under visible light irradiation. *Journal of Water Process Engineering*, 37, p. 101474.
- Tshangana, C., Chabalala, M., Muleja, A., Nxumalo, E. and Mamba, B., 2020. Shape-dependant photocatalytic and antimicrobial activity of ZnO nanostructures when conjugated to graphene quantum dots. *Journal of Environmental Chemical Engineering*, 8, p. 103930.
- Uma, B., Anantharaju, K.S., Renuka, L., Nagabhushana, H., Malini, S., More, S.S., Vidya, Y.S. and Meena, S., 2021. Controlled synthesis of (CuO-Cu<sub>2</sub>O) Cu/ZnO multi oxide nanocomposites by facile combustion route: A potential photocatalytic, antimicrobial and anticancer activity. *Ceramics International*, 47, pp. 14829 - 14844.
- Vattikuti, S.P., Nam, N.D. and Shim, J., 2020. Graphitic carbon nitride/Na<sub>2</sub>Ti<sub>3</sub>O<sub>7</sub>/V<sub>2</sub>O<sub>5</sub> nanocomposite as a visible light active photocatalyst. *Ceramics International*, 46, pp. 18287 - 18296.
- Vattikuti, S.P., Police, A.K.R., Shim, J. and Byon, C., 2018. In situ fabrication of the Bi<sub>2</sub>O<sub>3</sub>-V<sub>2</sub>O<sub>5</sub> hybrid embedded with graphitic carbon nitride nanosheets: Oxygen vacancies mediated enhanced visible-light-driven photocatalytic degradation of organic pollutants and hydrogen evolution. *Applied Surface Science*, 447, pp. 740 - 756.
- Veisi, P., Dorraji, M.S.S., Rasoulifard, M.H., Ghaffari, S. and Choobar, A.K., 2021. Synergistic photocatalytic-adsorption removal effect of NiFe<sub>2</sub>O<sub>4</sub>-Zn-Al mixed metal oxide composite under visible-light irradiation. *Journal of Photochemistry and Photobiology A: Chemistry*, 414, pp.113268 - 113283.
- Venkateshalu, S. and Grace, A.N., 2020. MXenes—A new class of 2D layered materials: Synthesis, properties, applications as supercapacitor electrode and beyond. *Applied Materials Today*, 18, p. 100509.

- Verma, S., Rao, B.T., Singh, R. and Kaul, R., 2021. Photocatalytic degradation kinetics of cationic and anionic dyes using Au–ZnO nanorods: Role of pH for selective and simultaneous degradation of binary dye mixtures. *Ceramics International*, 47, pp. 34751 - 34764.
- Vigneshwaran, S., Sirajudheen, P., Nabeena, C.P., Sajna, V.P. and Meenakshi, S., 2021. Photocatalytic performance of chitosan tethered magnetic Fe<sub>2</sub>O<sub>3</sub>-like (3D/2D) hybrid for the dynamic removal of anionic dyes: Degradation and mechanistic pathways. *International Journal of Biological Macromolecules*, 183, pp. 2088 – 2099.
- Wang, H., Chen, L., Sun, Y., Yu, J., Zhao, Y., Zhan, X. and Shi, H., 2021. Ti<sub>3</sub>C<sub>2</sub> Mxene modified SnNb<sub>2</sub>O<sub>6</sub> nanosheets Schottky photocatalysts with directed internal electric field for tetracycline hydrochloride removal and hydrogen evolution. *Separation and Purification Technology*, 265, pp.118516 -118522.
- Wang, R., Liu, R., Luo, S., Wu, J., Zhang, D., Yue, T., Sun, J., Zhang, C., Zhu, L. and Wang, J., 2021a. Band structure engineering enables to UV-Visible-NIR photocatalytic disinfection: Mechanism, pathways and DFT calculation. *Chemical Engineering Journal*, 421, p. 129596.
- Wang, W., Feng, H., Liu, J., Zhang, M., Liu, S., Feng, C. and Chen, S., 2020. A photo catalyst of cuprous oxide anchored MXene nanosheet for dramatic enhancement of synergistic antibacterial ability. *Chemical Engineering Journal*, 386, pp. 124116 – 124128.
- Wang, Y., Sun, X., Xian, T., Liu, G. and Yang, H., 2021b. Photocatalytic purification of simulated dye wastewater in different pH environments by using BaTiO<sub>3</sub>/Bi<sub>2</sub>WO<sub>6</sub> heterojunction photocatalysts. *Optical Materials*, 113, pp.110853 - 110866.
- Weldegebrerial, G.K. and Sibhatu, A.K., 2021. Photocatalytic activity of biosynthesized  $\alpha$ -Fe<sub>2</sub>O<sub>3</sub> nanoparticles for the degradation of methylene blue and methyl orange dyes. *Optik*, 241, pp. 167226 - 167241.
- WHO, 2017. *Water Quality and Health- Review of Turbidity: Information for regulators and water suppliers*. [pdf] Available at: <[https://www.who.int/water\\_sanitation\\_health/publications/turbidity-information-200217.pdf](https://www.who.int/water_sanitation_health/publications/turbidity-information-200217.pdf)> [Accessed 10 July 2021]
- Wong, K.A., Lam, S.M. and Sin, J.C., 2019. Wet chemically synthesized ZnO structures for photodegradation of pre-treated palm oil mill effluent and antibacterial activity. *Ceramics International*, 45, pp. 1868 - 1880.
- Wu, J., Zhang, Y., Lu, P., Fang, G., Li, X., William, W.Y., Zhang, Z. and Dong, B., 2021. Engineering 2D multi-hetero-interface in the well-designed nanosheet composite photocatalyst with broad electron-transfer channels for highly-efficient solar-to-fuels conversion. *Applied Catalysis B: Environmental*, 286, pp.119944 - 119954.

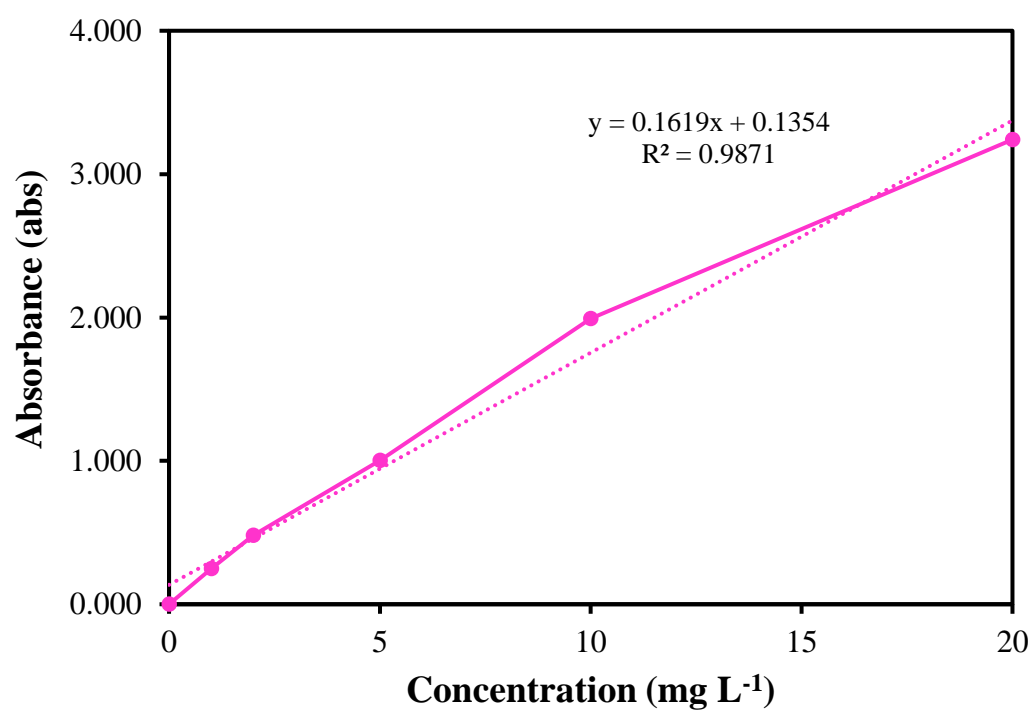
- Xia, Y., He, Z., Su, J., Tang, B., Hu, K., Lu, Y., Sun, S. and Li, X., 2018. Fabrication of magnetically separable NiFe<sub>2</sub>O<sub>4</sub>/BiOI nanocomposites with enhanced photocatalytic performance under visible-light irradiation. *RSC advances*, 8, pp. 4284 - 4294.
- Xie, L., Ren, Z., Zhu, P., Xu, J., Luo, D. and Lin, J., 2021. A novel CeO<sub>2</sub>-TiO<sub>2</sub>/PANI/NiFe<sub>2</sub>O<sub>4</sub> magnetic photocatalyst: Preparation, characterization and photodegradation of tetracycline hydrochloride under visible light. *Journal of Solid State Chemistry*, 300, pp. 122208 - 122219.
- Xu, H., Xiao, R., Huang, J., Jiang, Y., Zhao, C. and Yang, X., 2021. In situ construction of protonated g-C<sub>3</sub>N<sub>4</sub>/Ti<sub>3</sub>C<sub>2</sub> MXene Schottky heterojunctions for efficient photocatalytic hydrogen production. *Chinese Journal of Catalysis*, 42, pp. 107 - 114.
- Yan, D., Fu, X., Shang, Z., Liu, J. and Luo, H.A., 2019. A BiVO<sub>4</sub> film photoanode with re-annealing treatment and 2D thin Ti<sub>3</sub>C<sub>2</sub>T<sub>x</sub> flakes decoration for enhanced photoelectrochemical water oxidation. *Chemical Engineering Journal*, 361, pp. 853 - 861.
- Yang, C., Tan, Q., Li, Q., Zhou, J., Fan, J., Li, B., Sun, J. and Lv, K., 2020. 2D/2D Ti<sub>3</sub>C<sub>2</sub> MXene/g-C<sub>3</sub>N<sub>4</sub> nanosheets heterojunction for high efficient CO<sub>2</sub> reduction photocatalyst: Dual effects of urea. *Applied Catalysis B: Environmental*, 268, p.118738.
- Yang, Y., Zeng, Z., Zeng, G., Huang, D., Xiao, R., Zhang, C., Zhou, C., Xiong, W., Wang, W., Cheng, M. and Xue, W., 2019. Ti<sub>3</sub>C<sub>2</sub> MXene/porous g-C<sub>3</sub>N<sub>4</sub> interfacial Schottky junction for boosting spatial charge separation in photocatalytic H<sub>2</sub>O<sub>2</sub> production. *Applied Catalysis B: Environmental*, 258, pp.117956 - 117967.
- Yang, Z., Zhao, Z., Yang, X. and Ren, Z., 2021. Xanthate modified magnetic activated carbon for efficient removal of cationic dyes and tetracycline hydrochloride from aqueous solutions. *Colloids and Surfaces A: Physicochemical and Engineering Aspects*, 615, p. 126273.
- Yashni, G., AlGheethi, A., Mohamed, R.M.S.R., Arifin, S.N.H., Shanmugan, V.A. and Kassim, A.H.M., 2020. Photocatalytic degradation of basic red 51 dye in artificial bathroom greywater using zinc oxide nanoparticles. *Materials Today: Proceedings*, 31, pp. 136 - 139.
- Yi, X., Yuan, J., Tang, H., Du, Y., Hassan, B., Yin, K., Chen, Y. and Liu, X., 2020. Embedding few-layer Ti<sub>3</sub>C<sub>2</sub>T<sub>x</sub> into alkalized g-C<sub>3</sub>N<sub>4</sub> nanosheets for efficient photocatalytic degradation. *Journal of colloid and interface science*, 571, pp. 297 - 306.
- Yurtsever, A., Basaran, E., Ucar, D. and Sahinkaya, E., 2021. Self-forming dynamic membrane bioreactor for textile industry wastewater treatment. *Science of The Total Environment*, 751, p.141572.

- Zelege, M.A. and Kuo, D.H., 2019. Synthesis and application of  $V_2O_5$ - $CeO_2$  nanocomposite catalyst for enhanced degradation of methylene blue under visible light illumination. *Chemosphere*, 235, pp. 935 - 944.
- Zeng, J., Huang, J., Liu, J., Xie, T., Peng, C., Lu, Y., Lu, P., Zhang, R. and Min, J., 2019. Self-assembly of single layer  $V_2O_5$  nanoribbon/graphene heterostructures as ultrahigh-performance cathode materials for lithium-ion batteries. *Carbon*, 154, pp. 24 - 32.
- Zeng, J., Song, T., Lv, M., Wang, T., Qin, J. and Zeng, H., 2016. Plasmonic photocatalyst  $Au/g-C_3N_4/NiFe_2O_4$  nanocomposites for enhanced visible-light-driven photocatalytic hydrogen evolution. *RSC Advances*, 6, pp. 54964 - 54975.
- Zhan, X., Si, C., Zhou, J. and Sun, Z., 2020. MXene and MXene-based composites: synthesis, properties and environment-related applications. *Nanoscale Horizons*, 5, pp. 235 - 258.
- Zhang, H., Li, M., Cao, J., Tang, Q., Kang, P., Zhu, C. and Ma, M., 2018b. 2D  $\alpha$ - $Fe_2O_3$  doped  $Ti_3C_2$  MXene composite with enhanced visible light photocatalytic activity for degradation of Rhodamine B. *Ceramics International*, 44, pp.19958 - 19962.
- Zhang, H., Wei, W., Hou, F., Guo, W., Zhang, Q., Wang, T. and Wei, A., 2021b. Visible-light-driven photocatalytic disinfection of *Aspergillus fumigatus* under germinative biomorph: Efficiency and mechanism. *Separation and Purification Technology*, 265, p. 118510.
- Zhang, J., Dong, S., Zhang, X., Zhu, S., Zhou, D. and Crittenden, J.C., 2018a. Photocatalytic removal organic matter and bacteria simultaneously from real WWTP effluent with power generation concomitantly: Using an  $ErAlZnO$  photoanode. *Separation and Purification Technology*, 191, pp.101 - 107.
- Zhang, J., Shi, J., Tao, S., Wu, L. and Lu, J., 2021d.  $Cu_2O/Ti_3C_2$ MXene heterojunction photocatalysts for improved  $CO_2$  photocatalytic reduction performance. *Applied Surface Science*, 542, pp.148685 - 148693.
- Zhang, X., Jia, X., Duan, P., Xia, R., Zhang, N., Cheng, B., Wang, Z. and Zhang, Y., 2021a.  $V_2O_5/P-g-C_3N_4$  Z-scheme enhanced heterogeneous photocatalytic removal of methyl orange from water under visible light irradiation. *Colloids and Surfaces A: Physicochemical and Engineering Aspects*, 608, pp. 125580 - 125591.
- Zhang, X., Jia, X., Duan, P., Xia, R., Zhang, N., Cheng, B., Wang, Z. and Zhang, Y., 2021a.  $V_2O_5/Pg-C_3N_4$  Z-scheme enhanced heterogeneous photocatalytic removal of methyl orange from water under visible light irradiation. *Colloids and Surfaces A: Physicochemical and Engineering Aspects*, 608, pp. 125580 - 125591.
- Zhang, Y., Shen, G., Sheng, C., Zhang, F. and Fan, W., 2021c. The effect of piezo-photocatalysis on enhancing the charge carrier separation in  $BaTiO_3/KNbO_3$  heterostructure photocatalyst. *Applied Surface Science*, 562, pp. 150164 - 150176.

- Zhao, G., Ding, J., Zhou, F., Chen, X., Wei, L., Gao, Q., Wang, K. and Zhao, Q., 2021. Construction of a visible-light-driven magnetic dual Z-scheme BiVO<sub>4</sub>/g-C<sub>3</sub>N<sub>4</sub>/NiFe<sub>2</sub>O<sub>4</sub> photocatalyst for effective removal of ofloxacin: Mechanisms and degradation pathway. *Chemical Engineering Journal*, 405, pp. 126704 - 126719.
- Zhao, H., Lv, J., Sang, J., Zhu, L., Zheng, P., Andrew, G. and Tan, L., 2018. A facile method to construct MXene/CuO nanocomposite with enhanced catalytic activity of CuO on thermal decomposition of Ammonium Perchlorate. *Materials*, 11, p. 2457.
- Zhong, Q., Li, Y. and Zhang, G., 2020. Two-dimensional MXene-based and MXene-derived photocatalysts: recent developments and perspectives. *Chemical Engineering Journal*, 409, pp.128099 - 128117.
- Zhuang, Y., Liu, Y. and Meng, X., 2019. Fabrication of TiO<sub>2</sub> nanofibers/MXene Ti<sub>3</sub>C<sub>2</sub> nanocomposites for photocatalytic H<sub>2</sub> evolution by electrostatic self-assembly. *Applied Surface Science*, 496, pp.143647 - 143654.

## APPENDICES

Appendix A: Calibration Curve of RhB Dye at Wavelength of 553 nm.



**BOOK CHAPTER**

1. Lam SM\*, Yong ZJ, Choong MK, Sin JC, Chin YH, Tan JH, *MXene-Based Photocatalyst: Fabrication and Applications* with book chapter “Construction of MXene-Based Photocatalysts”, Accepted in Taylor & Francis Group Publisher 2021.

## AWARDS

1. **Gold Medallist**, awarded by 9<sup>th</sup> National Innovation and Invention Competition through Exhibition 2021 (iCompEx'21), September 2021, Jitra, Kedah.

Title of Invention : Innovative constructed wetland-microbial fuel cell for sustainable wastewater treatment and electricity production

Contributors : ChM. Ts. Dr. Lam Sze Mun, ChM. Ts. Dr. Sin Jin Chung, Leow Guo Yao, Ng Yee Jie, Choong Man Kit

2. **Gold Medallist**, awarded by Perlis International Engineering Invention and Innovation Exhibition 2020 (Pi-ENVEX 2020), May 2020, Arau, Perlis.

Title of Invention : Photocatalytic Fuel Cell for Sustainable Wastewater Treatment and Bacteria Disinfection Synchronized with Electricity Production

Contributors : ChM. Ts. Dr. Lam Sze Mun, ChM. Ts. Dr. Sin Jin Chung, Choong Man Kit, Chai Yen Yi, Ng Hao Yu